University of Miyazaki
Ph.D. Thesis

Development of Solar Concentrators and Solar Cells to Generate Electrical Energy

（電気エネルギー生成のための集光系および太陽電池の開発）

September, 2017

Department of Materials and Informatics
Interdisciplinary Graduate School of Agriculture and Engineering
University of Miyazaki
Nawwar Ahmad

Contents

Abstract

The first chapter: Introduction.

In this chapter, we discuss solar radiation and different technologies used to utilize solar energy like solar cells, concentrator photovoltaic (CPV) systems, and thermal solar energy systems. This chapter also explains about the special type of solar cells called multijunction solar cells, which are used in CPV systems and introduce the details of current calculations in these cells. This chapter also gives a brief history of the CPV technologies, spectral splitting techniques used to improve concentrator performance and the effect of temperature on solar cell performance.

The second chapter: Designing of long wavelength cut thin-film filter for temperature reduction of concentrator photovoltaic.

This chapter explains one of the primary methods implemented in this study to optimize CPV performance by decreasing the operating temperature of the multijunction solar cell used in CPV systems. This is done by cutting the solar spectrum that is not utilized in the solar cell and only allowing the spectrum in the range of the effective EQE to reach the solar cell. The study was conducted for two concentrator systems. The first system used InGaP/InGaAs/Ge triple junction solar cell with high spectral response in the range of 400−1700 nm. The second system used InGaP/GaAs/InGaAs triple junction solar cell with high spectral response in the range of 400−1100 nm. The optical system consists of Fresnel lens and homogenizer with a concentration ratio of 1322 times. We

cut the undesired solar spectrum range by using a thin-film filter on the surface of the homogenizer, which can achieve the desired spectrum cutting. Using needle optimizing and TFcalc (commercial thin-film design software) we developed two filters. The first filter was used for the concentrator module with InGaP/InGaAs/Ge triple junction solar cell. This filter only allowed the spectrum in the range of 400−1700 nm to be transmitted onto the solar cell while reflecting the rest of the long wavelength spectrum. The second thin-film filter used for the CPV module with InGaP/GaAs/InGaAs triple junction solar cell. This filter transmitted the spectrum in the range of 400−1100 nm and reflected the rest of the spectrum. Thermal simulation for the two cases compared to the system without thin-film showed that the highest cell temperature was for the system without thin-film filter (118.7°C), while the temperature dropped to 114.5°C when using 1700 nm cutoff wavelength thin-film with a total drop of about 4°C. The best thermal performance was achieved by the CPV system using 1100 nm wavelength cutoff filter where the temperature decreased by 18.2°C to reach 100.5°C.

The third chapter: Temperature reduction of solar cells in a concentrator photovoltaic system using a long wavelength cut filter.

This chapter discusses more detailed study for the system with InGaP/GaAs/InGaAs triple junction solar cell introduced in chapter 2. We used the same optical structure from chapter 2, yet because the solar cell showed better performance under spectrum in the range of 400−1300 nm, a new design for the thin-film was carried out and a new structure consists of 97 layers was designed. Ray-tracing was performed in the wavelength range of 300−2500 nm to show the effect of the thin-film filter on the overall performance of the CPV system. We improved COMSOL Multiphysics thermal model by adding three heat sources compared to one source which uses the total direct radiation in the first stage of this research. The first source, which represented the ultraviolet spectrum, and the second source, which represented the efficient spectrum, were added to the surface of the solar cell, the third source for the IR spectrum was added on the rear surface of the solar cell.

An electrical characteristics analysis for the CPV multijunction solar cell was conducted using single unit equivalent circuit model. We also introduced an average Arrhenius–Weibull model to calculate the unreliability and estimate the lifetime of the multijunction solar cell under different temperatures and irradiation fluctuation throughout the year in Miyazaki City. The simulation results showed that the cell temperature dropped from a maximum of 121°C (without the thin-film filter) to 95.7°C (with the thin-film filter), representing a total decrease of 25.3°C. Owing to the effect of the thin-film filter, which removes long-wavelength spectrum, the cell temperature was markedly reduced. Electrical simulation results showed that the open-circuit voltage (V_{oc}) increased due to the decrease in the solar cell temperature, while the current dropped a small amount due to the presence of the thin-film filter. The unreliability calculation to estimate the lifetime of the solar cell showed an increase in lifetime of 1.9×10^5 h. This means that for our concentrator photovoltaic system, the lifetime was increased by more than 65 years for a failure population of 5% through the use of a thin-film filter.

The fourth chapter: **111 suns concentrator photovoltaic module with wide acceptance angle that can efficiently operate using 30-min intermittent tracking system.**

In this chapter we proposed a new concentrator photovoltaic (CPV) system design with a wide acceptance angle lens, which tracks the sun based on a new 30-min intermittent tracking method that does not require a special high-precision CPV tracking system. This allowed the reduction of costs because a large percentage of the expense of a typical CPV system comes from the expensive accurate tracking system. The present system had a concentration ratio of 111 and an acceptance angle of 4.5°. We conducted an experiment to evaluate the thermal and electrical performances of the system in the outdoor test site in Miyazaki, Japan.

Optical, thermal, and electrical simulations for the module for the two cases (with zero tracking error angle and with the highest tracking error angle) was conducted and results were compared with the experimental results to evaluate the validity of the used wide acceptance angle CPV module and the efficiency of the design. The thermal simulation showed good agreement with the experimental results. The electrical outputs data of the system showed a significant difference from the simulated results. This difference was expected to be caused by the excessive silicone sealing around and between the solar cell and the homogenizer. A sensitivity analysis was conducted to evaluate the effect of the excessive sealing on the irradiance distribution and electrical characteristics of the module.

Results showed that silicone sealing should be done with more precision with the lowest possible thickness of silicone between the multijunction solar cell surface and the homogenizer exit surface, in order to obtain better electrical and overall performance for the system.

The fifth chapter: Summary.

This chapter summarizes the results of this thesis and gives a conclusion for the best ways to improve the working conditions of CPV systems and multijunctions solar cells in concentrator systems based on our study. This chapter also gives some suggestion for future work .

In this thesis, we were able to solve two main problems in CPV systems using different approaches from conventional ones. The first problem we were able to overcome is the increase in solar cell temperature in high concentrator photovoltaic systems. This was done by using thin-film filter instead of conventional heat sink design. The use of the thin-film technique in CPV model achieved the same system performance despite the large cut in spectrum and a significant increase in the lifetime of the CPV system which is considered a big appeal point from economical point of view.

The second problem we were able to overcome was the need for high precision tracking system that moves every minute and consume large amount of energy. This type of tracker usually add extra cost and complexity to the CPV design. We overcome this problem by using 30-min intermittent tracking system with wide-acceptance-angle CPV system. Results proved that there was no significant difference in the performance of the

CPV system with zero tracking error and under the highest tracking error angle which led to decreasing the cost and complexity of the CPV system. The use of such a system also led to decrease in the consumed power because the tracker moves every 30 minute while it goes into sleep the rest of the time. We consider the pervious improvement using this tracking system a powerful appeal points that would open new doors for further improvements in the CPV systems design by reducing the complexity and cost.

Acknowledgment

This work was done at Nishioka laboratory, department of materials and informatics, Interdisciplinary Graduate School of Agriculture and Engineering, Miyazaki University, under the supervision of Professor Kensuke Nishioka. Part of this work was supported by the New Energy and Industrial Technology Development Organization (NEDO) under the Ministry of Economy, Trade and Industry of Japan (METI).

The author would like to express his great gratitude to Professor Kensuke Nishioka for all the support and guiding that he provided throughout the author doctoral degree, and for all the advice and the detailed remarks that led to great improvement in the quality of the author’s work. The author would also like to express his deep emotion of thanks to Professor Nishioka for trusting the author and believing in him in the difficult times which gave the author the chance to finish this doctoral degree.

The author would also like to express his deep gratitude to Dr. Yasuyuki Ota for all the help and the support during the time of his doctoral degree. For all the in-depth advice and wonderful ideas that enriched the content of this work and led to great improvement in the scientific level of the author and left him with a more open-mindedness toward the future.

The author would like to express special thanks to Dr. Kenji Araki from Toyota Institute of Technology for the great chance to work with him and get enlightened by his great expertise and deep knowledge in the field of concentrator photovoltaics and for the many suggestions and discussions regarding the author work.

The author would also like to express his deep thanks to Prof. Noboru Yamada from Nagaoka University of Technology for all the support, the encouraging and deep understanding for the author at the beginning of his life in japan as a member of Yamada laboratory.

The author would like to express his love and thanks for his mother and his sister for supporting him all the way through his journey, and for standing by him and believing in his abilities throughout his doctoral degree and his life in Japan. The author would also like to dedicate his doctoral work to his deceased father for believing in him and having great faith that his son would make something beautiful out of his life even on his deathbed, may his soul rest in peace.

List of figures

List of tables

Chapter 1

Introduction

1.1. Solar energy

Recently, there has been a significant increase in the need and desire for energy independence. Much work is being done in a variety of fields to develop alternative energy sources to supplement, and perhaps replace the current energy sources all around the world. One of these fields is solar energy. There is a significant amount of research and development being done to try to improve the efficiency and lower the cost of solar energy systems.

Solar radiation that strikes the earth's surface contains a large amount of energy. On a sunny day, there are approximately 1,000 watts of solar power available to every square meter of a surface pointed normal to the sun. The goal of solar energy systems is to convert the sun's energy into another form of usable energy.

Solar radiation in space without the influence of the Earth's atmosphere is referred to as the AM0 spectrum. When light passes through the Earth's atmosphere (Fig.1-1) [1], the irradiance is reduced as a result of:

1. Reflection off the atmosphere.
2. Absorption by molecules in the atmosphere (H_2O, CO_2).
3. Rayleigh scattering (molecular scattering).
4. Mie scattering (scattering of dust particles and pollutants in the air).

There are two main commercial classes of solar energy systems: solar thermal and photovoltaic.

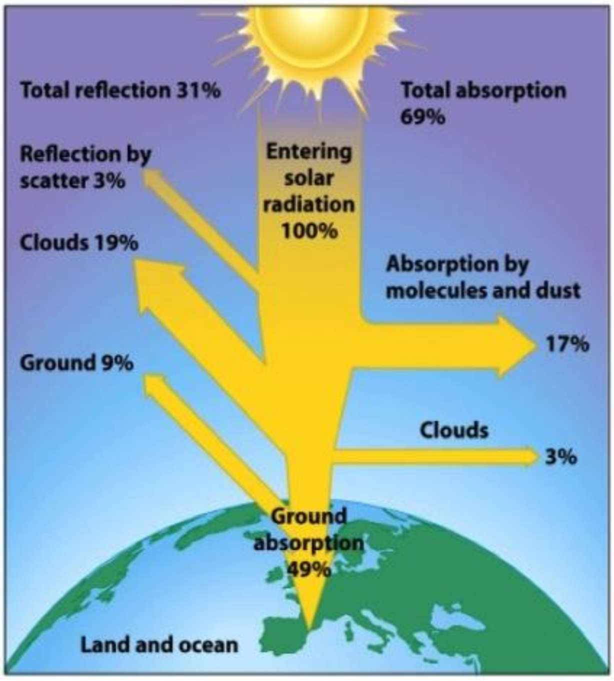

Fig. 1- 1: Sunlight as it passes through the atmosphere [1].

1.2. Thermal solar energy

In solar thermal systems, the sun's energy is used for heat generation. Solar thermal systems usually use an optical system, typically a mirror, to collect the sunlight and focus it to generate a large amount of heat in a small area. The sunlight heats up a heat transfer fluid that is then used to generate power. These systems are referred to as concentrated solar power (CSP) systems.

One common type of CSP system uses a parabolic trough mirror to create a line focus as shown in Fig. 1-2. A tube filled with the heat transfer fluid is placed at the line focus, and the focused sunlight is used to heat the fluid. Another type of system similar to the parabolic trough is a linear Fresnel system that uses smaller mirror segments instead of a full parabolic trough to concentrate the light to a line focus. Another class of CSP systems uses a large array of heliostats that all reflect the incident sunlight and direct it to a focal region at the top of a large tower. One last kind of CSP system places an engine or generator, often a Stirling engine, at the focal point of a dish concentrator [2].

Fig. 1- 2: Photograph of the Eurotrough collector loop (Skal-ET) implemented by solar millennium California [2].

1.3. Solar cells (Photovoltaic:PV)

In photovoltaic (PV) solar energy systems, sunlight is converted into electricity via the photovoltaic effect. PV devices are typically made from semiconductor materials. When photons with energy greater than the bandgap of the semiconductor material strike the device, an electron-hole pair can be created. The wavelength, λ_g corresponding to the bandgap energy, E_g, is given by

$$\lambda_g = \frac{hc}{E_g}, \qquad (1.1)$$

where h is Planck's constant and c is the speed of light. As electron-hole pairs are created, a current is generated. When an external voltage is applied to the solar cell, it generates power [3]. There are different materials that can be used for PV devices, with silicon being the most common material used for PV devices.

The conversion efficiency, η, of solar cells is calculated as the ratio between the generated maximum power P_m, generated by a solar cell and the incident power P_{in}. The η is determined from the *I–V* measurement using Eq. (1.2).

$$\eta = \frac{P_m}{P_{in}} = \frac{J_{sc}.V_{oc}.FF}{P_{in}}, \quad (1.2)$$

Where J_{sc} is the solar cell short current; V_{oc} is the open circuit voltage; *FF* is the solar cell fill factor. The irradiance of AM1.5 spectrum can be calculated from the spectral power density, $P(\lambda)$ shown in Fig. 1-3 using the following equation:

$$P_{in} = \int_0^\infty P(\lambda)\, d\lambda = \int_0^\infty \phi(\lambda) \frac{hc}{\lambda} d\lambda, \quad (1.3)$$

where $\phi(\lambda)$ is the photon flux density.

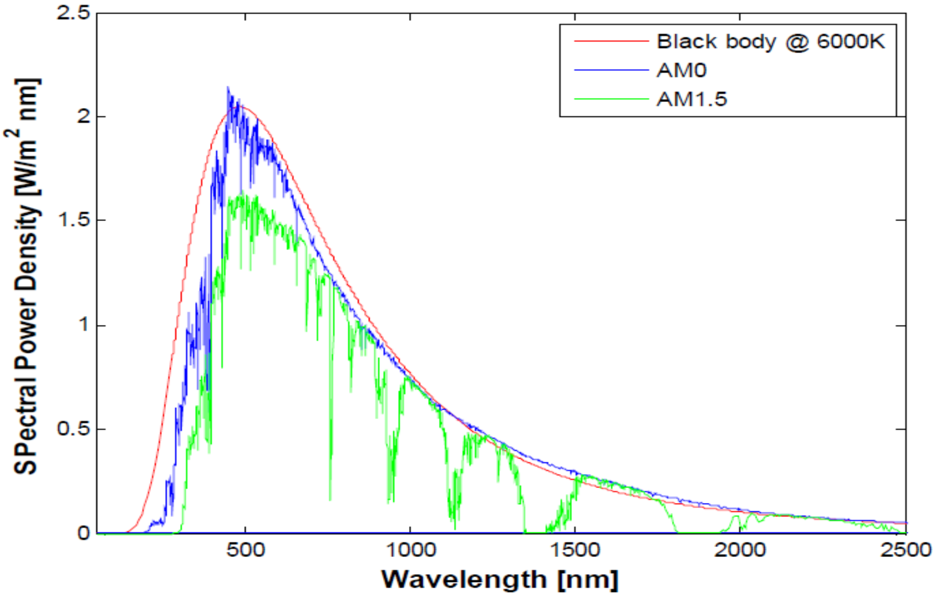

Fig. 1- 3: Spectral power density of black-body radiation at 6000 K, AM0 and AM1.5.

We can determine the fraction of energy of the incident radiation spectrum that is absorbed by a single junction solar cell. When we denote λ_G as the wavelength of photons that corresponds to the band gap energy of the absorber of the solar cell, only the photons with the energy higher than the bandgap are absorbed, it means photons with $\lambda \leq \lambda_G$.

The fraction of the incident power, p_{abs} that is absorbed by a solar cell and used for energy conversion is expressed as:

$$P_{\text{abs}} = \frac{\int_0^{\lambda_G} \phi(\lambda) \frac{hc}{\lambda} d\lambda}{\int_0^{\infty} \phi(\lambda) \frac{hc}{\lambda} d\lambda}. \tag{1.4}$$

A part of the absorbed energy, the excess energy of photons, is lost due to the thermalization of photo-generated electrons and holes in the absorber material. The fraction of the absorbed energy that the solar can deliver as useful energy, p_{use}, is described by Eq. (1.5):

$$P_{\text{use}} = \frac{E_G \int_0^{\lambda_G} \phi(\lambda) d\lambda}{\int_0^{\lambda_G} \phi(\lambda) \frac{hc}{\lambda} d\lambda}. \tag{1.5}$$

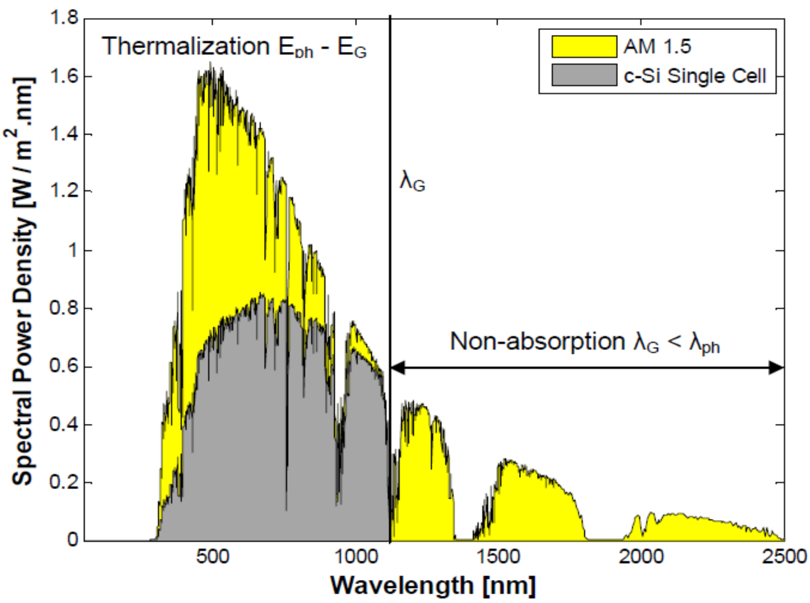

Fig. 1- 4: The fraction of the AM1.5 spectrum that can be converted into a usable energy by a crystalline silicon solar cell.

Figure 1-4 illustrates the fraction of the AM1.5 spectrum that can be converted into a usable energy by a crystalline silicon solar cell.

We can determine the conversion ultimate efficiency limited by the spectral mismatch using the following equation:

$$\eta = P_{\text{abs}}.P_{\text{use}} = \frac{\int_0^{\lambda_G} \phi(\lambda)\frac{hc}{\lambda}d\lambda}{\int_0^{\infty} \phi(\lambda)\frac{hc}{\lambda}d\lambda}\frac{E_G \int_0^{\lambda_G} \phi(\lambda)d\lambda}{\int_0^{\lambda_G} \phi(\lambda)\frac{hc}{\lambda}d\lambda}. \qquad (1.6)$$

1.4. Multijunction solar cells

Multijunction solar cells are a new technology that offers extremely high efficiencies compared to traditional solar cells made of a single layer of semiconductor material.

Depending on the particular technology, multijunction solar cells are capable of generating approximately twice as much power under the same conditions as traditional solar cells made of silicon. Unfortunately, multijunction solar cells are very expensive.

With a traditional single layer solar cell, much of the energy of incident light is not converted into electricity. If an incident photon has less energy than the bandgap of the semiconductor material, the photon cannot be absorbed since there is not enough energy to excite an electron from the conduction band to the valence band. Therefore, none of the light with less energy than the bandgap is used in the solar cell. If an incident photon has more energy than the bandgap, the excess energy will be converted into heat since the electron can only absorb the exact amount of energy required to move to the valence band.

Multijunction solar cells can make better use of the solar spectrum by having multiple semiconductor layers with different bandgaps. Each layer is made of a different material, which usually is a III-V semiconductor, and absorbs a different portion of the spectrum. The top layer has the largest bandgap so that only the most energetic photons are absorbed in this layer. Less energetic photons must pass through the top layer since they are not energetic enough to generate electron hole pairs (EHPs) in the material. Each layer going from the top to the bottom has a smaller bandgap than the previous. Therefore, each layer absorbs the photons that have energies greater than the bandgap of that layer and less than the bandgap of the higher layer. The most common form of multijunction solar cell consists of three layers, which is called a triple junction solar cell. one of the most powerful multijunction solar cells in commercial production today are triple junction cells made of InGaP, InGaAs, and Ge as shown in Fig. 1-5.

The triple junction solar cells used in this study are of two types: InGaP/InGaAs/Ge triple junction solar cell and InGaP/GaAs/InGaAs triple junction solar cell.

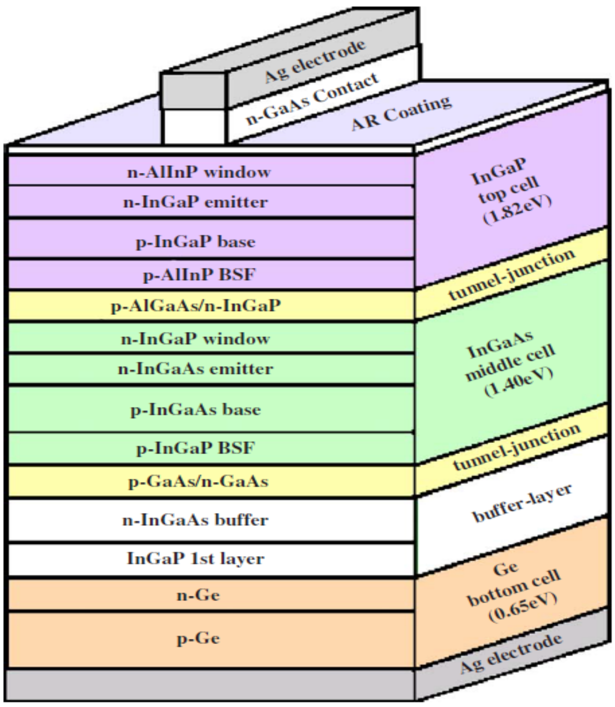

Fig. 1- 5: Schematic of an InGaP/InGaAs/Ge triple junction solar cell.

1.5. Flat panel Photovoltaic systems

There are two general types of PV systems, namely flat panel and concentrating systems. The majority of PV systems in production today are flat panel systems.

Except for a cover plate, there is no optical system prior to the PV device. The sunlight goes directly to the PV device without being focused. Because there is no concentration, light from any angle can be collected by flat panel systems. Therefore, flat panel systems can collect and convert diffuse light from the sky (or light reflected from the ground, snow, etc.) as well as direct sunlight as shown in Fig.1-6.

Fig. 1- 6: Flat panel photovoltaic System.

Since flat panel PV systems can collect light over an entire hemisphere, it is not necessary to use a tracking system to always point the system normal to the sun. The contribution from the diffuse light is approximately the same throughout the day, assuming no major changes in the weather conditions or cloud cover. However, as the sun moves across the sky, the projected area of the flat panel depends on the relative position of the sun to the panel. The projected area A_{proj} is defined as

$$A_{\mathrm{proj}} = A. \cos\theta, \quad (1.7)$$

where A is the area of the panel and θ is the incidence angle of the sunlight on the panel relative to normal. This leads to a significant reduction in the amount of sunlight that the panel can collect and, therefore, a lower power output as the sun moves away from the normal. If a dual-axis tracking system is used, then the panel can be kept pointed directly at the sun to avoid the decrease of power output due to the projected area.

1.6. Concentrator Photovoltaic systems (CPV)

Concentrator photovoltaic (CPV) systems use optics to concentrate the incident sunlight onto small photovoltaic solar cells. The motivation behind CPV solar systems, in general, is that solar cells, particularly high-efficiency solar cells, are very expensive, and by concentrating the incident solar radiation onto the solar cell a smaller amount of photovoltaic device area is needed compared to the overall module input area. The photovoltaic device cost per total module area can be reduced greatly using concentration. This is particularly true for CPV systems that use high-efficiency solar cells that are much more expensive than traditional silicon solar cells [4]. The Amonix 7700 system, for example, consists of seven concentrating module units, so called Mega Modules, mounted on a two-axis tracker as shown in Fig. 1-7. Sunlight is concentrated onto 7560 focal spots at a ratio of 500:1. This system uses multijunction InGaP/InGaAs/Ge cells grown on a germanium substrate rated at 37% efficiency under the test conditions of 50 W/cm^2, 25°C, and AM 1.5D. With an aperture area of 267 m^2, the capacity of this unit corresponds to 53 KWp AC power under the test conditions of the photovoltaics for utility scale applications (PVUSA), i.e., 850 W/m^2 direct normal incidence (DNI), 20ºC ambient temperature, and 1 m/sec wind velocity.

Fig. 1- 7: The Amonix 7700 60 kW AC system uses high-efficiency multijunction solar cells.

Along with decreasing the area and cost of the PV device, concentration also leads to an increase in the efficiency of the device. However, as the concentration increases, resistance losses begin to cause the efficiency to decrease. The optimal concentration for a given solar cell is dependent on the properties of that cell [5].

While concentration helps reduce the cost of the PV cells in a CPV system, it also adds complexity and cost in other ways. With concentration, the possible acceptance angle or the largest incidence angle at the front aperture of the system for which light can be collected by the system is decreased based on the étendue of the system. The geometric concentration, C_g, of a system is defined as:

$$C_g = \frac{A}{A'} \ , \tag{1.8}$$

where A and A' are the area of the input to the system and of the PV device, respectively. Through the principle of étendue, there is a fundamental limit on the geometric concentration that is attainable, based on the acceptance angle of the system [6]. For a rotationally symmetric system (including a circular PV device) with an acceptance angle of θ and where the largest incidence angle on the PV device is θ', the limit on the geometric concentration is:

$$C_g = \left(\frac{n' \sin\theta'}{n \sin\theta}\right)^2, \qquad (1.9)$$

where n is the index of refraction at the entrance aperture of the system and n' is the index of the medium immediately before the PV device. From equation (1.9) it follows that the maximum possible acceptance angle is

$$\theta = \sin^{-1}\left(\frac{n' \sin\theta'}{n \sqrt{C_g}}\right). \qquad (1.10)$$

For systems that have a rectangular front aperture and a rectangular PV device, it is helpful to look at the consequence of étendue in two dimensions. In two dimensions the equations (1.9) and (1.10) become, respectively,

$$C_g = \left(\frac{n' \sin\theta'}{n \sin\theta}\right), \qquad (1.11)$$

and

$$\theta = \sin^{-1}\left(\frac{n' \sin\theta'}{n\, C_g}\right), \qquad (1.12)$$

therefore, the limits can be calculated independently for each dimension of the system. CPV systems are divided into three main types based on the geometrical concentration value of the system. These three types are:

I: Low concentration, C_g = 2 ~ 100.

II: Middle concentration, C_g = 100 ~ 300.

III: High concentration, C_g = 300 to more than 1000.

Static CPV system (i.e. no tracking) could be used to collect direct sunlight for a portion of the day, as well as a smaller amount of diffuse light. For higher concentrations and if the light collection is desired throughout the day, though, a tracker is needed to always have the system pointed at the sun. The addition of a tracking system adds significant cost to the overall system. The added complexity of combining the optics with the PV devices also adds to the cost.

1.7. Photocurrent in CPV

The generated concentration short-circuit current (I_{sc}) is proportional to the luminous flux, meanwhile the open circuit voltage (V_{oc}) increases logarithmically with photogenerated current. Hence, concentrated sunlight increases solar cell voltages, which implies higher efficiencies as long as the increased series resistance (R_s) does not overcompensate them by inducing reduced fill factors (*FF*). Fill factor is a parameter which, in conjunction with V_{oc} and I_{sc}, indicates the maximum power obtained from the solar cell. There is a decrease in voltage due to the temperature increase in concentration but, in comparison with the influence of R_s, it is less significant [5]. However, in CPV it is important to provide cooling of the solar cells by radiation and/or convection using a heat sink in most cases. Additionally, the set of standard test conditions for CPV systems includes a cell temperature of 25°C, apart from the standard ASTM G-173 AM 1.5D solar spectrum and incident optical power of 900 W/m^2 at the entry aperture of the concentrator.

Gridlines are conductive, usually metallic, strips that provide an electrical contact on the front face of the triple junction (3J) cell. Solar cell grid is designed for uniform irradiance conditions. This is not because uniform is the optimum irradiance distribution in terms of efficiency, but because this design is simple and it seems to adapt better to arbitrary irradiance distributions.

A narrow base width of metallic gridlines leads to increased series resistance (R_s) due to the low metal cross-section meanwhile higher base widths increase obscuration. It is important to find optimum gridlines parameters combination for particular cell size and level of incident light in order to maintain high electrical conductance and minimize the metal obscuration at the same time.

High local differences in flux over the solar cell surface can cause efficiency losses due to increased series resistance (R_s), although this has less impact in multijunction cells than in silicon cells. In case of multijunction cells, we have to assure that their tunnel diodes are operating in the tunneling region [7-9]. It is recommendable that irradiance non-uniformities are kept low due to cell efficiency losses, and also because of the reliability of the cell or that the encapsulant may be compromised [10-11].

If the irradiance distributions corresponding to the spectral bands of different junctions are matched, even though these distributions are not uniform, the efficiency drop may not be severe [9, 12]. Multi-junction cell efficiency is affected by the chromatic differences in the irradiance distribution (which has been referred to as chromatic aberration [13-16]) due to local current mismatch between top and middle cells. The sensitivity of modern III-V cells to the spectral dependence of the irradiance distribution is expected to increase in the future, when four or even more junctions are used.

In order to describe spectral behavior of solar cells, the External Quantum Efficiency (EQE) is defined as the number of electrons generated and collected for each photon incident on the cell, i.e.: $EQE = n_E / n_P$ where n_E is the number of electrons generated and collected and n_P the number of incident photons, both per unit time.

The electrons generated but then recombined do not count. This would be the Internal Quantum Efficiency (IQE), which is higher. The Irradiance density is defined as:

$$I_D = dP/(A \cdot d\lambda), \quad (1.13)$$

where dP is the light power (energy per unit time), A is surface area and $d\lambda$ unit wavelength. The EQE and irradiance density are shown in Fig. 1-8.

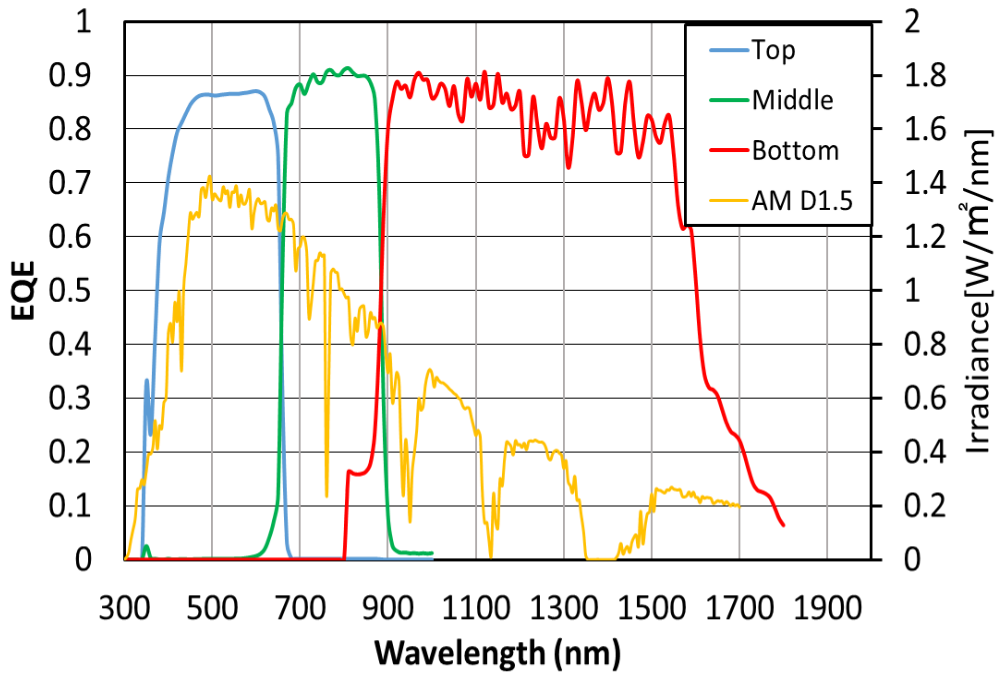

Fig. 1- 8: External Quantum Efficiencies (EQEs) of 3J cell sub-cells (blue-top, green-middle, red-bottom) and Irradiance density of the *ASTM G173 AM1.5D* standard terrestrial solar spectrum.

Electrical current is defined as the number of electrons per second (generated and collected as current):

$$I = n_E \cdot q, \quad (1.14)$$

where n_E is number of electrons and q the charge of the electron (q=1.602·10^{-19}C). According to the definition of EQE, the number of electrons produced by incident light in the range λ to $\lambda+\Delta\lambda$ is given by

$$n_E = \mathrm{EQE}(\lambda) \cdot n_P, \qquad (1.15)$$

obtained by the EQE multiplied by the number of incident photons for that wavelength . The energy of each photon at a wavelength λ is given by:

$$E = h\nu = hc/\lambda, \qquad (1.16)$$

where h is Planck's constant (h = 6.626·10^{-34}J·s), c is the speed of light (c = 2.998·10^{8}m·s^{-1}).

The power associated with these photons is $P = n_p \cdot E$ where n_P is the number of photons per unit time. Introducing this into the expression for I_D we get:

$$I_D = \frac{n_p \cdot E}{A \cdot d\lambda}. \qquad (1.17)$$

The number of photons per unit time in the range λ to $\lambda+\Delta\lambda$ can then be obtained by:

$$n_p = \frac{I_D \cdot A}{E} d\lambda. \qquad (1.18)$$

Therefore the corresponding photocurrent is given by:

$$I_{\lambda,\lambda+\Delta\lambda} = n_e \cdot q = EQE(\lambda) \cdot n_p \cdot q = A\frac{q \cdot \lambda}{h \cdot c} I_D(\lambda) \cdot EQE(\lambda) \cdot d\lambda. \qquad (1.19)$$

The short-circuit currents at 1 sun concentration for a single solar cell is calculated by integrating the previous Equation in the wavelength range corresponding to the spectral response of the cell. For each sub-cell of the 3J cell, under the ASTM G173 AM1.5D spectrum corresponding photocurrents will be calculated as:

$$I_{sc,Top}^{1sun} = \frac{q \cdot A_{cell}}{h \cdot c} \int_{350}^{1800} \lambda \cdot I_{D_{AM1.5D}}(\lambda) \cdot EQE_{TOP}(\lambda) d\lambda.$$

$$I_{sc,Middle}^{1sun} = \frac{q \cdot A_{cell}}{h \cdot c} \int_{350}^{1800} \lambda \cdot I_{D_{AM1.5D}}(\lambda) \cdot EQE_{Middle}(\lambda) d\lambda. \quad (1.20)$$

$$I_{sc,Bottom}^{1sun} = \frac{q \cdot A_{cell}}{h \cdot c} \int_{350}^{1800} \lambda \cdot I_{D_{AM1.5D}}(\lambda) \cdot EQE_{Bottom}(\lambda) d\lambda.$$

As these junctions are series connected, the smallest photocurrent of the three junctions will limit the photocurrent of the solar cell. In today's high-efficiency commercial cells photocurrents of the top and middle junctions are designed to be fairly well balanced (within about ±5% at the usual solar spectra, such as the standard ASTM G173 AM 1.5D). This is accomplished by the selection of the band gaps of the semiconductor materials, by the metal gridlines design and fabrication and design of the antireflection (AR) coating on the top of the solar cell. In case of the bottom Ge junction the bandgap energy is much smaller than required, which leads to an excessive photocurrent (by 40% to 50%) over those of the top and middle junctions. Hence, we may say that in present commercial 3J high-efficiency cells it is approximately true that:

$$I_{sc,3J} = I_{sc,Top} \approx I_{sc,Middle} \approx \frac{2}{3} I_{sc,Bottom}. \quad (1.21)$$

The short-circuit currents at geometrical concentration C_g are calculated as:

$$I_{sc,Top}^{conc} = \frac{q \cdot A_{cell} \cdot C_g}{h \cdot c} \int_{350}^{1800} \lambda \cdot I_{D_{AM1.5D}}(\lambda) \cdot EQE_{TOP}(\lambda) \cdot T(\lambda) d\lambda,$$

$$I_{sc,Middle}^{conc} = \frac{q \cdot A_{cell} \cdot C_g}{h \cdot c} \int_{350}^{1800} \lambda \cdot I_{D_{AM1.5D}}(\lambda) \cdot EQE_{Middle}(\lambda) \cdot T(\lambda) d\lambda, \quad (1.22)$$

$$I_{sc,Bottom}^{conc} = \frac{q \cdot A_{cell} \cdot C_g}{h \cdot c} \int_{350}^{1800} \lambda \cdot I_{D_{AM1.5D}}(\lambda) \cdot EQE_{Bottom}(\lambda) \cdot T(\lambda) d\lambda,$$

where A_{cell} is the solar cell area, h is the Planck's constant, c is the speed of light, C_g is geometrical concentration, $I_{D_{AM1.5D}}(\lambda)$ is the solar irradiance density as a function of wavelength (containing an integrated power density of 900 W/m^2 over the interval 350-

1800nm), $EQE_{TOP}(\lambda)$, $EQE_{Middle}(\lambda)$, $EQE_{Bottom}(\lambda)$ are the external quantum efficiency of top, middle, bottom sub-cells, respectively and $T(\lambda)$ is the spectral transmission of the concentrator.

1.8. Historical summary of CPV

While CPV technology has been under development for many years, commercialization has been elusive as technical and reliability difficulties dominated the development of this seemingly simple idea [17]. In addition, the rapidly maturing silicon panel market with its head start of many decades raised significant barriers to market entry. Swanson illuminates the dilemma facing the CPV industry in greater detail than is possible here and explains why the expected increase in commercial investment did not occur during that period [18]. Sala and Luque characterize the period up to the late 1990s as one dominated by academic leadership [19], with some product development progress being made by only a small number of companies, Amonix and Solar Systems Australia being examples, but advances in the efficiency of practical high-performance multijunction cells have reignited interest in HCPV. These cells, first developed for the space applications market and using materials other than silicon, promise conversion efficiencies of well over 40% but at a cost extremely prohibitive for use in standard panels, at one sun. The only possible application for these cells in a terrestrial environment is in high concentrator photovoltaic (HCPV) system. Significantly, this rebirth occurred at a time of great interest in energy prices and sustainable practices, much of it coming from the worldwide venture capital community, seeking a post-internet boom market. In addition, by the time the investment industry started to analyze CPV seriously, these cells had passed the stringent reliability standards of the space industry and had amassed millions of successful cell-hours of operation. This confluence of performance promise, interest in renewable energy sources, and positive reliability data emboldened the investment industry, and an explosion in new HCPV companies occurred in the first few years of the century. This was soon followed by investments in the cell segment itself, as meaningful progress had been made on new cell morphologies and related technologies [20], building on the pioneering work at NREL. The LCPV segment also received significant interest.

Improvements in silicon cells, while not as spectacular as those in multi-junction cells, were important to this segment of the industry. The combination of efficiencies in the 18% range and low fabrication costs allowed for designs to made economic sense. Though a smaller segment than HCPV, LCPV has attracted high-quality commercial representation. While all concentrator optics are constrained by the physics of reflection refraction and total internal reflection (TIR), within these limits the relatively new field of non-imaging optics (NIO) pioneered by Welford and Winston added an opportunity for innovation [21]. Significant performance and manufacturability improvements have been realized by applying NIO, and the pathway to practical, deliverable products has become much more navigable. As a result, many new CPV companies have worked to merge NIO with the new cells, and a large range of designs have recently appeared at both ends of the concentration range, further contributing to what was an already well-prototyped field. Today, the leading companies in CPV have matured their products, have commissioned high-volume production lines and have amassed large amounts of data from operating installations. The focus for many of these companies is now on proving their bankability and product reliability, as larger commercial opportunities become available. Currently, there are over 20 active CPV companies. After a long gestation, CPV is starting to meet its promise. Swanson declared that CPV is “a long range option of vital importance to the energy security of the world” [18]. Cost analyses indicate that it certainly has the possibility of becoming the low-cost PV approach in large installations.

1.9. Effects of temperature

The solar irradiation that is falling onto a solar cell is not fully converted into electrical energy. The electrical energy is removed from the cell through the external circuit; however, the thermal energy is dissipated by heat transfer mechanisms. In a solar cell, at a fixed irradiation level, increasing cell temperature leads to decreased open-circuit voltage and a slightly increased short-circuit current. The I_{sc} increases with temperature because the band gap energy decreases and more photons have enough energy to create electron-hole pairs but this effect is small. The main effect of increasing temperature for solar silicon cells is the reduction of V_{oc} and the fill factor. Therefore the overall effect is the reduction of the cell output leading to the reduction of the efficiency of the module. To get rid of this, heat transfer from the module should be maximized so that the cells will operate at the lowest possible temperatures, yet our approach in this thesis is to use a spectral splitting filter to reduce the temperature of the cell.

At high concentration of irradiation level, the cell reaches higher cell temperature, which reduces the output voltage. Therefore cooling is often required for concentrating solar systems. The effect of temperature on the (I–V) characteristics of a solar cell is shown in Fig. 1-9.

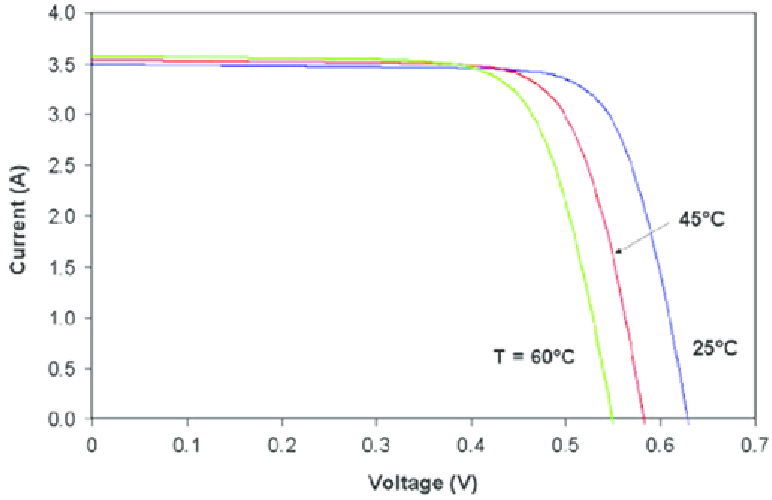

Fig. 1- 9: The effect of temperature on the *I–V* characteristics of a solar cell.

1.10. Heat sinks in CPV (conventional cooling)

A crucial point in the operation of HCPV is the removal of energy dissipated as heat in the solar cell (almost 60% in multijunction solar cells) which may become substantial when the concentration levels is high which can decrease the performance of the solar cell and the system drastically. This elevated temperature accelerates many failure modes; especially for materials such as adhesives or encapsulants which have a fairly low temperature tolerance, but are otherwise desirable in the CPV module. As general rule the power production decrease by 0.2% for each °C increase in temperature. Beside the power production the reliability of the solar cell decrease drastically with temperature increase. In order to avoid performance degradation, appropriate cell packaging and cooling are necessary. Two different options are generally considered for removing the residual thermal power namely:

1) Passive cooling, which is usually based on simple natural convection heat transfer between the converter and the ambient (simple, reliable, and requires neither maintenance nor use of energy consuming devices) [22].

2) Active cooling, which generally involves forced motion of a cooling fluid (thermal power to remove becomes significant, i.e. when the dimensions of the cell or the illumination level (or both) is increased).

The device used in both cases is called heat sink and different configurations and designs are usually used but they all use the same previously mentioned two concepts as shown in Fig. 1-10.

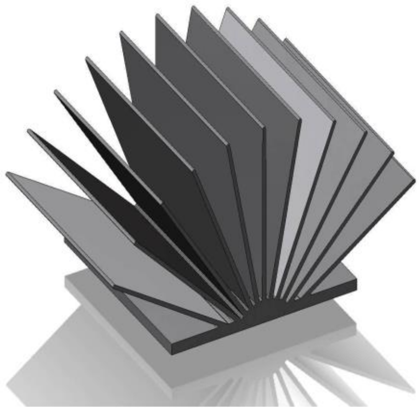

(a) passive cooling heat sink design with fins [22].

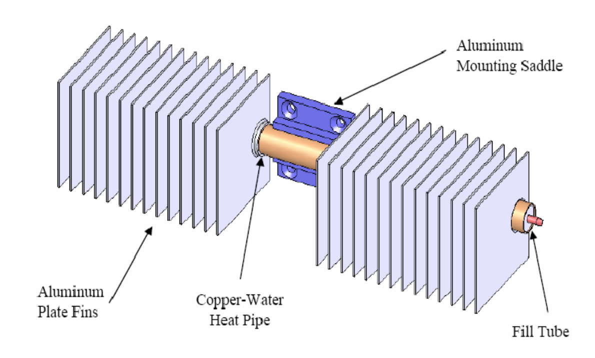

(b) Active cooling heat pipe cooling heat sink system schematic [23].

Fig. 1- 10: Different heat sinks designs examples.

While these concepts are usually considered the conventional ways for temperature reduction in CPV systems a new concept for heat reduction is introduced in this thesis which has never been studied before as an efficient way for heat reductions in solar cells. This concept is spectral splitting which is usually studied as a way of increasing the total conversion efficiency of a solar conversion system by combining two types of receiver (PV and thermal receivers or different types of PV cells). Nevertheless, we consider this study the first detailed study that illustrate the effect of spectrum splitting on the thermal performance and temperature reduction in a CPV system.

1.11. Spectral splitting in CPV system

Photovoltaic conversion is highly wavelength-dependent and most efficient when converting photons which have energy close to the PV cell band-gap energy. Photons below the band-gap energy are not absorbed in the active cell area, and just dissipated as heat on the rear surface or other parts of the cell. Photons of energy larger than the bandgap can only be partly utilized, and the remainder of their energy is dissipated as heat through thermal relaxation.

One way to optimize the performance of solar cells is by only allowing the part of the solar spectrum for which high conversion efficiency can be achieved to reach the solar cell. The optimization is done by either redirecting the spectrum outside of solar cell efficient spectrum to a second receiver, thus increasing the total system efficiency as in PV/thermal solar hybrid systems. We could also just reflect the unutilized spectrum away from the solar cell thus cutting the solar spectrum for which high conversion efficiency can't be achieved. This ultimately reduces the temperature of cell due to the reduction in energy dissipated as heat in the solar cell. An example of spectral splitting system us shown in Fig. 1-11.

The main filtering techniques for PV cells are characterized into different categories. These categories are; all-dielectric and metal-dielectric multilayer filters [24-26]. Heat reflectors [27, 28], refraction or prism spectrum splitting [29-31], holographic filters [32-34], fluorescent methods [35-36], and liquid absorption filters [26, 38, 39]. In PV only systems, two basic filtering techniques can be carried out. One technique is using two or more solar cells of different semiconductor materials that are arranged in order of decreasing energy band-gap and mechanically or monolithically stacked in series [40-42].

The other technique is spectrum splitting in which an optical filter separates the light into spectral components and direct the different parts of spectrum onto individual cells of different band-gap energies [43-45]. In this research, we used the spectrum splitting thin-film optical filter approach to achieve our goal of temperature reduction.

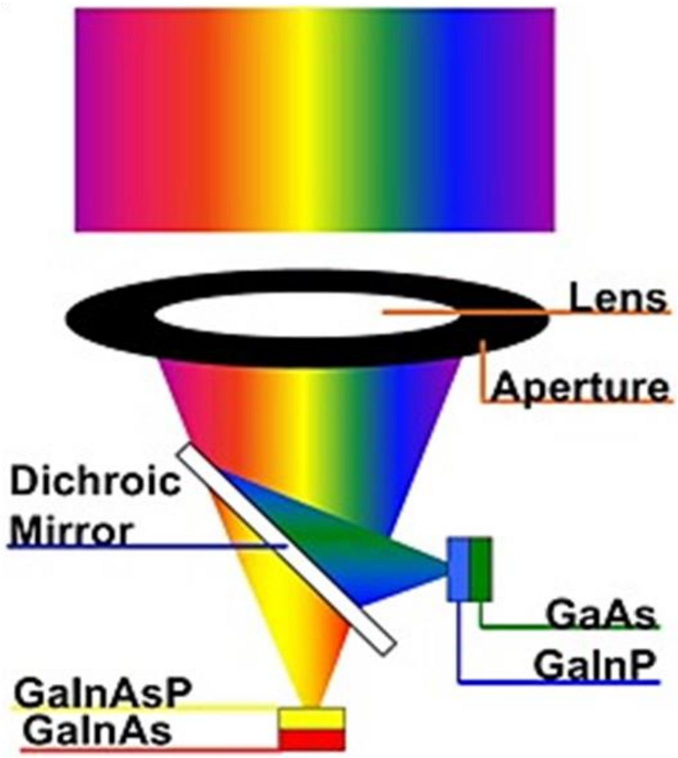

Fig. 1- 11: Spectral splitting example in CPV system [46].

1.12. Tracking systems in CPV

The primary benefit of a tracking system is to collect solar energy for the longest period of the day with the most accurate alignment to the Sun. Although solar tracking could provide more power output than a stationary PV panel, tracking is not always the ideal option since the trackers are more expensive than fixed PV panels. Solar trackers can adapt to the sun's change of location throughout the day, and across the seasons by tilting the panels according to the azimuthal and zenith angle of the sun. This leads to an increase in energy output and therefore in efficiency because solar panels are at peak efficiency when they are at a perfectly perpendicular angle with the sun.

In typical high concentration systems tracking accuracy must be in the ± 0.1º range, which mean that the tracker needs to move at least every minute and leads to large power consumption and complexity in the system design. On the other hand, low concentration systems, tracking accuracy must be in the ± 2.0º range. The difference between tracking technologies is down to tracking methods and algorithms used, which effects the needed tracking motor's accuracy and cost and as result the efficiency and cost of the system.

There are different types of trackers and different technologies but the system used in this thesis is azimuthal tracker in which motion is made by combining vertical rotation with an elevation motion. This is because the panel rotates around the vertical axis that is represented by the base [47].

If we can implement a tracking methodology in a CPV system that moves in longer intervals than one minute and can achieve the same performance for the CPV system this will lead to great decrease in the cost, complexity and power consumption of the system, and this is one of the main aims in this thesis.

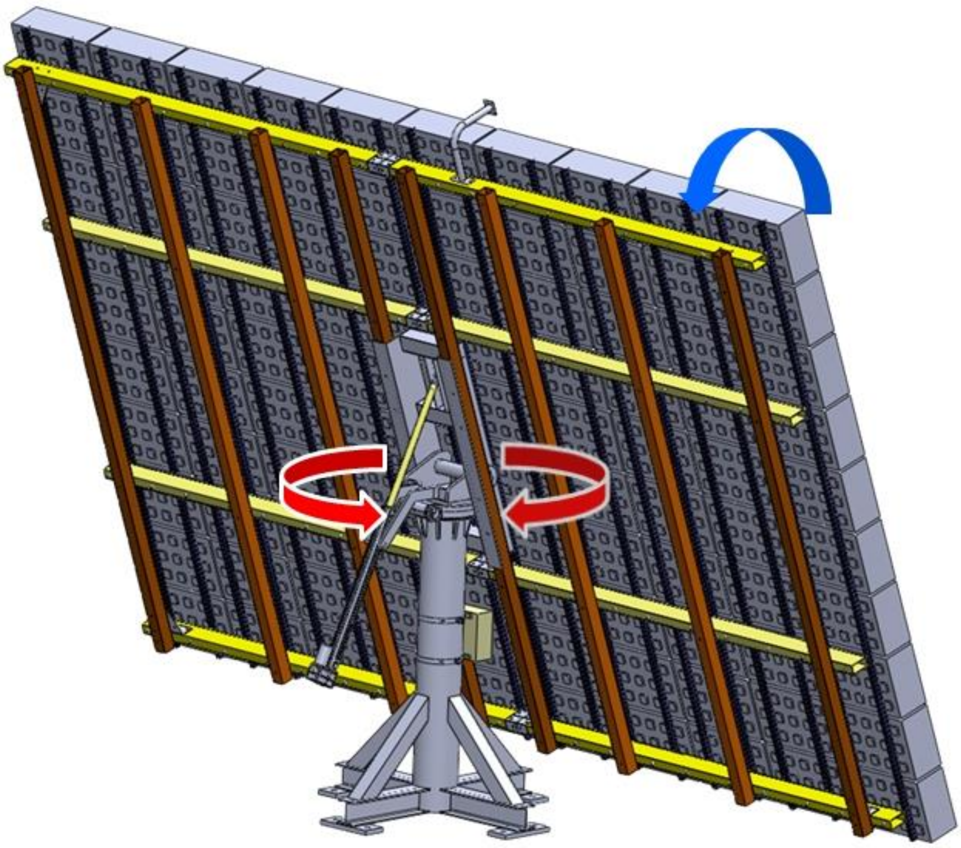

Fig. 1- 12: Dual Axis azimuthal tracker for CPV

1.13. Objective

The aim of this thesis is to examine and evaluate possible ways to improve the performance and cost of CPV systems using new improved techniques that can lead to enhancement of the overall system performance and cost.

Problem statement

1. Temperature increase in solar cells can reduce performance and reliability drastically in CPV systems. We are seeking to evaluate the benefits of using a new technique (thin-film filter) different from the conventional temperature decrease techniques (heat sinks) to reduce temperature and increase the lifetime of a solar cell.
2. The need for high precision tracking system (± 0.1°) in CPV add complexity to the system and extra cost and consume more energy because the system need to move every min to redirect the module toward the sun. To overcome this a new approach with wide-acceptance-angle CPV system and 30-min intermittent tracking system was implemented. System evaluation was conducted to prove that there would be no difference in the system performance even when the system is operating under the largest tracking error angle (low precision).

Based on the previously mentioned two problems we can conclude the objective of each chapter as follows:

Chapter 1

This chapter is the general introduction and the basic theoretical knowledge required to proceed into the next chapters of this thesis.

Chapter 2

The aim of this chapter is to explore the possibilities of using spectral splitting thin-films to improve the CPV performance by reducing the temperature of the concentrator multijunction solar cell which will allow the extension of the lifetime of the solar cell and the CPV system in general. The research makes a comparison of three-dimensional simulation for concentrator photovoltaic module using two types of multijunction solar cells. Each solar cell had its range of spectral response and based on that range a thin-film filter is developed for each case to reflect the unused solar spectrum and allow the desired spectrum to reach the solar cell. A thermal simulation is also conducted to compare the expected decrease in cell temperature and decide which system promises the best thermal performance using the thin-film filter.

Chapter 3

After deciding which system has the highest potentials for reducing the temperature of the solar cell the next stage of the research will be to improve the thermal model and evalute the electrical performance for this CPV system analysed in chapter 2. The use of the thin-film filter aims to reduce the temperature of the solar cell while obtaining almost the same electrical performance of the CPV system. A new improved thin-film filter was designed to meet the EQE requirements and the spectral sensitivity of the solar cell. A thermal simulation using COMSOL Multiphysics is also conducted to examine the impact of the thin-film filter on the temperature of the solar cell. The (*I*–*V*) current–voltage characteristics of the InGaP/GaAs/InGaAs triple junction solar cell under concentration conditions will be also analyzed using an equivalent circuit simulator to determine the effect of using the thin-film filter on the solar cell electrical performance. After evaluating of thermal and electrical performance, the next objective of this chapter is to assess the effect of temperature reduction on the lifetime of the solar cell. An average Arrhenius–Weibull model is built to calculate the unreliability and estimate the lifetime of the multijunction solar cell.

Chapter 4

This chapter objective is to prove that using wide-acceptance-angle CPV system with 30-min intermittent tracking system can achieve good performance for the CPV system even when using low precision tracking technology. The use of such low precision tracking system will lead to decrease in the system cost and complexity because a large percentage of the cost and complexity of a typical CPV system comes from the expensive accurate tracking system.

The first step in this chapter is to build an optical, thermal and electrical models for the high-acceptance-angle dielectric concentrator and compare the simulation results with experimental outputs of the real CPV module. Furthermore, the results will be discussed for the case with zero tracking error and the highest tracking error to establish a solid proof of the feasibility of using an intermittent tracking system for wide acceptance angles CPV systems. One new idea of this section will be to examine the heating in the focal point of the system and its effect on the optical properties of the used lens.

A sensitivity analysis for the silicone excessive sealing effect on the electrical performance will be also conducted to examine the degradation in electrical performance caused by this sealing.

Chapter 5

The present research is summarized, and potentials for future research improvement is discussed.

References

1) Web [https://mcouts2.com/how-does-the-trf-work/insolation-reflection/]
2) T. M. Letcher, Future energy: improved, sustainable and clean options for our planet (Elsevier, London, 2008) 1st ed., p. 376.
3) T. Markvart, Solar electricity (Energy engineering learning package) (Wiley, New York, 2000) 2nd ed., p. 290.
4) R. M. Swanson, The promise of concentrators, Prog. Photovoltaics **8**, 93-111 (2000).
5) A. Luque, Solar cells and optics for photovoltaic concentration, (A. Hilger, Bristol, 1989) p. 540.
6) R. Winston, J. C. Miñano, and P. Benítez, Nonimaging optics, (Elsevier , Boston, 2005) p. 503.
7) J. M. Gordon, E. A. Katz, W. Tassew, and D. Feuermann, Photovoltaic Hysteresis and its ramifications for concentrator solar cell design and diagnostics, Appl .Phys. Lett, **86**, 073508 (2005).
8) A. Braun, B. Hirsch, E. A. Katz, J. M. Gordon, W. Guter, and A. W. Bett, Localized radiation effects on tunnel diode transitions in multi-junction concentrator solar cells, Sol. Energy Mater. Sol. Cells **93**, **1692** (2009).
9) J. M. Olson, Simulation of nonuniform irradiance in multijunction III-V solar cells, 35^{th} IEEE Photovoltaic Specialists Conference (35-PVSC), 002066-002069, (2010).
10) D. C. Miller, M. D. Kempe, M.T. Muller, M. H. Gray, K. Araki, and S. R. Kurtz, Durability of polymeric encapsulation materials in a PMMA/glass concentrator photovoltaic system, Prog. Photovoltaics: Res. Appl. **24**, 1385 (2016).
11) M. Victoria, R. Herrero, C. Dominguez, I. Anton, S. Askins, and G. Sala, Characterization of the spatial distribution of irradiance and spectrum in concentrating photovoltaic systems and their effect on multi-junction solar cells, Prog. Photovoltaics: Res. Appl. **21**, 308 (2013).
12) O. Korech, B. Hirsch, E. A. Katz, and J. M. Gordon, High-flux characterization of ultrasmall multijunction concentrator solar cells. Appl. Phys. Lett. **91**, 064101, (2007).

13) S. Kurtz and M. J. O'Neill, Estimating and controlling chromatic aberration losses for twojunction, two terminal devices in refractive concentrator systems, Proc. 25th Photovoltaic Specialists Conf. (25-PVSC), [DOI: 10.1109/PVSC.1996.564020].
14) L.W. James, Effects of concentrator chromatic aberration on multi-junction cells, IEEE, 1st World Conference on Photovoltaic Energy Conversion – WCPEC, [DOI: 10.1109/WCPEC.1994.520652].
15) K. Araki, M. Kondo, H. Uozumi, and M. Yamaguchi, Experimental proof and theoretical analysis on effectiveness of passive homogenizers to 3J concentrator solar cells, Proc. 3rd World Conference on Photovoltaic Energy Conversion, 2003 p. 853.
16) I. García, P. Espinet-Gonz lez , I. Rey-Stolle, and C. Algora, Analysis of Chromatic Aberration Effects in Triple-Junction Solar Cells Using Advanced Distributed Models, IEEE Photonics Technol. Lett. **1**, 219 (2011).
17) A. Rosenthal and C. Lane, Field test results for the 6MW Carrizo solar photovoltaic power plant, Solar Cells. **30**, 563 (1991).
18) R. Swanson, in *Handbook of Photovoltaic Science*, eds. A. Luque and S. Hegedus, (John Wiley & Sons, Ltd, Chichester, 2003) p. 449.
19) G. Sala and A. Luque, in *Concentrator photovoltaics*, eds. A. Luque, V. Andreev, (Springer-Verlag Berlin Heidelberg, Berlin, 2007) p. 1.
20) N. Miyashita, Y. Shimizu, and Y. Okada, Effect of increasing nitrogen composition on the performance of GaAs/GaInNAs heterojunction solar cells, Proc. 22nd European Photovoltaic Solar Energy Conf, 2007, p. 414.
21) W. Welford and R. Winston, High collection nonimaging optics, (Academic Press, London, 1989).
22) F. Gualdi, O. Arenas, A. Vossier, A. Dollet, V. Aimez, and R. Arès, Determining Passive Cooling Limits In CPV Using An Analytical Thermal Model, AIP Conf. Proc, 1556, 10 (2013).
23) W. G. Anderson1, S. Tamanna, D. B. Sarraf, and P. M. D, Heat Pipe Cooling of Concentrating Photovoltaic (CPV) Systems, 33rd IEEE Photovoltaic Specialists Conf. (PVSC), [DOI: 10.1109/PVSC.2008.4922577].
24) L. DeSandre, Y.D. Song, H.A. Macleod, M.R. Jacobson, and D.E. Osborn, Thin-film multilayer filter designs for hybrid solar energy conversion systems,

Proc. SPIE : Optical Materials Technology for Energy Efficiency and Solar Energy Conversion IV. **562**, 159 (1985).
25) D. E. Osborn, M. A. C. Chendo, M. A. Hamdy, F. Luttmann, M. R. Jacobson, H. A. Macleod, R. Swenson, Spectral selectivity applied to hybrid concentration systems, Sol. Energy Mater. **14**, 299 (1986).
26) M. A. C. Chendo, M. R. Jacobson, and D.E. Osborn, Liquid and thin-film filters for hybrid solar energy conversion systems, Sol. Wind Technol. **4**, 131 (1987).
27) J. C. C. Fan and F. J. Bachner, Transparent heat mirrors for solar-energy applications, Appl. Opt. **15**, 1012 (1976).
28) D. E. Soule and S.E. Wood, Heat-mirror spectral profile optimization for TSC hybrid solar conversion, Proc. SPIE Optical Materials Technology for Energy Efficiency and Solar Energy Conversion V, **653**, 172 (1986).
29) S. R. Clark, US Patent, US4350837 A (1982).
30) U. Ortabasi, A hardened solar concentrator system for space power generation: photovoltaic cavity converter (PVCC), Space Technol Ind Commer Appl, **13**, 513 (1993).
31) J. P. Penn, US Patent, US6469241 B1(2002).
32) S. McGrew, Color control in dichromated gelatin reflection holograms, Proc. SPIE, Recent Advances in Holography, **215**, 24 (1980).
33) W. H. Bloss , M. Griesinger, and E. R. Reinhardt, Dispersive concentrating systems based on transmission phase holograms for solar applications, Appl. Opt. **21**, 3739 (1982).
34) J. E. Ludman, J. Riccobono, I. V. Semenova, N. O. Reinhand, W. Tai, X. Li, G. Syphers, E. Rallis, G. Sliker, and J. Martin, The optimization of a holographic system for solar power generation, Sol. Energy Mater. **60**, 1 (1997).
35) P. Gravisse and M. Prevot, US Patent, US3912931 A (1975).
36) A. Gotzberger, W. Greubel, Solar energy conversion with fluorescent collectors, Appl. Phys. **14**, 123 (1977).
37) F. Galluzzi and E. Scafe, Spectrum shifting of sunlight by luminescent sheets: performance evaluation of photovoltaic applications, Sol. Energy. **33**, 507 (1984).
38) R. A. Powell, US Patent US4278829 A (1981).
39) M. Sabry, R. Gottschalg, T. R. Betts, M. A. M. Shaltout, A. F. Hassan, M .M. El-

Nicklawy, and D. G. Infield, Optical filtering of solar radiation to increase performance of concentrator systems, Proc. 29th IEEE Photovoltaic Specialists Conference, 2002 , p. 1588.

40) E. D. Jackson, US Patent US2949498 A (1960).

41) J. J. Loferski, Tandem photovoltaic solar cells and increased solar energy conversion efficiency, Proc. 12th IEEE Photovoltaic Specialists Conference (PVSC), 1976, p. 957.

42) M. F. Lamorte and D. Abbott, Two-junction cascade solar cell characteristics under 1000 concentration ratio and AM0-AM5 spectral conditions, Proc. 13th IEEE Photovoltaic Specialists Conference (PVSC), 1978, p. 874.

43) M. Wolf, Limitations and possibilities for improvements of photovoltaic solar energy converters, Proc. Institute of Radio Engineers, **48**, 1960, p. 1246.

44) G. W. Masden and C. E. Backus, Increased photovoltaic conversion efficiency through use of spectrum splitting and multiple cells, Proc. 13th IEEE Photovoltaic Specialists Conference (PVSC), 1978, p. 853.

45) J. R. Onffroy, D. E. Stoltzmann, R. J. H. Lin, and G. R. Knowles, High-efficiency concentration/multi solar-cell system for orbital power generation, Proc. 15th Intersociety Energy Conversion Engineering Conference, 1980, p. 371.

46) X. Wang, N. Waite, P. Murcia, K. Emery, M. Steiner, F. Kiamilev, K. Goossen, C. Honsberg, and A. Barnett, Lateral spectrum splitting concentrator photovoltaics: direct measurement of component and submodule, Prog. Photovoltaics **20**, 149 (2011).

47) Web [http://www.macsunsolar.com/en/showpro.php?id=143]

Chapter 2

Designing of long wavelength cut thin-film filter for temperature reduction of concentrator photovoltaic

2.1. The concept of the system

In this chapter, we present a three-dimensional simulation for concentrator photovoltaic module using two types of multijunction solar cell. Each had its own range of spectral response and based on that range a thin-film filter was developed for each case to reflect the unused spectral wavelength range of the solar spectrum and allow the desired spectrum to reach the solar cell. The first solar cell was InGaP/InGaAs/Ge triple junction solar cell with high spectral response in the wavelength range from 400−1700 nm [1]. The second solar cell was InGaP/GaAs/InGaAs triple junction solar cell with high spectral response in the wavelength range of 400−1100 nm [2]. The thin-film was deposited on a secondary optical element that was used to homogenize the irradiance distribution on the solar cell. The systems' geometrical concentration ratio was 1322 times. A thermal simulation was conducted to compare the resulted decrease in cell temperature due to the use of the thin-film for each case.

2.2. The system design

2.2.1. The optical model design

Ray-Trace calculation was conducted for the optical system using commercial optical simulation software ZEMAX (ZEMAX LLC.). The optical system consists of typical flat Fresnel lens as a primary optical element with dimensions of 200 mm × 200 mm as incident ray area (focal length = 420 mm), and secondary optical element (homogenizer).

Figure 2-1 shows the schematic diagram of the CPV optical structure. The homogenizer (14 mm × 14 mm as entry aperture area, 5.5 mm × 5.5 mm as exit aperture area, and 40 mm in height) was set at the focal point of the Fresnel lens. The used thin-film was deposited at the entry aperture of the homogenizer, and the resulted intensity distribution of the concentrated light was analyzed. The distance between Fresnel lens and the solar cell was 460 mm. The geometrical concentration ratio for this system was 1322 times. The spectral irradiance used in ray tracing simulation was AM 1.5D (total power: 900 W/m^2) [3]. Ray trace was carried out in the wavelength from 300 to 2500 nm to show the effect of using the thin-film on the overall performance of the system.

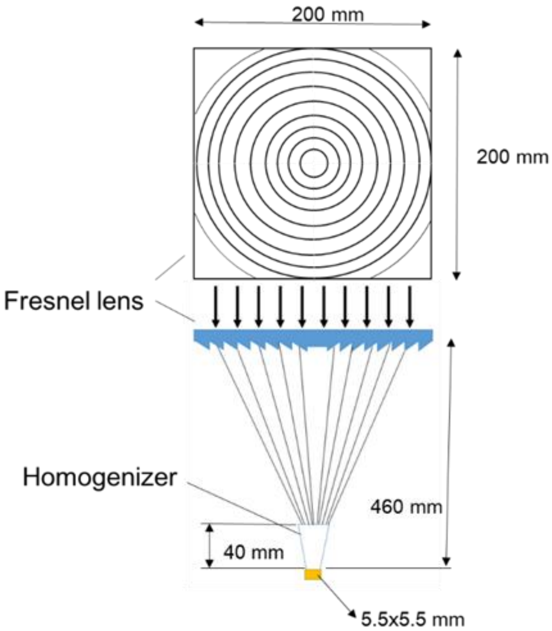

Fig. 2- 1: Schematic Diagram of the CPV optical structure.

2.2.2. The thin-film design

For designing the thin-film there were different traditional optimization methods widely accepted and used. Nevertheless most used optimization techniques for thin-film are greatly affected by the initial structure of the used film, which may cause a local convergence. To design the thin-films we used powerful thin-film optimization technique called needle optimization method which was developed by Tikhonravov et al. [4, 5]. This design method optimizes the thin-film structure in such a way that the starting point is irrelevant. The main idea of the needle optimization technique is that its algorithm identifies the proper places to insert new layers that will improve the merit function. The algorithm will also identify which layer material, from a preselected group of materials, will provide the greatest improvement.

The calculations will measure the corresponding numerical value between actual and desired spectral characteristics which define the merit function. The smaller the merit function the closest the reached design is to the targeted performance. The merit function was defined by the following equation

$$\delta F = P_1(z,n)\delta + P_2(z,n)\delta^2 + \cdots, \qquad (2.1)$$

where δ is the thickness and n is the refractive index of a new layer, z is the location of the layer insertion. Needle optimization technique has an analytic algorithm that allows the calculation of the change in the merit function as a function of the index and position of a new layer without the actual insertion of a new layer [6]. The algorithm is rather complicated but it is extremely efficient from the computational point of view. The function P identifies the most appropriate position to insert new layers within the existing design and determine which of the available materials is the best choice for the new layer:

$$P(z) = min_{1<j<J} P_j(z, n_j). \qquad (2.2)$$

The places where the P function is negative may be considered appropriate places for the insertion of new layers. Figure 2-2 shows the needle optimization synthesis procedure.

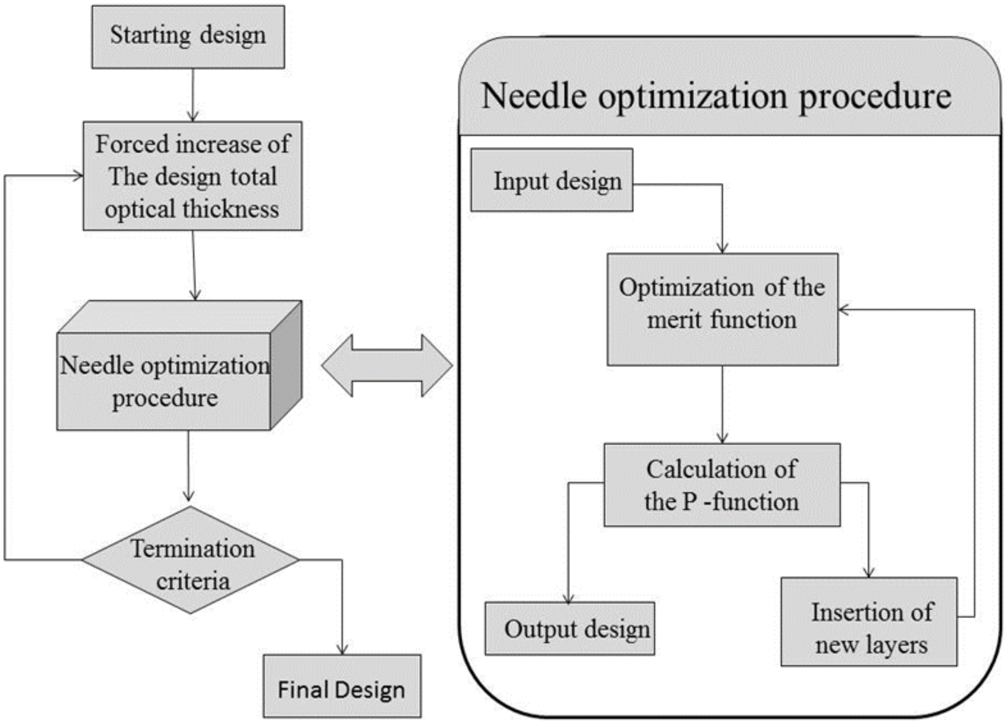

Fig. 2- 2: Schematic of the gradual evolution approach enhanced with the needle optimization technique.

The optical constants for the two materials are shown in Table 2-1 and Table 2-2, respectively. The two materials used in designing the filter are high refractive index material (in our case TiO_2), and low refractive index material (in our case SiO_2).

Table 2- 2: Optical constants for TiO_2 film at different wavelength (nm).

Wave	**400**	**430**	**450**	**500**	**550**	**600**	**700**	**800**	**900**
n	2.397	2.313	2.27	2.210	2.177	2.160	2.147	2.146	2.148
k	0.002	0.002	0.00	0.002	0.002	0.002	0.002	0.002	0.002

Table 2- 1: Optical constants for SiO_2 film at different wavelength (nm).

Wave	**350**	**400**	**450**	**500**	**550**	**600**	**650**	**700**	**900**	**1562**
n	1.472	1.467	1.463	1.459	1.455	1.452	1.450	1.446	1.434	1.429
k	0	0	0	0	0	0	0	0	0	0

Using needle optimizing and TFcalc (commercial thin-film design software), we developed two filters; the first filter was used for the InGaP/InGaAs/Ge triple junction solar cell concentrator module and it only allowed the spectrum in the range from 400−1700 nm to be transmitted onto the solar cell while reflecting the rest of the long wavelength spectrum.

The resulted structure consisted of 65 layers and had a thickness of 3490.4 nm. The thin-film structure is shown in Table 2-3 as follows:

Table 2- 3: The 1700 nm cutoff thin-film layers design.

Layer No.	Material	Thickness [nm]	Layer No.	Material	Thickness [nm]
1	SiO_2	731.37	16	TiO_2	10.89
2	TiO_2	4.15	17	SiO_2	42.16
3	SiO_2	36.04	18	TiO_2	6.5
4	TiO_2	5.42	19	SiO_2	254.28
5	SiO_2	22.65	20	TiO_2	6.41
6	TiO_2	7.46	21	SiO_2	39.05
7	SiO_2	17.42	22	TiO_2	9.16
8	TiO_2	9.99	23	SiO_2	18.17
9	SiO_2	12.16	24	TiO_2	20.3
10	TiO_2	16.17	25	SiO_2	13.99
11	SiO_2	11.12	26	TiO_2	130.37
12	TiO_2	111.53	27	SiO_2	15.79
13	SiO_2	14.33	28	TiO_2	25.23
14	TiO_2	20.22	29	SiO_2	42.99
15	SiO_2	20.39	30	TiO_2	10.24

Layer No.	Material	Thickness [nm]	Layer No.	Material	Thickness [nm]
31	SiO_2	250.9	49	SiO_2	15.96
32	TiO_2	8.42	50	TiO_2	7.22
33	SiO_2	44.82	51	SiO_2	40
34	TiO_2	23.89	52	TiO_2	4.06
35	SiO_2	15.7	53	SiO_2	274.14
36	TiO_2	137.42	54	TiO_2	5.24
37	SiO_2	15.15	55	SiO_2	32.43
38	TiO_2	23.01	56	TiO_2	7.28
39	SiO_2	43.1	57	SiO_2	14.9
40	TiO_2	8.07	58	TiO_2	19.55
41	SiO_2	260.08	59	SiO_2	6.57
42	TiO_2	8.52	60	TiO_2	135.53
43	SiO_2	41.91	61	SiO_2	14.98
44	TiO_2	24.87	62	TiO_2	14.43
45	SiO_2	14.18	63	SiO_2	25.97
46	TiO_2	130.73	64	TiO_2	11.64
47	SiO_2	14	65	SiO_2	93.2
48	TiO_2	16.6			

where the first layer was deposited on BK7 substrate. The transmittance of this 1700 nm cutoff filter is illustrated in Appendix A. As for the thin-film filter used for the InGaP/GaAs/InGaAs triple junction solar cell, it transmitted the spectrum in the range from 400−1100 nm and reflected the rest of the long wavelength spectrum. This thin-film consisted of 91 layers with a total thickness of 4551.6 nm. The transmittances of this cutoff thin-film is described in Appendix B.

The structure of this thin-film is described in Table 2-4. Figure 2-3 shows the transmittance for the two thin-films.

Table 2- 4: The 1100 nm cutoff thin-film layers design.

Layer No.	Material	Thickness [nm]	Layer No.	Material	Thickness [nm]	Layer No.	Material	Thickness [nm]
1	TiO_2	6.61	32	SiO_2	6.26	63	TiO_2	112.5
2	SiO_2	38.65	33	TiO_2	23.86	64	SiO_2	11.72
3	TiO_2	12.67	34	SiO_2	32.29	65	TiO_2	16.24
4	SiO_2	22.3	35	TiO_2	11.67	66	SiO_2	15.77
5	TiO_2	14.71	36	SiO_2	215.82	67	TiO_2	8.43
6	SiO_2	22.05	37	TiO_2	15.27	68	SiO_2	34.97
7	TiO_2	12.98	38	SiO_2	26.04	69	TiO_2	3.96
8	SiO_2	29.1	39	TiO_2	117.25	70	SiO_2	212.15
9	TiO_2	9.05	40	SiO_2	15.75	71	SiO_2	40.78
10	SiO_2	50.39	41	TiO_2	17.37	72	TiO_2	7.27
11	TiO_2	2.82	42	SiO_2	33.9	73	SiO_2	36.94
12	SiO_2	452.84	43	TiO_2	5.67	74	TiO_2	12.97
13	TiO_2	9.08	44	SiO_2	488.99	75	SiO_2	20.45
14	SiO_2	38.66	45	TiO_2	6.05	76	TiO_2	18.94
15	TiO_2	25.18	46	SiO_2	25.1	77	SiO_2	15.28
16	SiO_2	12.45	47	TiO_2	12.21	78	TiO_2	24.33
17	TiO_2	133.25	48	SiO_2	14.93	79	SiO_2	13.48
18	SiO_2	7.69	49	TiO_2	110.92	80	TiO_2	22.01
19	TiO_2	22.55	50	SiO_2	26.71	81	SiO_2	19.22
20	SiO_2	30.71	51	TiO_2	13.4	82	TiO_2	12.64
21	TiO_2	9.82	52	SiO_2	198.49	83	SiO_2	38.5
22	SiO_2	230.37	53	TiO_2	11.95	84	TiO_2	7.59
23	TiO_2	7.52	54	SiO_2	22.79	85	SiO_2	225.89
24	SiO_2	49.58	55	TiO_2	107.25	86	TiO_2	6.98
25	TiO_2	17.06	56	SiO_2	25.24	87	SiO_2	39.31
26	SiO_2	27.69	57	TiO_2	15.31	88	TiO_2	11.67
27	TiO_2	25.03	58	SiO_2	212.5	89	SiO_2	45.42
28	SiO_2	18.8	59	TiO_2	9.62	90	TiO_2	12.05
29	TiO_2	31.87	60	SiO_2	19.36	91	SiO_2	106.47
30	SiO_2	9.84	61	TiO_2	10.88			
31	TiO_2	150.55	62	SiO_2	12.95			

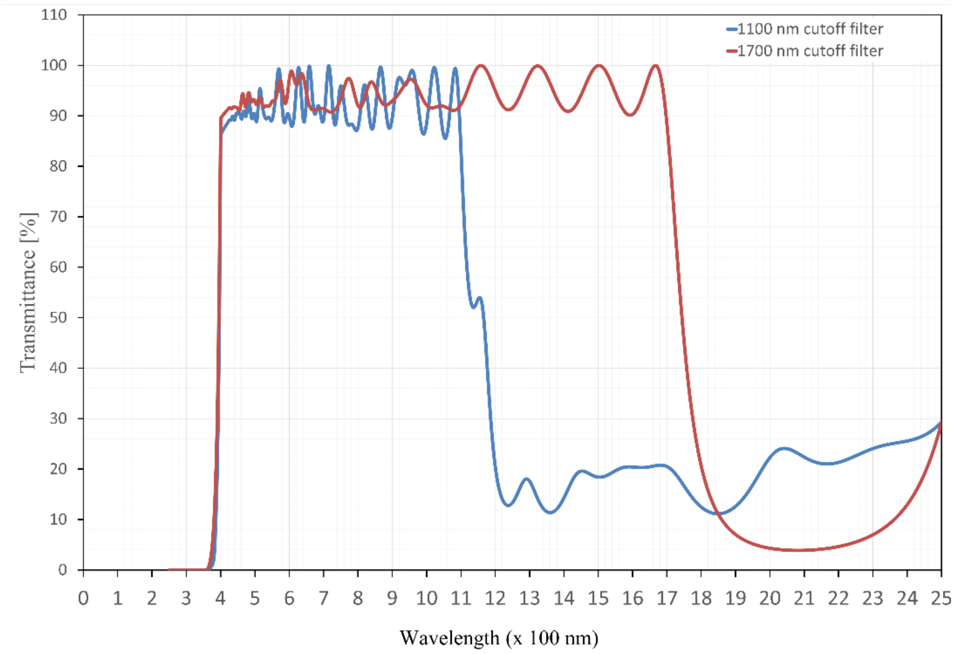

Fig. 2- 3: Thin-film transmittance curve as a function of wavelength.

2.2.3. The thermal model design

Heat transfer simulation for the CPV module was carried out using COMSOL Multiphysics. Figure 2-4 shows the geometry model developed for the calculations of heat transfer in the CPV module. The receiver consisted of homogenizer, III-V solar cell, a solder, a copper electrode, insulation materials and aluminum stage which was mounted on the aluminum chassis. I. Antón et al. [7] reported that the cell temperature (T_{cell}) could be related to the module temperature (temperature at the back surface of CPV module) through:

$$T_{cell} = T_{module} + R_{th\_cell\_heatsink} \cdot P, \quad (2.3)$$

where T_{module} (K) is module temperature at the back surface, $R_{th\_cell\_heatsink}$ (K/W) is thermal resistance between the cell and the back chassis or heat sink core, and P (W) is the heat power, respectively. The heat power was related to the direct normal irradiance (DNI) through:

$$P = DNI \cdot A_{\text{cell}} \cdot C \cdot \eta_{\text{op}} \cdot (1 - \eta), \tag{2.4}$$

where A_{cell} is the solar cell area, C is the concentration ratio, η_{op} is the optical efficiency, and η is the electrical efficiency. A_{cell} was fixed to 5.5 × 5.5 mm^2. The initial temperature was 300 K.

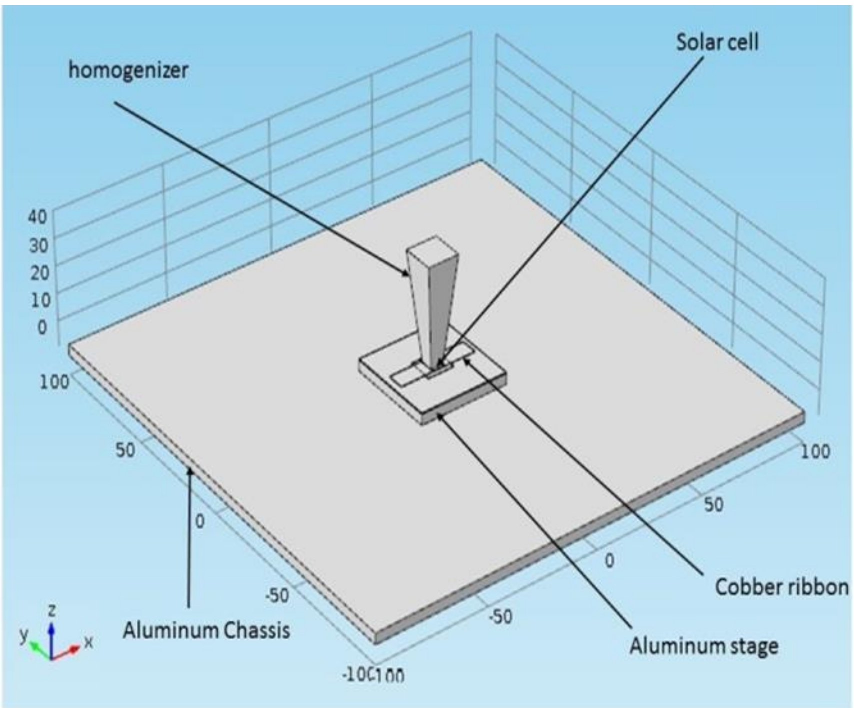

Fig. 2- 4: Simple geometry module for the heat transfer simulation.

The thickness and dimensions of the different structure layers around the solar cell are shown in Table 2-5.

Table 2- 5: Details of the structure around the solar cell.

Layer name	Thickness (mm)	Dimensions (mm × mm)
Solar cell	0.2	5.5×7.5
Solder 1	0.1	35×7.5
Copper ribbon	0.12	35×7.5
Solder 2	0.1	35×7.5
Cu-Zn layer	0.3	12×11
Insulation sheet	0.5	40×40
Aluminum stage	4	40×40
Insulation layer	0.9	40×40
Aluminum chassis	4	200×200

2.3. Results and discussion

2.3.1. Optical simulation

Using Ray-Trace simulation we analyzed the irradiance distribution on the solar cell for three cases. The first case was without thin-film on the homogenizer face, the second case was using 1700 nm cutoff thin-film filter, and the third case was when using a 1100 nm cutoff thin-film filter. Figure 2-5 shows the irradiance distribution on the solar cell for these three cases.

The results showed good irradiance uniformity due to the use of homogenizer in all three cases. The peak irradiance value in the optical model without the thin-film was 1.076×10^6 W/m^2 and the peak to average irradiance ratio (PAR) was equal to 1.071. As for the model with 1700 nm cutoff wavelength thin-film the peak irradiance value was 1.019×10^6 W/m^2 and PAR = 1.067. For the last case with 1100 nm cutoff wavelength thin-film the calculated peak irradiance on the solar cell was 8.786×10^5 W/m^2 and PAR value was 1.091. The previous results indicate that the best irradiance uniformity was obtained for the module with 1700 nm cutoff wavelength thin-film because it had the lowest PAR value although the lowest peak irradiance value was for the module with 1100 nm cutoff wavelength thin-film. It seems that the thin-film selective characteristics, depending on the wavelength and the optical spectral matching, in the range of 400–1100 nm had a much higher effect on the uniformity of the resulted irradiance distribution than in the case of the filter with 1700 nm cutoff. The optical efficiency for the system without thin-film was 84.4%. This optical efficiency decreased to 80.29% for the system with 1700 nm cutoff thin-film filter and to 67.72% for the system with 1100 nm cutoff thin-film filter.

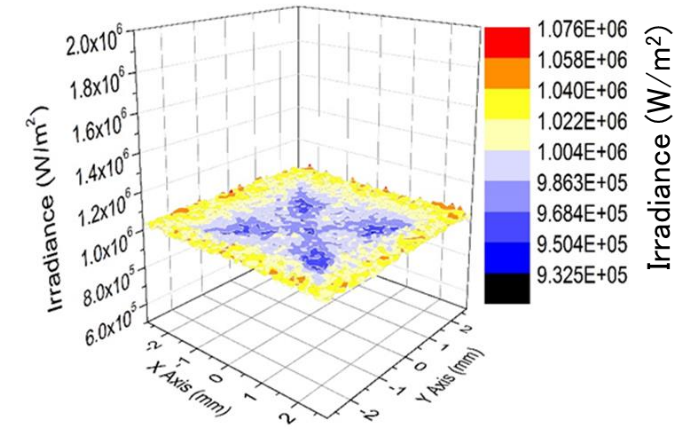

a) Without thin-film filter.

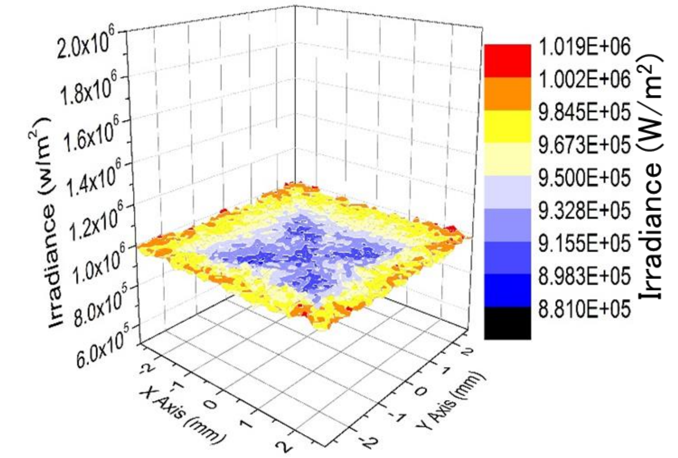

b)1700 nm cutoff thin-film filter.

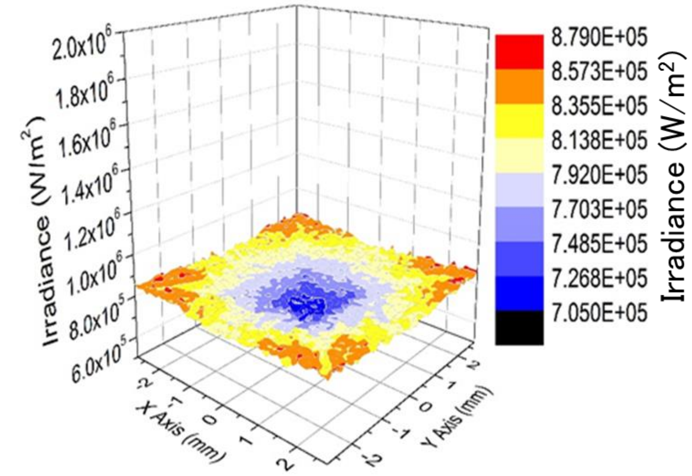

c)1100 nm cutoff thin-film filter.

Fig. 2- 5: Calculated irradiance distribution on the solar cell surface.

2.3.2. Thermal simulation

The results of thermal simulation for the three cases showed that the highest temperature was for the model without thin-film with the maximum temperature for the solar cell reaching to about 118.7°C as shown in Fig. 2-6(a). The highest temperature was concentrated in the center of the solar cell, and it decreases gradually toward the edges.

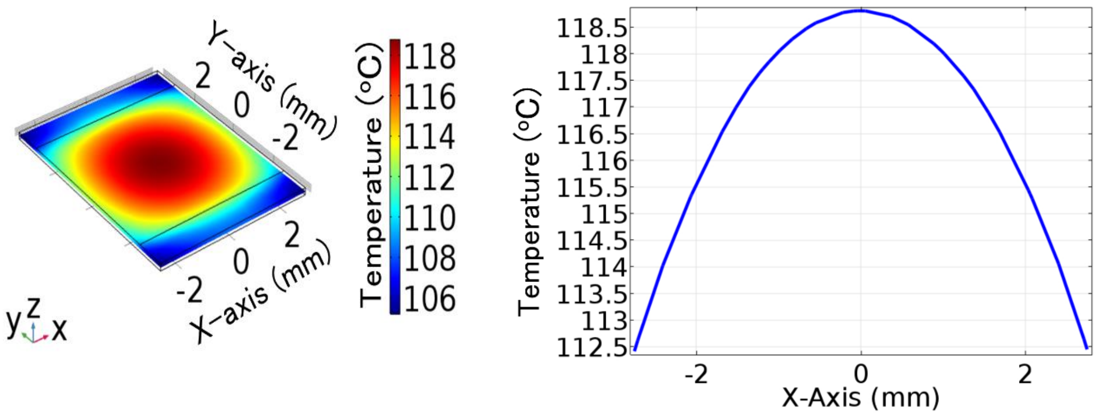

(a) Solar cell Temperature distribution.

(b) Temperature change across the X- axis of the Solar cell.

Fig. 2- 6: Thermal simulation results for the model without thin-film filter.

The total change in temperature across *x*-axis at $y = 0$ was 6.2°C and it ranged between 118.7°C and 112.5°C as shown in Fig. 2-6(b).

When using 1700 nm cutoff wavelength thin-film, the temperature dropped to 114.5°C with a total drop of about 4°C in temperature compared to the model without thin-film. The temperature distribution on the solar cell surface and the temperature change across the *x*-axis of the solar cell are shown in Fig. 2-7(a) and 2-7(b), respectively. Results showed that the temperature change across the solar cell surface was 5.5°C.

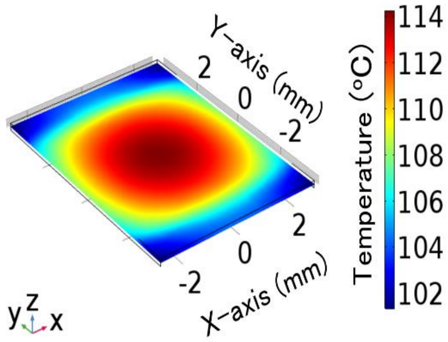

(a)

Solar cell Temperature distribution.

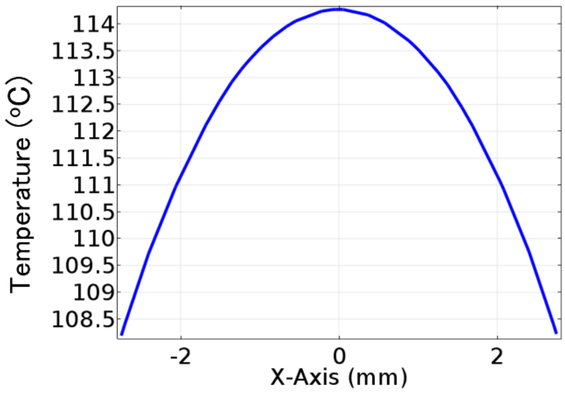

(b)

Temperature change across the X- axis of the Solar.

Fig. 2- 7: Thermal simulation results for the model with 1700nm cutoff thin-film filter.

The best thermal performance was achieved by the model with 1100 nm cutoff wavelength thin-film where the temperature decreased by 18.2°C compared to the model without thin-film filter and reached to 100.5°C. The temperature distribution on the surface of the solar cell is shown in Fig. 2-8(a), while Fig. 2-8(b) shows the change in temperature across the *x*-axis in the center of the solar cell (y = 0). The temperature reduction in this model was very high, which would definitely lead to better electrical performance. The change in temperature across the surface of the solar cell as shown from Fig. 2-8(b) was less than the last two cases with temperature varying between 100.5°C and 95.5°C, which mean only 5°C difference across the surface of the solar cell was accomplished by using thin-film cutoff filter.

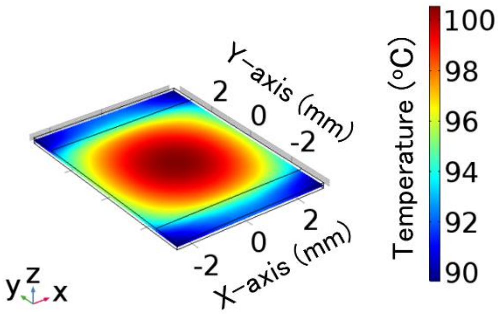

(a)

Solar cell Temperature distribution.

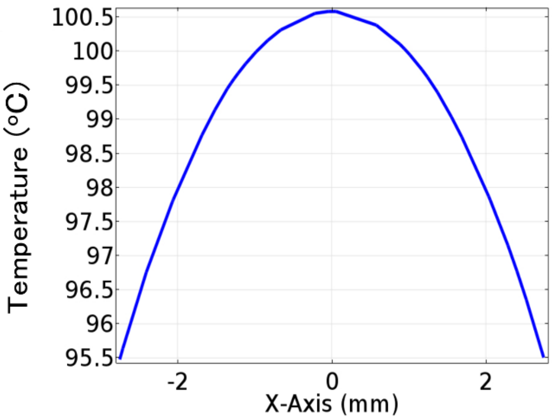

(b)

Temperature change across the X- axis of the Solar.

Fig. 2- 8: Thermal simulation results for the model with 1100nm cutoff thin-film filter.

2.4. Conclusion

Results showed that it is possible to cut the part of the solar spectrum which is not utilized and converted mostly into heat in the solar cell, using a thin-film filter that we designed based on the spectral response range of two types of multijunctions solar cells. The use of such thin-film filter was proven to result in a significant reduction in the solar cell temperature although the used thin-film filter area (14 mm × 14 mm) was very small which mean reduction in the total cost of the designed filter.

Results indicated a degradation in the solar irradiance distribution uniformity on the surface of the solar cell when using cutoff thin-film filter. Nevertheless, peak to average irradiance ratio was within the accepted values. The best irradiance uniformity was on the solar cell in the model with wavelength 1700 nm cutoff filter with a PAR value of 1.067. The heat transfer simulation showed excellent performance for the solar cell when using a 1100 nm cutoff filter with a temperature drop by 18.2°C compared to the case without thin-film filter; this indicated the feasibility of using the thin filter for temperature reduction in the solar cell. Another benefit, which was observed, was better uniformity in temperature distribution and less change across the surface of the cell when using thin-film filter which can lead to better electrical performance. These results led us to conclude that cutting the unutilized spectrum in the solar cell would result in a large decrease in the temperature of the solar cell by using a simple technique as depositing a thin-film filter on the surface of the homogenizer.

The previous results showed that the best performance was achieved by the CPV system, which uses InGaP/GaAs/InGaAs triple-junction solar cell with thin-film cutoff filter that allows only the spectrum in the range of 400–1100 nm to reach the solar cell.

This evaluation led us to decide that the system with 400-1100 nm cutoff thin-film filter has the highest potential for further development and thus a more detailed study of thermal and electrical performance will be pursued in the next chapter of this doctoral thesis. The next chapter will also include an evaluation of the lifetime of the used CPV system and the effect of temperature reduction on reliability and electrical performance of the system.

References:

1) W. Guter, J. Schöne, S. P. Philipps, M. Steiner, G. Siefer, A. Wekkeli, E.Welser, E. Oliva, A. W. Bett, and F. Dimroth, Current-matched triple-junction solar cell reaching 41.1% conversion efficiency under concentrated sunlight, Appl. Phys. Lett. **94**, 223504 (2009).

2) K. Sasaki, T. Agui, K. Nakaido, N. Takahashi, R. Onitsuka, and T. Takamoto, Development of InGaP/GaAs/InGaAs inverted triple junction concentrator solar cells, AIP Conf. Proc. **1556**, 22 (2013).

3) http://rredc.nrel.gov/solar/spectra/am1.5/

4) A. V. Tikhonravov, M. K. Trubetskov, and G. W. DeBell, Application of the needle optimization technique to the design of optical coatings, Appl. Opt. **35**, 5493 (1996).

5) A. V. Tikhonravov, M. K. Trubetskov, and G. W. DeBell, Optical coating design approaches based on the needle optimization technique, Appl. Opt. **46**, 704 (2007).

6) A. N. Tikhonov Jr., A. V. Tikhonravov, and M. K. Trubetskov, Second order optimization methods in the synthesis of multilayer coatings, J. Comput. Math. Math. Phys. **33**, 1339 (1993).

7) I. Anton, M. Martinez, F. Rubio, R. Nunez, R. Herrero, C. Dominguez, M. Victoria, S. Askins, and G. Sala, Power rating of CPV systems based on spectrally corrected DNI, AIP Conference Proceedings (8th International Conference on Concentrating Photovoltaic Systems), **1477**, 331-335 (2012).

Chapter 3

Temperature reduction of solar cells in a concentrator photovoltaic system using a long wavelength cut filter

3.1. The concept of the system

In this chapter, we propose an improved thermal and new electrical model with a full CPV system performance and lifetime estimation using unreliability calculations for the CPV model with InGaP/GaAs/InGaAs solar cell presented in chapter 2. High-efficiency multijunction solar cells under conditions of high light concentration have been investigated thoroughly for terrestrial applications in the last two decades [1-15]. CPV modules consisting of a Fresnel optical concentrator lens was also investigated thoroughly in different other works [16]. In general CPV modules uses III–V multijunction solar cell, which is expensive but highly efficient, typically have an efficiency above 40% [17-25]. Optical losses and spectral mismatch caused by optical elements in the CPV system significantly degrade the performance of a CPV system [26]. In this chapter the technique used to improve the performance of the solar cell under high concentration was cutting the wave range of solar spectrum that is responsible for heating the solar cell and allowing only the spectrum range that is converted into electricity to reach the multijunction solar cell. The multijunction solar cells are influenced by their operating temperature, and decreasing this temperature can have a significant impact on the open-circuit voltage, maximum power point, and efficiency of the solar cells [27]. The technique used to cut the undesired spectrum was to implement a thin-film filter on the surface of the secondary optical element in the system to cut the undesired spectrum. The solar cell used was an InGaP/GaAs/InGaAs multijunction solar cell [28]. Further analysis of the multijunction characteristics compared to the previous chapter showed that the highest spectral response was in the range of 400–1300 nm compared to the considered range of 400–1100 nm in chapter 2. A new thin-film was designed so that it has high transmission in this range while reflecting the rest of the solar spectrum. Another reason for perusing a new thin film design was the relatively low optical efficiency achieved in chapter 2 for the model with 1100 nm cutoff thin film filter. The new thin-film filter was designed to meet the desired characteristics using commercial thin-film design software. Improved thermal and new electrical performance study of the system was conducted to estimate the effect of the thin-film filter on the solar cell temperature and electrical characteristics. The possible effect on the lifetime of the solar cell was also estimated by making a reliability estimation under different temperature stress levels.

3.2. The system design

3.2.1. The optical design

The optical system in this study consists of two main parts, the POE (primary optical element) [29] which in this study was a Fresnel lens and the SOE (secondary optical element) which was a homogenizer (refractive truncated inverted pyramid) [4].

The Fresnel lens is an optical component which can be used as alternative to conventional continuous surface optics because of its low cost and light weight characteristics. The bulk of material between the refracting surfaces in the normal optical lens has no effect (other than increasing absorption losses) on the optical properties of the lens, that is why the bulk of material in Fresnel lens has been reduced by the extraction of a set of coaxial annular cylinders of material. One of the most important characteristics of the Fresnel lens is the focal length, which was 420 mm. The distance between the multijunction solar cell and the Fresnel lens was set to 460 mm. A schematic diagram of the optical system is shown in Fig. 3-1.

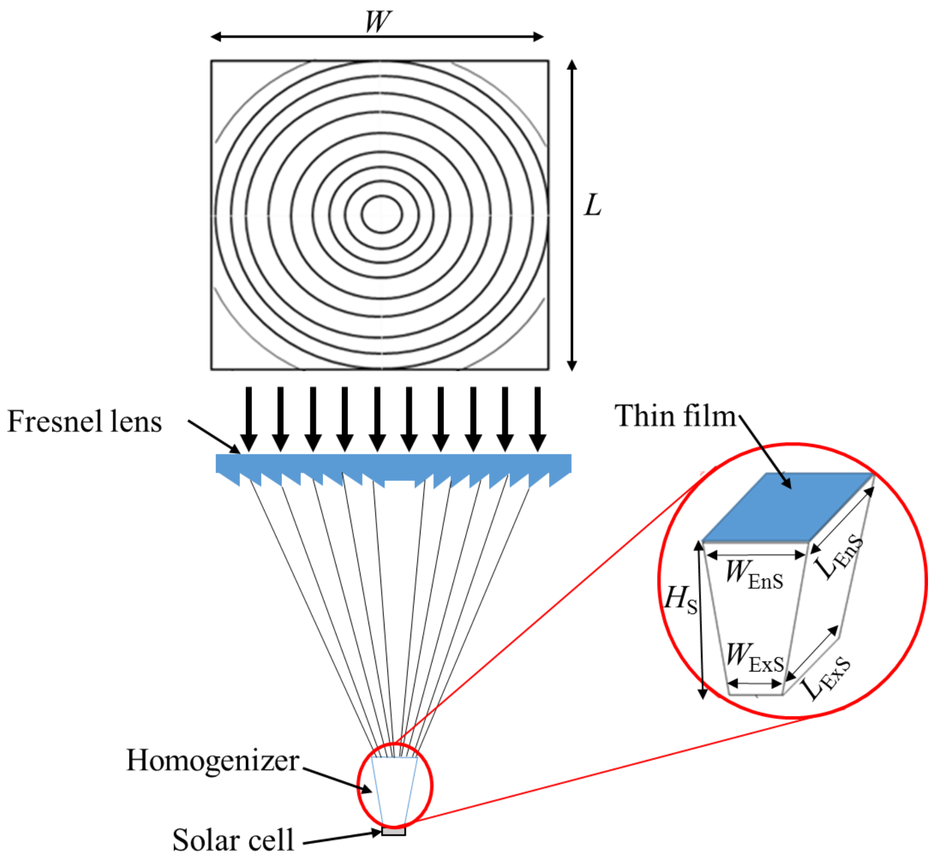

Fig. 3- 1: Schematic of the optical system.

The dimensions of the optical system parts are shown in Table 3-1. The geometrical concentration ratio of the system was C_g = 1322 times. The material of the Fresnel lens was set to be SOG (silicon on glass) because of the high optical performance of SOG Fresnel lenses. In order to simulate the performance of the system a Monte-Carlo ray tracing was conducted in ZEMAX software in the wavelength range of 300–2500 nm using the solar spectrum AM 1.5D (total power: 900 W/m^2) ASTM G173-03 [30].

We chose to perform the simulation in the wave range of 300–2500 nm although the used multijunction solar cell works in the wavelength range 400–1300 nm to study the effect of extra heating in the solar cell by the spectrum part, that is not converted into electricity, and it is rather converted into heat. This will show the direct effect of using the thin-film on the performance of the system.

Table 3- 1: The basic dimensions of the optical system.

The system parts	**Dimensions (mm)**	
Primary optical element	L	200
	W	200
Secondary optical element	L_{EnS}	14
	W_{EnS}	14
	L_{ExS}	5.5
	W_{ExS}	5.5
	H_S	40
PV cell	L_{PV}	5.5
	W_{PV}	5.5
	H	0.2

3.2.2. The thin-film design

In this section, we discuss the designing procedure for the long wavelength cut thin-film filter. To be able to design the thin-film we first have to understand the used multijunction solar cell spectrum response and EQE under concentration conditions.

The used multijunction solar cell was InGaP/GaAs/InGaAs. The External quantum efficiency (EQE) indicates the ratio of the number of charge carriers collected by the solar cell to the number incident photons of a particular wavelength. The EQE of the used multijunction solar cell is shown in Fig. 3-2.

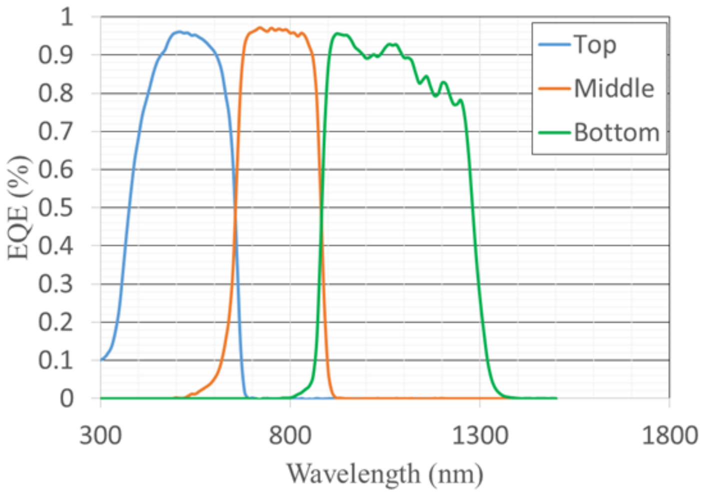

Fig. 3- 2: The EQE of InGaP/GaAs/InGaAs multijunction solar cell.

EQE chart indicates clearly that the highest response of the used solar cell is in the wavelength range of 400–1300 nm which means that the solar cell utilizes the solar spectrum into electrical energy in this wavelength range, while the rest of the solar spectrum outside this range is probably lost as heat in the solar cell. The main idea of using thin-film filter is to prevent the solar spectrum, which is lost as heat or dissipated in other parts of the solar cell, from reaching the solar cell while allowing only the utilized spectrum to hit the solar cell surface. The thin-film, which we designed in this section, can do exactly that by transmitting the solar spectrum in the range 400–1300 nm, while reflecting the rest of the spectrum.

Using the needle optimization technique described in section 2.2.2 of the second chapter [31- 33] and commercial thin-film design software TFCalc (Software Spectra), we were able to design the desired thin-film filter.

The two materials used in the filter are TiO_2 (for a high refractive index) and SiO_2 (for a low refractive index) which has negligible absorption in the spectral range of interest. These two materials are commonly used for coating and can manage high thermal loads; the optical constants for the two materials are shown in Table 3-2 and Table 3-3 respectively. The transmittance of the thin-film is shown in Fig. 3-3. The resulted thin-film had 97 layers, which are shown in Table 3-4. The substrate was BK7. The resulted thin film thickness was 4451.46 nm. Appendix C shows the transmittance profile of the thin-film filter.

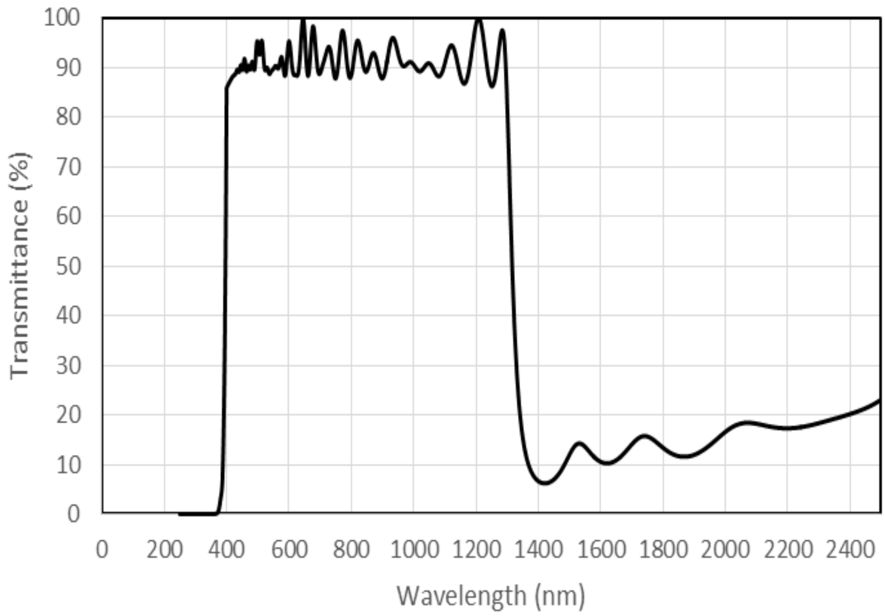

Fig. 3- 3: Thin-film transmittance curve as a function of wavelength.

Table 3- 2: Optical constants for TiO_2 film at different wavelength (nm).

Wave	**400**	**430**	**450**	**500**	**550**	**600**	**700**	**800**	**900**
n	2.397	2.313	2.273	2.210	2.177	2.160	2.147	2.146	2.148
k	0.002	0.002	0.002	0.002	0.002	0.002	0.002	0.002	0.002

Table 3-3: Optical constants for SiO_2 film at different wavelength (nm).

Wave	**350**	**400**	**450**	**500**	**550**	**600**	**650**	**700**	**900**	**1562**
n	1.472	1.467	1.463	1.459	1.455	1.452	1.450	1.446	1.434	1.429
k	0	0	0	0	0	0	0	0	0	0

Table 3- 4: Thin-film structure.

No.	Material	Thickness (nm)	No.	Material	Thickness (nm)	No.	Material	Thickness (nm)
0	Substrate		34	TiO_2	7	68	TiO_2	13
1	SiO_2	188	35	SiO_2	16	69	SiO_2	23
2	TiO_2	1	36	TiO_2	3	70	TiO_2	8
3	SiO_2	351	37	SiO_2	17	71	SiO_2	207
4	TiO_2	7	38	TiO_2	6	72	TiO_2	12
5	SiO_2	33	39	SiO_2	8	73	SiO_2	27
6	TiO_2	11	40	TiO_2	15	74	TiO_2	107
7	SiO_2	18	41	SiO_2	6	75	SiO_2	15
8	TiO_2	24	42	TiO_2	183	76	TiO_2	14
9	SiO_2	11	43	SiO_2	9	77	SiO_2	28
10	TiO_2	126	44	TiO_2	21	78	TiO_2	8
11	SiO_2	9	45	SiO_2	17	79	SiO_2	217
12	TiO_2	22	46	TiO_2	12	80	TiO_2	8
13	SiO_2	12	47	SiO_2	23	81	SiO_2	22
14	TiO_2	12	48	TiO_2	9	82	TiO_2	6
15	SiO_2	18	49	SiO_2	44	83	SiO_2	14
16	TiO_2	8	50	TiO_2	4	84	TiO_2	16
17	SiO_2	27	51	SiO_2	267	85	SiO_2	8
18	TiO_2	6	52	TiO_2	7	86	TiO_2	115
19	SiO_2	358	53	SiO_2	27	87	SiO_2	14
20	TiO_2	5	54	TiO_2	16	88	TiO_2	17
21	SiO_2	29	55	SiO_2	12	89	SiO_2	25
22	TiO_2	6	56	TiO_2	130	90	TiO_2	7
23	SiO_2	19	57	SiO_2	14	91	SiO_2	212
24	TiO_2	10	58	TiO_2	11	92	TiO_2	8
25	SiO_2	12	59	SiO_2	20	93	SiO_2	18
26	TiO_2	23	60	TiO_2	9	94	TiO_2	5
27	SiO_2	7	61	SiO_2	220	95	SiO_2	52
28	TiO_2	130	62	TiO_2	10	96	TiO_2	11
29	SiO_2	12	63	SiO_2	18	97	SiO_2	116
30	TiO_2	23	64	TiO_2	9			
31	SiO_2	37	65	SiO_2	15			
32	TiO_2	11	66	TiO_2	117			
33	SiO_2	218	67	SiO_2	13			

3.2.3. The thermal model design

A new improved heat transfer model compared to the thermal model introduced in section 2.2.3 was built in COMSOL Multiphysics. If a photon has less energy than the bandgap, it is not collected. This is a major drawback for solar cells, which are not sensitive to most of the infrared spectrum, although infrared spectrum represents almost half of the power coming from the sun. Conversely, photons with energy higher than the bandgap, for example, those in blue light, initially eject an electron to a state high above the bandgap, but this extra energy is lost as heat [34]. The IR radiation, which is transmitted through the transparent section of the solar cell, tends to be absorbed in the silver at the rear surface of the solar cell and eventually increases the temperature of the cell.

We introduced the following modifications to the model in section 2.2.3 based on the information above by adjusting Eq. (2.4). We separated the solar spectrum into three parts: one was the spectrum in the range 400–1300 nm, which is used by the solar cell we are using to generate electricity, the second was the ultraviolet spectrum range, and the third was the rest of the spectrum above 1300 nm. By integrating the direct solar spectrum (AM1.5D, total power = 900 W/m^2, ASTM G173-03) in each wavelength range we obtained the fraction of the DNI that is used in each range of the spectrum, and as a result new three equations for heat loss was obtained.

The DNI that we used was equal to 751 W in the spectrum range of 400 to 1300 nm, which represents a fraction of the total 900 W direct radiation equal to 0.834, and the heat power equation becomes

$$P_{cell} = 0.834 \cdot DNI \cdot A_{\text{cell}} \cdot C \cdot \eta_{\text{op}} \cdot (1 - \eta), \quad (3.1)$$

We should imply that the optical efficiency and solar cell electrical efficiency was calculated for this part of the spectrum.

The amount of the DNI that we used in the range 0–400 nm (the ultraviolet spectrum) was equal to 30 W, which represents a fraction of the total 900 W direct radiation equal to 0.0335, and the heat power equation becomes

$$P_{UV} = 0.0335 \cdot DNI \cdot A_{\text{cell}} \cdot C \cdot \eta_{\text{op}} \ . \quad (3.2)$$

The total amount of DNI that we used in the spectrum range above 1300 nm was equal to 118 W, which is converted into heat in the silver at the rear surface of the solar cell. This represented a fraction of the total 900 W direct radiation equal to 0.131, and the equation becomes

$$P_{IR} = 0.131 \cdot DNI \cdot A_{\text{cell}} \cdot C \cdot \eta_{\text{op}} \ . \quad (3.3)$$

We added three heat sources to the COMSOL model, we added the first source for the ultraviolet spectrum and the second source for the efficient spectrum on the surface of the solar cell, while we added the third source for the IR spectrum on the rear surface of the solar cell. The heat power was calculated using the average η_{op} for each wavelength range. The used electrical efficiency in Eq. (3.1) for the spectrum range of 400–1300 nm with a power of 751 W (total power in all ranges: 900 W) was 49%. This efficiency was driven from the total conversion efficiency of the solar cell for all the spectrum range which was equal to 41%.

The detailed structure around the multijunction solar cell is illustrated in Fig. 3-4.The receiver consisted of homogenizer, III-V solar cell, a solder, a copper electrode, insulation materials and aluminum stage which was mounted on the aluminum chassis.

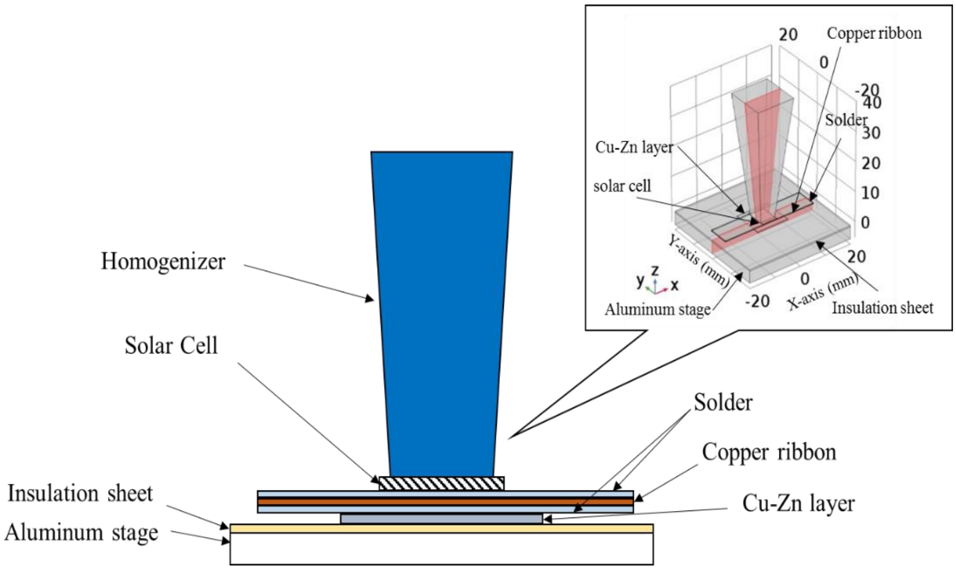

Fig. 3- 4: Detailed structure around the multijunction solar cell.

3.2.4. The electrical model design

In order to analyze the electrical performance of the system we first need to obtain photocurrent distribution for each sub-cell, making it possible to determine the total photocurrent value and current matching ratio. An artificial spectrum $S_{\mathrm{AM\ 1.5D}}$ (λ) was used for the emitting source in ZEMAX simulation to predict the photocurrent distribution. The integration of this artificial spectrum for each wavelength range and for the specific EQE at that range weights the wavelength potential to generate an electron-hole pair in the solar cell. We obtained this artificial spectrum by taking the multijunction solar cell EQE into account using the following equation:

$$S_{AM\ 1.5D}(\lambda) = E_{AM\ 1.5D}(\lambda) \cdot \frac{q\lambda}{hc} \cdot EQE(\lambda), \quad (3.4)$$

where $S_{\mathrm{AM\ 1.5D}}$ (λ) is the artificial spectrum for the photocurrent where the unit for the integration of this spectrum is typically expressed in mA/cm^2; $E_{\mathrm{AM\ 1.5D}}$ (λ) (W/m^2/nm) is the standard direct solar spectrum distribution AM 1.5D; λ is the wavelength (nm); q

represents the charge of a single electron; h is Planck's constant; and c is the speed of light in vacuum. The artificial spectrum for the photocurrent was divided into several parts corresponding to every subcell. As a result, the simulation output represented the photocurrent distribution for each sub-cell.

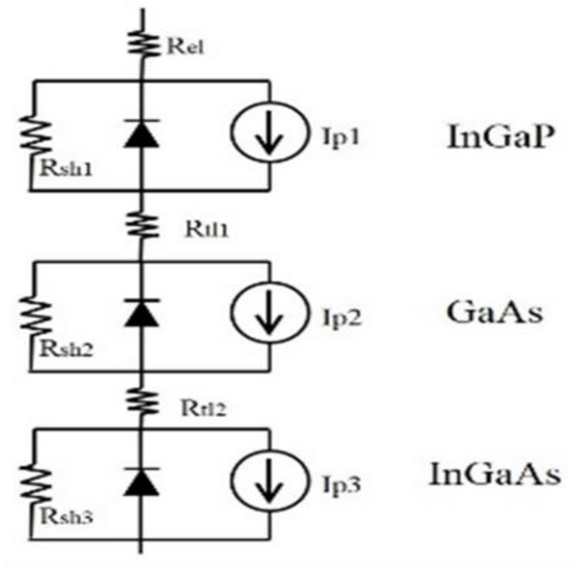

Fig. 3- 5: Equivalent circuit model for triple junction solar cell.

Equivalent circuit calculations were carried out using the SPICE (Cadence Design System) [35, 14]. The single unit equivalent circuit used is shown in Fig. 3-5. The parameters of the circuit are shown in Table 3-5.

Table 3-5: Parameters of single unit equivalent circuit model.

Symbol	Name	Value	Unit
R_{sh1}	Top sub-cell shunt resistance	3000k	Ω
R_{sh2}	Middle sub-cell shunt resistance	1500k	Ω
R_{sh3}	Bottom sub-cell shunt resistance	115	Ω
R_{tl1}	Tunnel junction resistance	0.0012	Ω
R_{tl2}	Tunnel junction resistance	0.0008	Ω
R_{el}	Circuit series resistance	0.0236	Ω

3.2.5. Average Arrhenius–Weibull model for the lifetime estimation of solar cell

Reducing the temperature of the solar cell can lead to a longer lifetime. Espinet-González and coworkers reported that the unreliability of the multijunction solar cell could be calculated using an Arrhenius–Weibull model. By calculating unreliability, we can estimate the lifetime of the solar cell under different stress levels [36-38]. The activation energy E_A, which is the main parameter needed for this model, was calculated by fitting the Arrhenius–Weibull model to the failure distribution across the different tested temperatures. The unreliability F(t) as a function of time is described by

$$F(t) = \int_0^t f(\mathrm{t})dt \qquad (3.5)$$

The Arrhenius life-stress model is derived from the Arrhenius reaction rate equation proposed by Svante Arrhenius [37] as

$$L(T) = C \cdot \exp(\frac{E_A}{kT}), \qquad (3.6)$$

where $L(T)$ is a temporal measurable characteristic of the device under the life test, which depends on the temperature T, k is the Boltzmann constant, and E_A is the activation energy of the mechanism that causes the failure. C is a parameter of the Arrhenius model, which depends on the $L(T)$ used.

The activation energy (E_A) of the failure mechanism, which determines the acceleration factor (A_F) of the test, is obtained from the linearized expression of the Arrhenius life-stress model, as

$$\ln[L(T)] = E_A \cdot \left({}^{1}/_{kT}\right) + \ln[C]. \qquad (3.7)$$

The activation energy is obtained from the slope of the curve ln[$L(T)$] versus $1/kT$. Obviously at least three different values of $L(T)$ obtained from three experiments at three different temperatures are necessary in order to fit the curve ln[$L(T)$] versus $1/kT$ properly. The value of E_A that we used in this study was calculated by Espinet-González et al. and was equal to 1.58 eV [36]. The activation energy is a measure for the response of lifetime to the stress (in our case, the temperature). The larger the value of the activation energy, the higher the dependence of the lifetime on the specific stress, in this case, the temperature. In other words, the higher the activation energy, the higher the effect of the temperature on the solar cell.

The acceleration factor (A_F) is defined as a unitless number that relates a product's lifetime at an accelerated stress level to the lifetime at the nominal stress level. Once the activation energy is calculated, we can obtain the acceleration factor between two temperatures (T_1 and T_2) directly from

$$A_F = \frac{L(T_1)}{L(T_2)} = \exp\left[\frac{E_A}{k}\cdot\left(\frac{1}{T_1} - \frac{1}{T_2}\right)\right] \ . \qquad (3.8)$$

It has to be pointed out that small changes in the value of the activation energy have a strong impact on the acceleration factor since it has an exponential dependence on E_A [37].

$f(\mathrm{t})$ is the Arrhenius–Weibull model for the lifetime distribution and the life stress model, which can be expressed by the following equation [36-37]:

$$f(t,T) = \frac{\beta}{c\cdot\exp(\frac{E_A}{kT})}\cdot\left(\frac{t}{c\cdot\exp\left(\frac{E_A}{kT}\right)}\right)^{\beta-1}\cdot\exp\left[-\left(\frac{t}{c\cdot\exp(\frac{E_A}{kT})}\right)^{\beta}\right] \ . \qquad (3.9)$$

Here, t is the time, T is the temperature, $f(t, T)$ is the probability density function, β is the shape parameter, C is a parameter of the Arrhenius model, E_A is the activation energy, and k is the Boltzmann constant.

The deterioration in the solar cell by the temperature increase was reported by Espinet-González et al., [39] which we used as a reference for our calculations of warranty time. The accelerated life test (ALT) failure analysis revealed a severe worsening of the silver electrodes, which resulted in making the busbar and fingers not equipotential. This would have led to the circulation of very high current densities into the semiconductor in very small areas of the cell structure during the ALT. The existence of these high current densities in small semiconductor regions would have favored the evolution of defects and cracks, turning the solar cells into shunts. This is a failure driven by thermal runaway. Thermal runaway failures caused by thermal fatigue have also been previously reported [39]. If the solar cells were not forward biased and just experienced a temperature stress, there would be no decrease in their performance even for temperatures as high as 164°C. A detailed analysis of both the front metal contacts and the semiconductor structure by scanning electron microscopy and energy-dispersive X-ray spectrometry did not show any kind of degradation either. On the other hand, the cells experiencing the combined temperature and current injection stress show a severe degradation, leading to a short-circuit-like failure. The current is identified as the cause of degradation while the temperature just dominates the accelerating factor of the ALT [40].

In this study we introduced an average Arrhenius–Weibull model taking into account the different temperatures and irradiation fluctuation throughout the year in Miyazaki City, while Espinet-González et al.'s [36-38] study was conducted at single stress levels. The average model was modified from the Arrhenius–Weibull model using the following equation:

$$g(\mathrm{t}) = \frac{\sum_{i=1}^{m} f(t,T_i)}{m} \tag{3.10}$$

Here, *m* is the number of calculated cell temperatures throughout one year estimated from 8760 calculated temperature points. The new unreliability function is described by an equation that uses the average Arrhenius–Weibull model:

$$G(\mathrm{t}) = \int_0^t g(t)dt \ . \tag{3.11}$$

To obtain the average Arrhenius–Weibull model, we used the calculated temperatures based on the DNI data for Miyazaki City. We obtained the DNI from the Meteorological Test Data for Photovoltaic Systems (METPV) database, which is a weather database developed by Japan Meteorological Agency based on a request from the New Energy and Industrial Technology Development Organization (NEDO) [41]. This data was used to calculate temperature values throughout one year for a range of registered DNI data.

3.3. Results and discussion

3.3.1. Optical simulation

Using ray-tracing simulation, we analyzed the optical performance of the CPV model with the thin-film filter and compared it with the model without the thin-film filter. The peak irradiance value without thin-film was 1.076×10^6 W/m^2 and the peak to average irradiance ratio PAR was equal to 1.071. After using the designed thin-film in the optical model the resulted peak irradiance value decreased to 9.635×10^5, and the peak to average irradiance value became 1.091, which indicates less uniform distribution on the surface of the solar cell. The irradiance distribution on the surface of the solar cell is shown in Fig. 3-6. Despite the small increase in PAR value both of the irradiance distributions with thin-film and without thin-film can be considered as a good uniform distribution compared to the ideal case of PAR = 1. The total optical efficiency of the model was 84.4% without the thin-film filter and 74.2% with the thin-film filter.

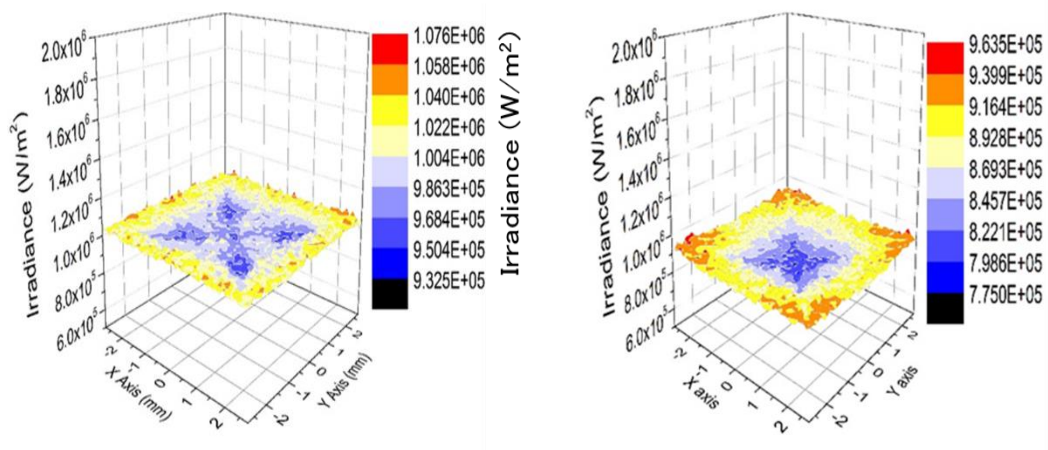

(a) Irradiance without thin-film filter.

(b) Irradiance with thin-film filter.

Fig. 3- 6: Irradiance distribution on the solar cell.

The main reason for the drop in the optical efficiency when using the thin-film filter is the filter's cut of the long-wavelength region. We must stress that this drop in the optical efficiency in the case with the thin-film filter had little influence on the output of the CPV module, as we will explain later, because the multijunction solar cell converts radiation of wavelengths greater than 1300 nm into heat rather than electricity. Average optical efficiency in Eq. (3.1, 3.2, 3.3) was calculated for each wavelength range. Table 3-6 shows the resulted optical efficiencies.

Table 3- 6: Optical efficiency for different spectrum ranges with and without thin-film.

Optical efficiency (%)	**400 to 1300 nm**	**Less than 400 nm**	**Above 1300 nm**
Without thin-film	87.47	67.43	67.39
With thin-film	83.47	11.5	9.32

3.3.2. Thermal simulation

Thermal simulation using the new improved thermal model, which takes into account the three ranges of spectrum (the spectrum from 400 to 1300 nm, the ultraviolet spectrum range, and the rest of the spectrum above 1300 nm), showed that the temperature of the multijunction solar cell without thin-film filter reached to a maximum of 121°C, which mean 2.3°C increase in the resulted temperature from the thermal model in chapter 2.

The temperature distribution on the solar cell surface is shown in Fig. 3-7(a), while the change in temperature across the x-axis (y = 0) was about 6°C between 115°C and 121°C and its shown Fig. 3-7(b).

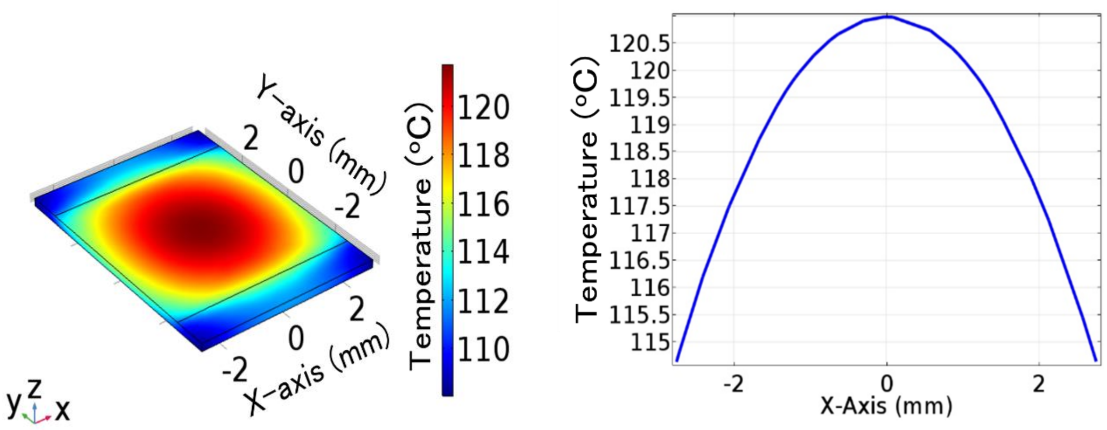

(a) Solar cell Temperature distribution.

(b) Temperature change across the X- Axis of the Solar cell.

Fig. 3- 7: Thermal simulation results for the case without cutoff thin-film filter.

The use of thin-film with this thermal model had led to a big decrease in the temperature of the solar cell. The solar cell temperature was decreased to 95.7°C (with the thin-film filter), representing a total decrease of 25.3°C. Owing to the effect of the thin-film filter, which removes long-wavelengths, the cell temperature was markedly reduced. The temperature change across the solar cell surface was also decreased to only 4.7°C, which means better temperature uniformity across the solar cell surface and as a result better performance. The results for heat transfer simulation with thin-film filter are shown in Fig. 3-8. The temperature distribution on the surface of the solar cell is shown in Fig. 3-8(a), while Fig. 3-8(b) shows the temperature change across the *x*-axis ($y = 0$) of the solar cell.

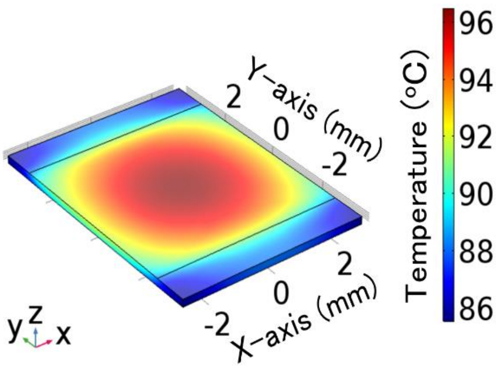

(a)

Solar cell Temperature distribution.

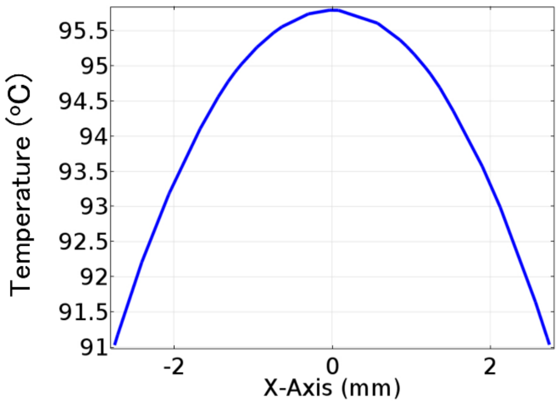

(b)

Temperature change across the X- Axis of the Solar cell.

Fig. 3- 8: Thermal simulation results for the case with cutoff thin film filter.

The highest registered DNI in Miyazaki City was 1035 W/m^2, where the temperature of the solar cell reached 135°C without the thin-film filter and 106°C with the thin-film filter. The calculated cell temperatures throughout the year were estimated at 8760 points, an average of 24 points every day. The resulting cell temperature count is illustrated by the histograms in Fig. 3-9. The figure shows that the highest count in the case without the thin-film filter was for temperatures in the range of 110°C to 115°C, while for the cell with the thin-film, the highest count was for temperatures in the range of 85°C to 90°C. These results demonstrated a sizeable decrease in the operation temperature range. We should stress that this histogram does not show the results for the case of DNI equal to 0 because this data is for the highest repeated temperatures due to night-time hours.

(a) Temperature range counts without thin film

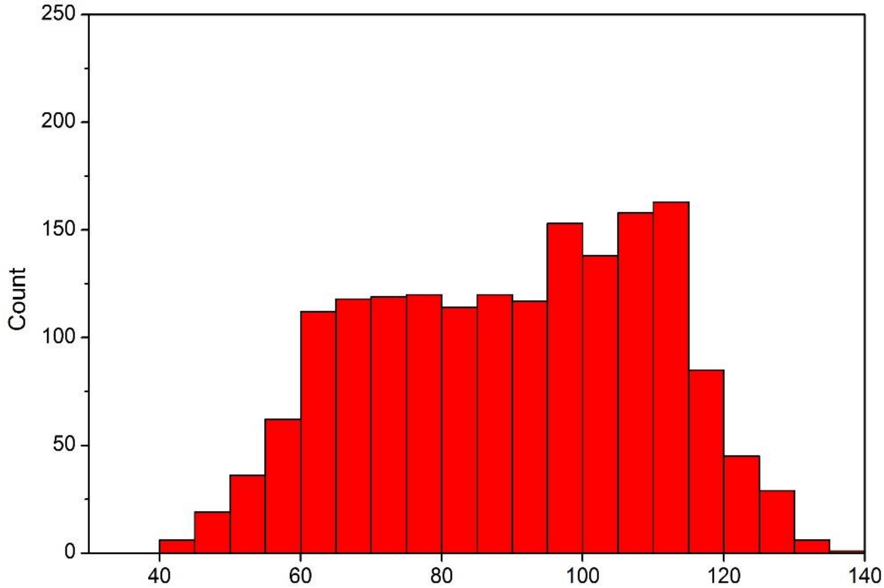

Temperature (^oC)

(b) Temperature range counts with thin film

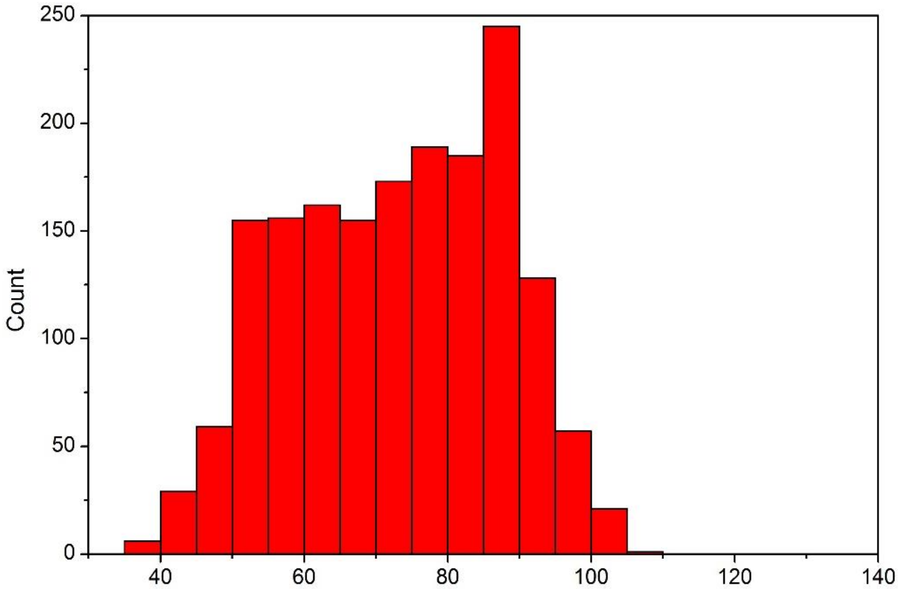

Temperature (^oC)

Fig. 3- 9: Temperature counts over the course of a year in cases (a) without and (b) with thin-film.

3.3.3. Electrical simulation

The in-plane distributions of the photocurrent were obtained from the spectral response of the InGaP/GaAs/InGaAs multijunction solar cell as explained earlier in this chapter in section 3.2.4. The resulting distributions of the photocurrent generated from each sub-cell (top, middle, and bottom subcells) are shown in Fig. 3-10. Figure 3-10(a) represents the results for model without the thin-film filter, while Fig. 3-10(b) represents the photocurrent distribution for the model with the thin-film filter set on the surface of the homogenizer. The results showed that there was good uniformity in both cases due to the use of the secondary optical element (the homogenizer). The photocurrents from each sub-cell in the cases with and without the thin-film filter are shown in Table 3-7.

Table 3- 7: Photocurrents from each sub-cell with and without thin-film filter.

Symbol	Name	Value	Unit
I_{p1}(with TF)	Top sub-cell photocurrent	4.7	A
I_{p2}(with TF)	Middle sub-cell photocurrent	4.75	A
I_{p3}(with TF)	Bottom sub-cell photocurrent	5	A
I_{p1}(without TF)	Top sub-cell photocurrent	4.82	A
I_{p2}(without TF)	Middle sub-cell photocurrent	4.824	A
I_{p3}(without TF)	Bottom sub-cell photocurrent	5.249	A

We analyzed the operating characteristics of the CPV module by combining the ray-tracing, equivalent circuit, and thermal simulations. Figure 3-11 shows the calculated Current–Voltage (*I*–*V*) characteristics of CPV modules with and without the thin-film filter. These results were simulated using SPICE for the two different calculated maximum temperatures, 121°C in the case without the thin-film filter and 95.7°C with the thin-film filter, we also used the resulting photocurrent values shown in Table 3-7 in SPICE model.

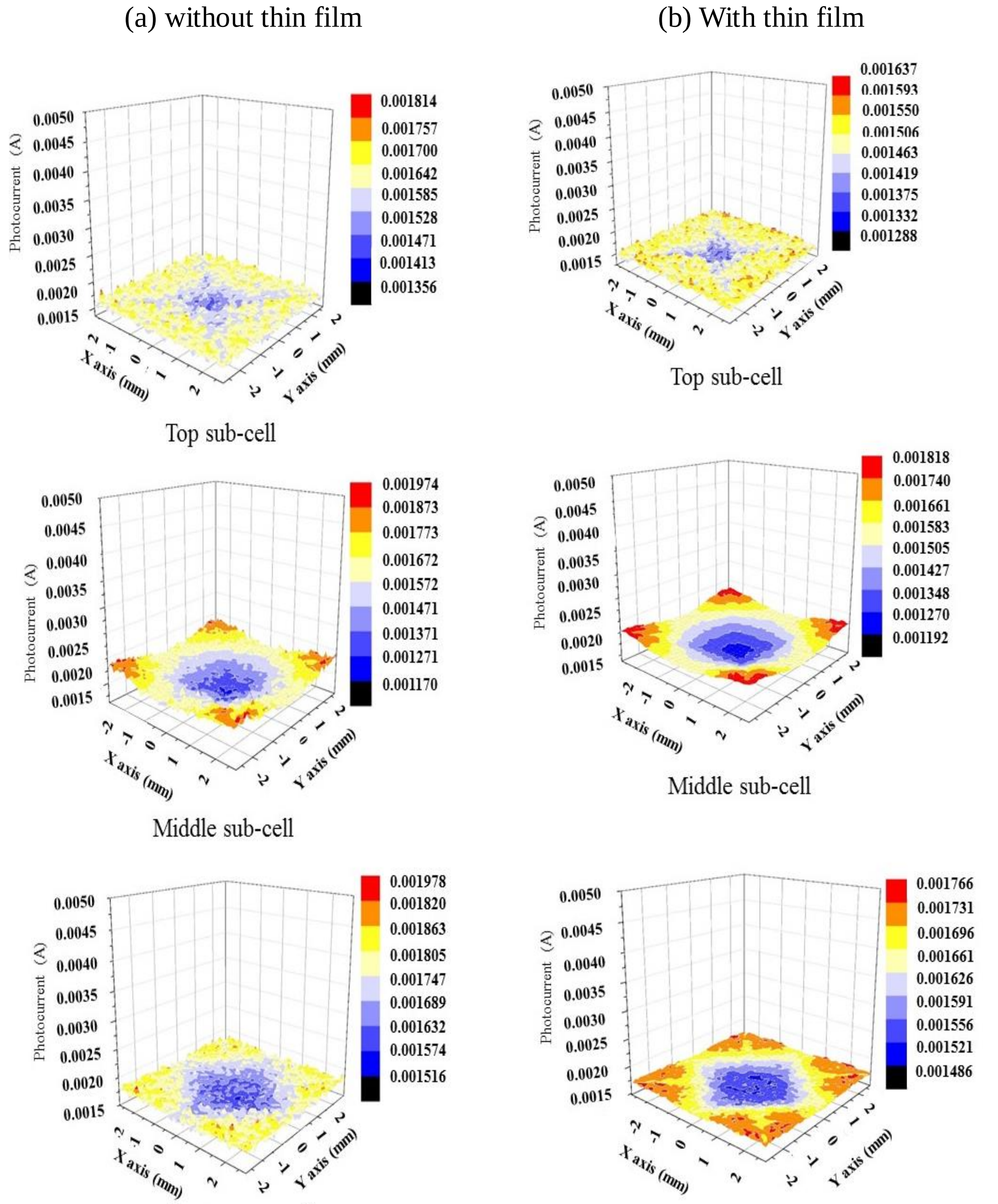

Fig. 3- 10: Resulting distribution of photocurrent generated from each subcell (top, middle, and bottom sub-cells), (a) Distribution of photocurrent without thin-film. (b) Distribution with thin-film deposited on homogenizer surface.

The results showed that the open-circuit voltage (V_{oc}) increased due to the decrease in the cell temperature because there is an inverse relationship between temperature and V_{oc}, while the current dropped a small amount due to the presence of the thin-film filter, which cuts a large range of the solar spectrum. The small drop in the short-circuit current (I_{sc}) can be justified by the sizeable drop in temperature. Table 3-8 shows the calculated output characteristics of CPV modules with and without the thin-film filter. Eventually, we could obtain almost the same maximum power (P_m) and the module efficiency increased for the optical model with a thin-film filter and a lower solar cell working temperature was achieved.

Table 3- 8: Calculated output characteristics of the CPV modules.

	I_{sc} (A)	V_{oc} (V)	P_m (W)	*FF*	Module efficiency (%)
Without thin-film	4.82	3.66	14.05	0.796	39.02
With thin-film	4.70	3.73	14.19	0.809	39.4

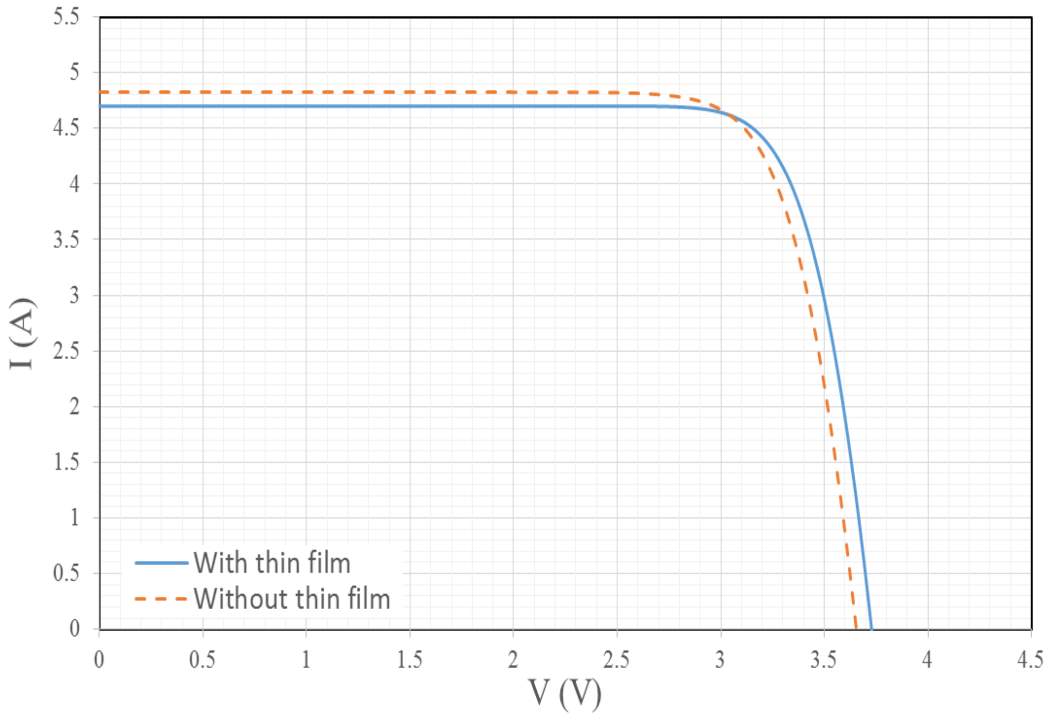

Fig. 3- 11: Calculated *I–V* characteristics of CPV modules with and without thin-film filter.

3.3.4. Lifetime simulation

We calculated the unreliability as a function of time using Eqs. (3.10) and (3.11). This calculation were done for the case with and without the thin-film for all temperature stress levels by using Mathcad software. Figure 3-12 shows the average unreliability as a function of time for a module with and without the thin-film. The solar cell will malfunction when the unreliability value of the solar cell reaches 100%. In general, the warranty time is defined for a failure population of 5%. The warranty time for a cell without a thin-film was 1×10^4 h using the average unreliability function, while for a multijunction solar cell with the thin-film the warranty time for a failure population of 5% was increased to 2×10^5 h, as shown in Fig. 3-12. We assumed that the operation time for the multijunction solar cell was 8 h per day based on previous work on evaluating the reliability of concentrator multijunction solar cells [37]. For a failure population of 5% and working time of 8 h per day in the used CPV the increase in lifetime of 1.9×10^5 h means that the lifetime of the multijunction solar cell increased from about 3.4 years to almost 68.5 years. This is a similar result to the reference mentioned previously [37]. In Ref. 37, the obtained warranty time for a failure population of 5% and working temperature of 80ºC was equal to 69 years, while the warranty time for a working temperature of 119ºC was less than 1000 h.

For a failure population of 5% by using a thin-film results showed that for our concentrator PV system, the lifetime was increased by more than 65 years filter. We consider this a proof of the effectiveness of the thin-film filter and the huge benefits of using it.

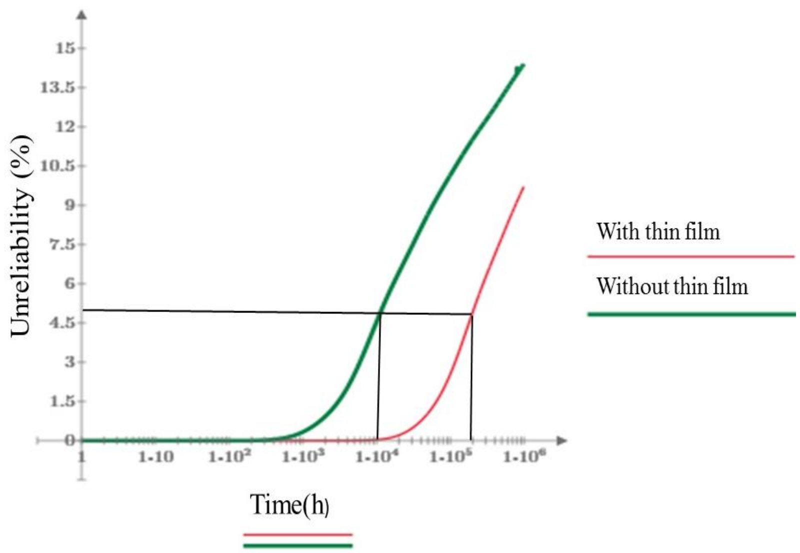

Fig. 3- 12: Average unreliability as a function of time for a module with and without thin-film.

3.4. Conclusion

A 1322 sun CPV system with a InGaP/GaAs/InGaAs multijunction solar cell was designed and optical, electrical, and thermal simulations were conducted. A thin-film filter was set on the homogenizer entry surface in order to cut the solar spectrum outside the wavelength range of 400–1300 nm, and we evaluated the system operation without and with thin-film filter.

Results showed that the model with the thin-film filter had a significant decrease in the solar cell temperature larger than the temperature decrease achieved in the chapter 2 and better optical performance with higher optical efficiency. The main advantage of using the thin-film filter was to decrease the operation temperature of the system without decreasing the electrical performance of the system despite the huge cut in the spectrum, and in the same time, we achieved a significant increase in lifetime. The thin-film filter will not add any weight or load to the tracker system, it is expected to reduce the weight of the needed heat sinks, and as result, less power will be needed for the tracking system. Because of the small area of the thin-film filter and based on the assumption that a heat sink will cost around 5% of the total cost of the CPV unit, we concluded that implementing thin-film filter technique for the reduction of cell temperature and increasing the lifetime of the system will be efficient form economical point of view.

The total optical efficiency of the optical model without the thin-film filter was 84.4%; correspond with 74.2% with the thin-film filter. This revealed and increase of 6.48% in the optical efficiency compared to the results achieved in chapter 2. Irradiance distribution showed good uniformity before and after using the thin-film filter with very small degrade in the uniformity after using the thin-film filter, which indicates that the use of thin-film filter has almost no effect on the resulted irradiance distribution profile.

The thermal simulation results showed that the cell temperature dropped from a maximum of 121°C (without the thin-film filter) to 95.7°C (with the thin-film filter), representing a total decrease of 25.3°C. We expected that this decrease in the solar cell temperature had a big impact on the lifetime and the reliability of the system. The temperature decrease in this chapter was larger than that achieved in chapter 2 because we used an improved thermal model and a new thin-film filter design which resulted in more accurate results.

The temperature profile for a full year was also evaluated, and results showed that the temperatures in the range of 110°C to 115°C had the highest count which means that the solar cell work mostly in this range for the case without thin-film filter. For the module with the thin-film, the highest count of temperatures was in the range of 85°C to 90°C, which reveals that the solar cell works most of the time in temperatures less than the calculated temperature of 95.7°C for the CPV with thin-film under standard conditions in section 3.3.2.

By combining the ray-tracing, equivalent circuit, and thermal simulations, the electrical characteristics of the CPV module were analyzed in full. We obtained almost the same maximum power (P_m) and the model electrical efficiency increased in the model with the thin-film filter. The reliability and lifetime analysis of the solar cell showed that we were able to drastically increase the lifetime of the solar cell by the achieved temperature reduction. Results showed an increase of 1.9×10^5 h in the lifetime of the multijunction solar cell, or by more than 65 years for a failure population of 5% through the use of a thin-film filter. This leads us to conclude that the use of long-wavelength cut filter would increase the lifetime of a solar cell drastically without affecting its electrical performance despite the huge cut in the solar spectrum.

References

1) S. P. Philipps and A. W. Bett, III-V Multi-junction solar cells and concentrating photovoltaic (CPV) systems, Adv. Opt. Technol. **3**, 469 (2014).

2) K. Nishioka, T. Takamoto, T. Agui, M. Kaneiwa, Y. Uraoka, and T. Fuyuki, Evaluation of InGaP/InGaAs/Ge Triple-Junction Solar Cell under Concentrated Light by Simulation Program with Integrated Circuit Emphasis, Jpn. J. Appl. Phys. **43**, 882 (2004).

3) K. Nishioka, T. Takamoto, T. Agui, M. Kaneiwa, Y. Uraoka, and T. Fuyuki, Evaluation of temperature characteristics of high-efficiency InGaP/InGaAs/Ge triple-junction solar cells under concentration, Sol. Energy Mater. Sol. Cells **85**, 429 (2005).

4) K. Araki, M. Kondo, H. Uozumi, N. J. Ekins-Daukes, T. Egami, M. Hiramatsu, Y. Miyazaki, and M. Yamaguchi, Packaging III–V tandem solar cells for practical terrestrial applications achievable to 27% of module efficiency by conventional machine assemble technology, Sol. Energy Mater. Sol. Cells **90**, 3320 (2006).

5) K. Nishioka, T. Takamoto, T. Agui, M. Kaneiwa, Y. Uraoka, and T. Fuyuki, Evaluation of InGaP/InGaAs/Ge triple-junction solar cell and optimization of solar cell's structure focusing on series resistance for high-efficiency concentrator photovoltaic systems, Sol. Energy Mater. Sol. Cells **90**, 1308 (2006).

6) K. Nishioka, T. Takamoto, T. Agui, M. Kaneiwa, Y. Uraoka, and T. Fuyuki, Annual output estimation of concentrator photovoltaic systems using high-efficiency

InGaP/InGaAs/Ge triple-junction solar cells based on experimental solar cell's characteristics and field-test meteorological data ,Sol. Energy Mater. Sol. Cells **90**, 57 (2006).

7) K. Araki, T. Yano, and Y. Kuroda, 30 kW Concentrator Photovoltaic System Using Dome-shaped Fresnel Lenses, Opt. Express **18**, A53 (2010).

8) K. Nishioka, T. Sueto, M. Uchida, and Y. Ota, Detailed Analysis of Temperature Characteristics of an InGaP/InGaAs/Ge Triple-Junction Solar Cell, J. Electron. Mater. **39**, 704 (2010).

9) J. Jaus, A. W. Bett, H. Reinecke, and E. R. Weber, Reflective secondary optical elements for Fresnel lens based concentrator modules, Prog. Photovoltaics 19, (2011).

10) Y. Sakurada, Y. Ota, and K. Nishioka, Simulation of Temperature Characteristics of InGaP/InGaAs/Ge Triple-Junction Solar Cell under Concentrated Light, Jpn. J. Appl. Phys. **50**, 04DP13 (2011).

11) N. Shibata, Y. Ota, Y. Sakurada, Y. Takahashi, I. Kumagai, K. Araki, and K. Nishioka, Output Comparison of CPV and Flat‐Plate Systems in Japanese Meteorological Condition, AIP Conf. Proc. **1407**, 341 (2011).

12) Y. Ota, K. Araki, and K. Nishioka, Impact of volcanic ash on CPV system in Miyazaki Japan, AIP Conf. Proc. **1477**, 340 (2012).

13) Y. Ota and K. Nishioka, Two-Dimensional Mapping of Power Consumption Due to Series Resistance Evaluated by Simulator for Concentrator Photovoltaic Module, Jpn. J. Appl. Phys. **51**, 02BP03 (2012).

14) Y. Ota and K. Nishioka, Three-dimensional simulating of concentrator photovoltaic modules using ray trace and equivalent circuit simulators, Sol. Energy **86**, 476 (2012).

15) Y. Ota, T. Sueto, H. Nagai, K. Araki, and K. Nishioka, Reduction in Operating Temperature of 25 Series-Connected 820X Concentrator Photovoltaic Module, Jpn. J. Appl. Phys. **52**, 04CR03(2013).

16) J. C. Miñano, P. Benítez, P. Zamora, M. Buljan, R. Mohedano, and A. Santamaría, Free-form optics for Fresnel-lens-based photovoltaic concentrators ,Opt. Express **21**, A494 (2013).

17) M. Bosi and C. Pelosi, The potential of III-V semiconductors as terrestrial photovoltaic devices, Prog. Photovoltaics **15**, 51 (2007).

18) A. Aldossary, A. Algarue, S. Mahmoud, and R. K. AL-Dadah, Performance of Multi Junction Photovoltaic Cells with High Concentration Ratio, Energy Procedia **61**, 2258 (2014).

19) T. Takamoto, M. Kaneiwa, M. Imaizumi, and M. Yamaguchi, InGaP/GaAs-based multijunction solar cells, Prog. Photovoltaics **13**, 495 (2005).

20) M. Yamaguchi, T. Takamoto, and K. Araki, Super high-efficiency multi-junction and concentrator solar cells, Sol. Energy Mater. Sol. Cells **90**, 3068 (2006).

21) J. F. Geisz, S. Kurtz, M. W. Wanlass, J. S. Ward, A. Duda, D. J. Friedman, J. M. Olson, W. E. McMahon, T. E. Moriarty, and J. T. Kiehl, High-efficiency GaInP⁄GaAs⁄InGaAs triple-junction solar cells grown inverted with a metamorphic bottom junction, Appl. Phys. Lett. **91**, 023502 (2007).

22) W. Guter, J. Schöne, S. P. Philipps, M. Steiner, G. Siefer, A. Wekkeli, E. Welser, E. Oliva, A. W. Bett, and F. Dimroth, Current-matched triple-junction solar cell reaching 41.1% conversion efficiency under concentrated sunlight, Appl. Phys. Lett. **94**, 223504 (2009).

23) V. Sabnis, H. Yuen, and M. Wiemer, High-efficiency multijunction solar cells employing dilute nitrides, AIP Conf. Proc. **1477**, 14 (2012).

24) K. Sasaki, T. Agui, K. Nakaido, N. Takahashi, R. Onitsuka, and T. Takamoto, Development of InGaP/GaAs/InGaAs inverted triple junction concentrator solar cells, AIP Conf. Proc. **1556**, 22 (2013).

25) F. Dimroth, M. Grave, P. Beutel, U. Fiedeler, C. Karcher, T. N. D. Tibbits, E. Oliva, G. Siefer, M. Schachtner, A. Wekkeli, A. W. Bett, R. Krause, M. Piccin, N. Blanc, C. Drazek, E. Guiot, B. Ghyselen, T. Salvetat, A. Tauzin, T. Signamarcheix, A. Dobrich, T. Hannappel, and K. Schwarzburg, Wafer bonded four-junction GaInP/GaAs//GaInAsP/GaInAs concentrator solar cells with 44.7% efficiency, Prog. Photovoltaics **22**, 277 (2014).

26) H. A. Husna, N. Shibata, N. Sawano, S. Ueno, Y. Ota, T. Minemoto, K. Araki, K. Nishioka, Impact of spectral irradiance distribution and temperature on the outdoor performance of concentrator photovoltaic system, AIP Conf. Proc. **1556**, 252 (2013).

27) G. S. Kinsey, P. Hebert, K. E. Barbour, D. D. Krut, H. L. Cotal, R. A. Sherif, Concentrator multijunction solar cell characteristics under variable intensity and temperature, Prog. Photovoltaics **16**, 503 (2008).

28) K. Sasaki, T. Agui, K. Nakaido, N. Takahashi, R. Onitsuka, and T. Takamoto, Development of InGaP/GaAs/InGaAs inverted triple junction concentrator solar cells, AIP Conf. Proc. 1556, **22** (2013).

29) N. Hayashi, A. Matsushita, D. Inoue, M. Matsumoto, T. Nagata, H. Higuchi, Y. Aya, and T. Nakagawa, Nonuniformity Sunlight-Irradiation Effect on Photovoltaic

Performance of Concentrating Photovoltaic Using Microsolar Cells Without Secondary Optics, IEEE J. Photovolt. **6**, 350 (2016).

30) http://rredc.nrel.gov/solar/spectra/am1.5/

31) A. V. Tikhonravov, M. K. Trubetskov, and G. W. DeBell, Application of the needle optimization technique to the design of optical coatings, Appl. Opt. **35**, 5493 (1996).

32) A. V. Tikhonravov, M. K. Trubetskov, and G. W. DeBell, Optical coating design approaches based on the needle optimization technique, Appl. Opt. **46**, 704 (2007).

33) A. N. Tikhonov Jr., A. V. Tikhonravov, and M. K. Trubetskov, Second order optimization methods in the synthesis of multilayer coatings, J. Comput. Math. Math. Phys. **33**, 1339 - 1352 (1993).

34) M. A. Green, Third Generation Photovoltaics (Springer, Heidelberg, 2003) p. 69.

35) Y. Ota and K. Nishioka, Estimation of operating temperature and energy output of concentrator photovoltaic module under concentration conditions, Jap. J. Appl. Phys. **53**, 122301 (2014).

36) P. Espinet-González, C. Algora, N. Núñez, V. Orlando, M. Vázquez, J. Bautista, and K. Araki, Evaluation of the reliability of commercial concentrator triple-junction solar cells by means of accelerated life tests (ALT), AIP Conf. Proc. **1556**, 222 (2013).

37) P. Espinet-González, C. Algora, N. Núñez, V. Orlando, M. Vázquez, J. Bautista, and K. Araki, Temperature accelerated life test on commercial concentrator III–V triple-junction solar cells and reliability analysis as a function of the operating temperature, Prog. Photovoltaics **23**, 559 (2015).

38) P. Espinet-González, R. Romero, V. Orlando, M. Gabas, N. Núñez, M. Vázquez, S. Palanco, S. Bijani, Y. Contreras, B. Galiana, C. Algora, K. Araki, Case study in

failure analysis of accelerated life tests (ALT) on III-V commercial triple-junction concentrator solar cells, Proc. 39th IEEE Photovoltaic Specialists Conf. (PVSC), 2013, 1666.

39) C. Algora and I. Rey-Stolle, Hand Book of Concentrator Photovoltaic Technology, (Wiley, Chichester, 2016) p. 545.

40) V. Orlando, M. Gabás, B. Galiana, P. Espinet-González, S. Palanco, N. Núñez, M. Vázquez, K. Araki and C. Algora, Failure analysis on lattice matched GaInP/Ga(In)As/Ge commercial concentrator solar cells after temperature accelerated life tests, Prog. Photovoltaics (in press) [DOI: 10.1002/pip.2818].

41) http://app0.infoc.nedo.go.jp/

Chapter 4

111 sun concentrator photovoltaic module with wide acceptance angle that can efficiently operate using 30-min intermittent tracking system

4.1. Introduction

In this section we introduce the second problem that we are trying to overcome in CPV systems which is the need for high precision expensive tracking system. A new approach to improve the CPV system performance by using a mid-concentration wide-acceptance-angle lens to concentrate the solar light was introduced. This wide-acceptance-angle lens will allow us to use 30-min intermittent tracking method that does not require a special high-precision CPV tracking system. This will allow the reduction of costs and complexity, because a large percentage of the cost of a typical CPV system comes from the expensive accurate tracking system.

The concentration in a CPV system is achieved by replacing the aperture of the system with an optical system, which could be an imaging or non-imaging type [1-2]. A CPV system uses inexpensive optical elements, such as Fresnel lenses [3] or parabolic mirrors [4], to focus sunlight onto a high-efficiency multijunction solar cell [5-13].

The need for a mechanical tracker that allows the gathering of direct radiation is one of the main differences between CPV systems and flat panel PV systems. This tracker follows the sun's position to keep the concentration spot focused on the multijunction solar cell. High-precision dual-axis trackers are necessary for high concentrator photovoltaic (HCPV: more than 300 suns) systems, due to the low achieved acceptance angles (≤1°), as it is impossible to achieve both high geometrical concentration ratio and wide-acceptance-angle and in the same system [14]. The need for tracking is very low in low concentrator photovoltaic (LCPV: from 2 to 100 suns) systems because it has considerably higher acceptance angles. The CPV system in this study falls in the medium concentrator photovoltaic (MCPV: from 100 to 300 suns) category, which lies between the two above mentioned CPV systems types. Achieving medium concentration ratios while using precise tracking is a major drawback of MCPV systems, which implies unjustified cost for the system. The main purpose of this research is to address this problem and prove that an inexpensive and relatively low-accuracy tracking system can achieve good performance, despite the high tracking error angle resulting from using it.

The current system, which was investigated earlier by Araki et al, uses a 30-min intermittent tracking system, which moves one time only every 30 min and relocate the tracker direction into an intermediate point that allows the lowest achievable tracking error angle. This is combined with a high-acceptance-angle dielectric concentrator lens that allows this low precision technique to be feasible [15].

In this study, we characterized the concentrator performance and compared it to the experimental results by building optical, thermal, and electrical models. At any particular time, the angle between the sun position vector and the collector's normal vector in the same coordination is called the tracking error angle [16]. The main target of this study was to evaluatethe MCPV system performance at 0° tracking error and at the highest calculated tracking error angle to determine whether the performance of the system was affected by the large tracking error angle.

4.2. System design

4.2.1 Optical model

The optical system used in this study consisted of a refractive and dielectric concentrator with a primary optical element (POE) [17] coupled with secondary optical element (SOE) dielectric kaleidoscope (homogenizer) [18]. This coupling was applied to reduce the chromatic aberration losses caused by the POE [19]. We used ZEMAX which is a commercial optical simulation software to conduct Monte-Carlo ray-tracing simulations for the optical system under different tracking error conditions, as shown in Fig. 4-1(a). A schematic diagram of the optical system is shown in Fig. 4-1(b). The aperture of the lens was 55 × 55 mm^2 and the focal length was 88 mm. The entry aperture of the homogenizer had an area of 8.6 × 8.6 mm^2, while the exit aperture area was 5.2 × 5.2 mm^2. The height of the homogenizer was 25.5 mm. When choosing the optical material for the CPV system one of the main important factors we should consider is the outdoor durability. To increase the Concentration Acceptance Product (CAP) [20] and reduce the focal distance another consideration was taking into account, which is the need of a high refractive index for the lens material. We chose S-TIM2 glass, with a refractive index of n = 1.62, as the optical system material. The geometric concentration ratio for this system was 111. For the ray-tracing simulation we used the AM 1.5D (total power: 900 W/m^2) ASTM G173-03 solar spectrum [21]. The performance of the module is strongly affected by spectral variation due to the use of a multijunction solar cell and the optical design [22]. Ray-tracing was performed in the effective wavelength range of the employed lattice-matched (InGaP/InGaAs/Ge) solar cell, from 400 to 1700 nm.

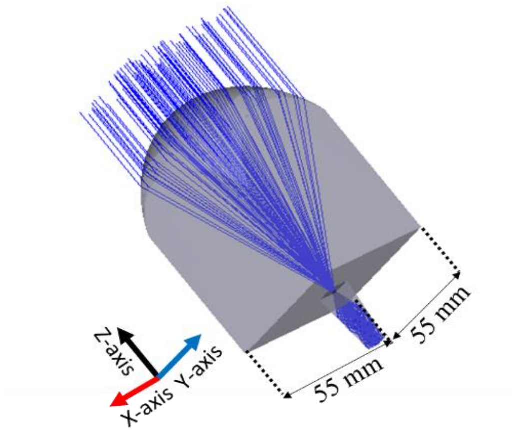

(a) optical model is ZEMAX.

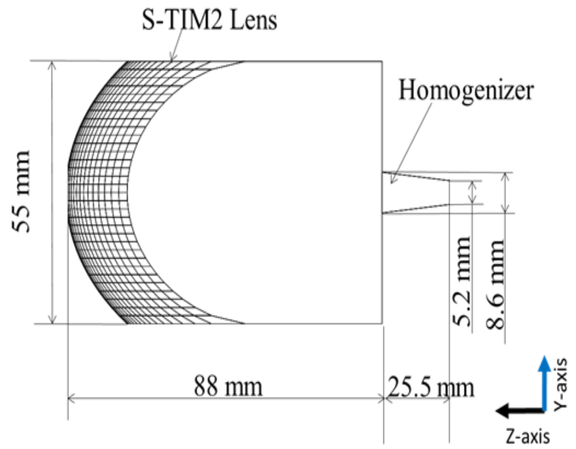

(b) Schematic of the dimensions of the optical model.

Fig. 4- 1: Optical model.

The results for optical simulation and their relation to the tracking error in the *x* and *y* directions were obtained from the optical output and tracking error vector calculations.

4.2.2 Thermal model

A COMSOL Multiphysics (COMSOL inc.) model based on the real module was built. A schematic of the geometrical thermal model and real CPV module are shown in Figs 4-2(a) and 4-2(b), respectively. The thicknesses of the components around the multijunction solar cell are presented in Table 4-1.

Table 4- 1: Structure thickness around the multijunction solar cell.

Layer name	**Thickness (mm)**
Solar cell	0.17
Solder	0.05
Copper ribbon	0.05
Insulation sheet	0.5
Aluminum stage	3
Insulation layer	0.5
Aluminum chassis	10

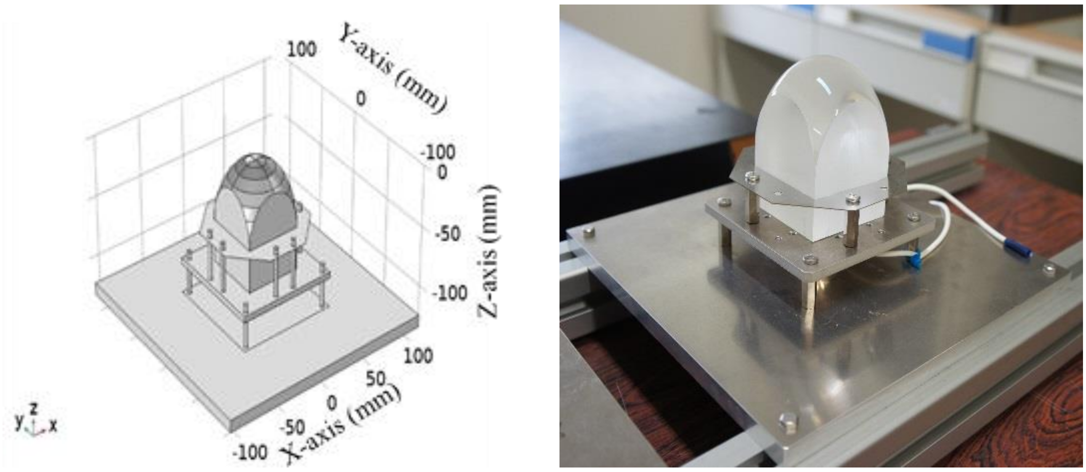

(a) (b)

Fig. 4- 2: Thermal model. (a) schematic of the geometrical CPV thermal model in COMSOL. (b) Real CPV module.

A more detailed schematic of the structure around the multijunction solar cell is shown in Fig. 4-3. A gray colored cross-sectional view in the thermal model is also shown in Fig. 4-3.

A precision platinum temperature sensor (Pt100) is inserted into a drilled hole in a chassis under the structure around the solar cell shown in Fig. 4-3, which will be further explained in the experimental method section.

The receiver consisted of a homogenizer, a III–V multijunction solar cell, a solder, a copper ribbon electrode, insulation materials, and an aluminum stage mounted on an aluminum chassis. The thermal conductivity of the thin insulation layer between the stage and the chassis was 0.72 W/(m·K), while that of the insulation sheet between the copper ribbon and the stage was 5 W/(m·K).

The multijunction solar cell was modeled as a heat source. The heat power was integrated into the heat transfer model and was calculated from the direct normal irradiance (DNI) using:

$$P = DNI \cdot A_{\text{cell}} \cdot C \cdot \eta_{\text{op}} \cdot (1 - \eta), \tag{4.1}$$

where A_{cell} is the multijunction solar cell area, C is the concentration ratio, η_{op} is the optical efficiency, and η is the electrical efficiency [23]. A_{cell} was fixed at 5.2×5.2 mm^2.

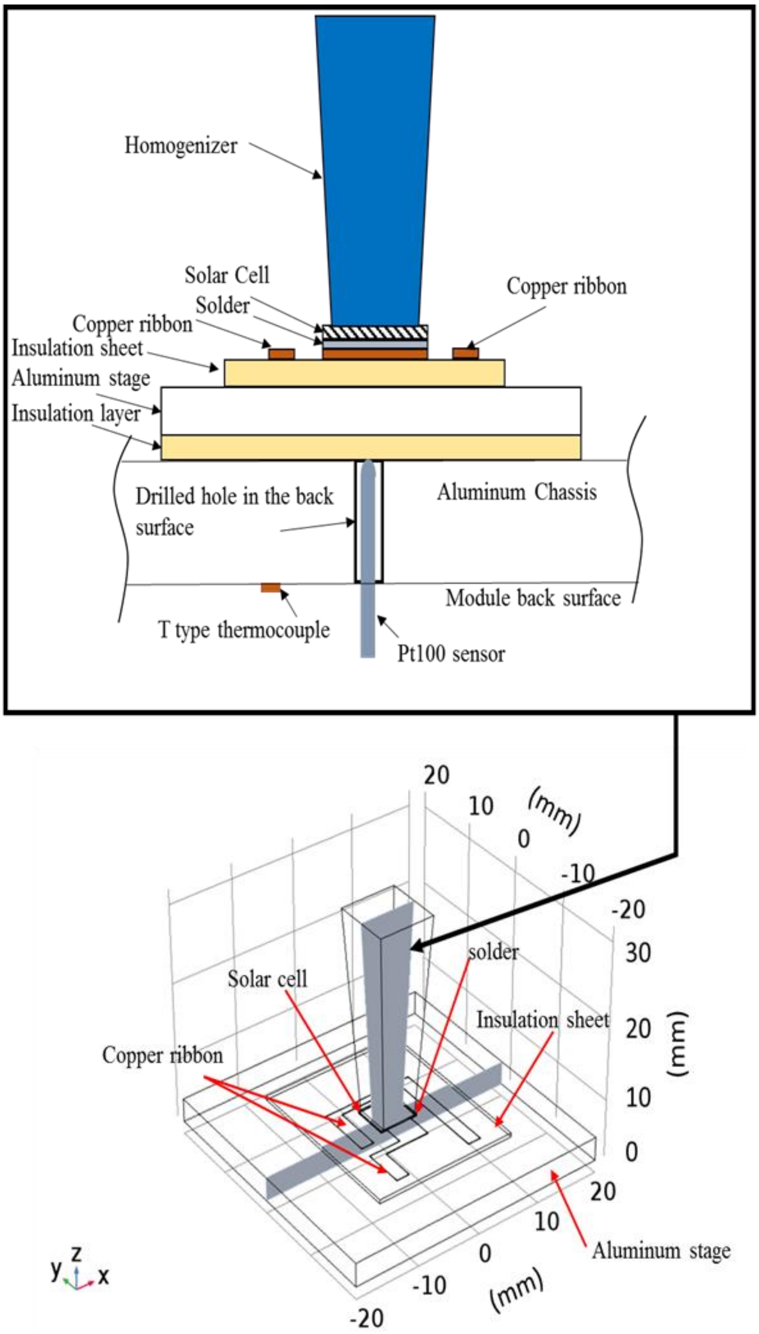

Fig. 4- 3: Detailed schematic for the structure around the multijunction solar cell.

Ambient temperature and DNI were measured throughout the day on February 15, 2017 and were used in the thermal model. We integrated the obtained irradiance distribution on the solar cell from the optical simulation into the thermal model to obtain the temperature distribution on the surface of the multijunction solar cell at different tracking error angles. This integration allowed us to analyze the temperature change across the surface of the solar cell and their relation to the irradiance distribution at different tracking error angles. The heat transfer through the solid layers was assumed to occur via conduction. All free exposed areas in the model were assumed to release heat through convection and radiation.

A windless condition was assumed because the experimentally measured wind speeds were very low. Calculations of convection and radiation heat transfer coefficients h ($W/m^2 \cdot K$) were conducted for all surfaces.

4.2.3 Electrical model

In order to analyze the electrical performance of the MCPV module, we need to obtain the photocurrent distribution for each sub-cell, making it possible to determine the total photocurrent value and current matching ratio. An artificial spectrum S_{RS} (λ) was used for the emitting source in a ZEMAX simulation to predict the photocurrent distribution as described in section 3.2.4 in chapter 3 but by using the real spectrum. The integration of this artificial spectrum for each wavelength range and for the specific EQE in that range weights the wavelength potential to generate an electron–hole pair in the solar cell. We obtained this artificial spectrum by taking the multijunction solar cell EQE into account using the following equation:

$$S_{RS}(\lambda) = E_{RS}(\lambda) \cdot \frac{q\lambda}{h_p c} \cdot EQE(\lambda), \tag{4.2}$$

where $S_{\mathrm{RS}}(\lambda)$ is the artificial spectrum for the photocurrent (the unit for the integration of this spectrum is typically expressed in mA/cm^2); $E_{\mathrm{RS}}(\lambda)$ ($W/m^2/nm$) is the real measured direct spectrum of the sun at the calculation time on February 15, 2017; λ (nm) is the wavelength; $q = 1.602 \times 10^{-19}$ C represents the charge of a single electron; $h_{\mathrm{p}} = 6.626 \times 10^{-34}$ J·s is Planck's constant; and $c = 2.998 \times 10^{8}$ $m \cdot s^{-1}$ is the speed of light in vacuum. The artificial spectrum for the photocurrent was divided into several parts corresponding to every sub-cell. The resulted simulation output represented the photocurrent distribution for each sub-cell. We used a real spectrum in the calculations, because the current–voltage (*I*–*V*) characteristics are significantly affected by the spectrum [24, 25]. In Fig. 4-4, we illustrate the difference between the AM 1.5D spectrum and the spectrum measured on February 15 at 12:30.

Equivalent circuit calculations were carried out using SPICE (Cadence Design System) [26, 27]. The single-unit equivalent circuit model used is shown in Fig. 4-5. The parameters of the circuit are shown in Table 4-2.

Table 4- 2: Parameters of the single unit equivalent circuit model.

Symbol	Name	Value	Unit
R_{sh1}	Top sub-cell shunt resistance	3000k	Ω
R_{sh2}	Middle sub-cell shunt resistance	1500k	Ω
R_{sh3}	Bottom sub-cell shunt resistance	115	Ω
R_{tl1}	Tunnel junction resistance	0.0012	Ω
R_{tl2}	Tunnel junction resistance	0.0008	Ω
R_{el}	Circuit series resistance	0.0236	Ω

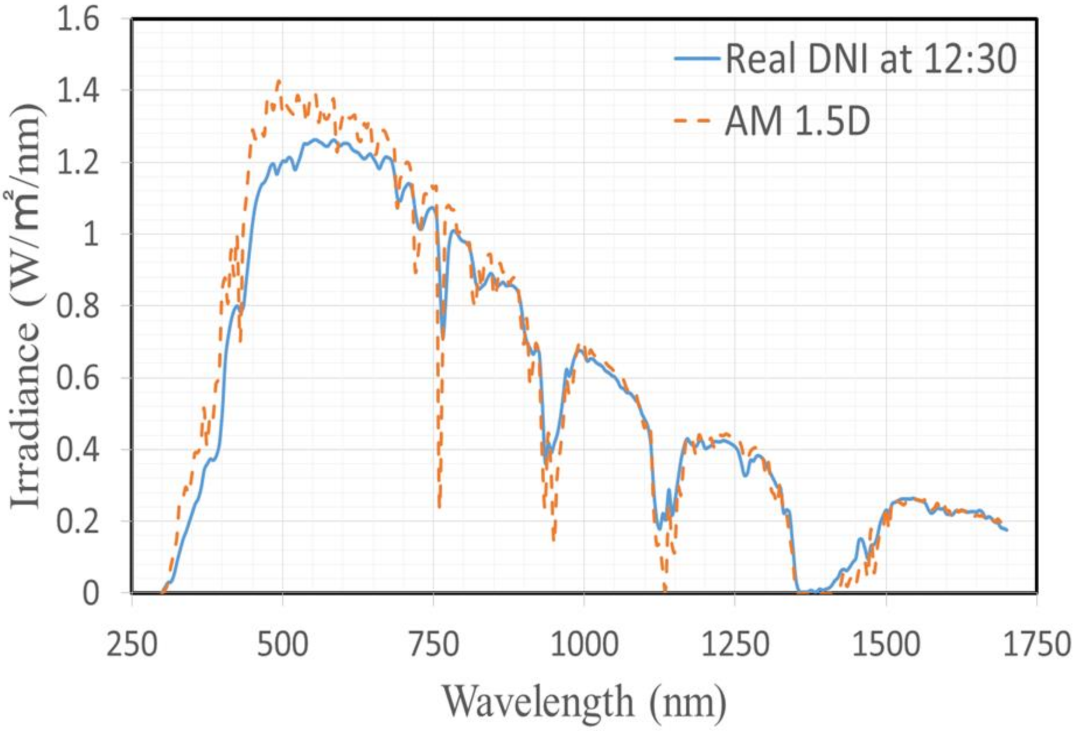

Fig. 4- 4: Difference between the AM 1.5D spectrum and spectrum measured on February 15, 2017 at 12:30 when the tracking error angle was 0°.

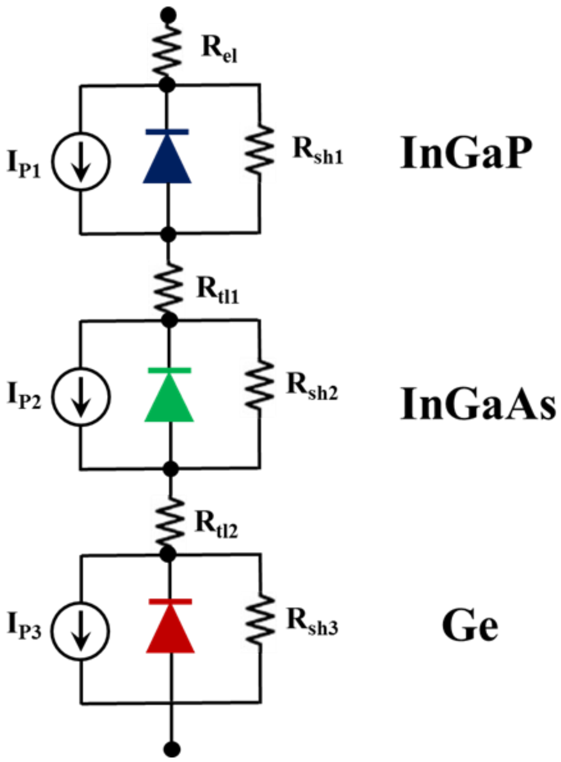

Fig. 4- 5: Equivalent circuit model for the multijunction solar cell.

4.3. Experimental methods

We mounted two CPV modules (Fig. 4-6(a)) on a 30-min intermittent advanced feed forward tracking system (Fig. 4-6(b)), located at the outdoor test site in the University of Miyazaki, Miyazaki city, Japan. The tracking system, including the tracking control and the power source, moves one time every 30 min for tracking. The rest of the time, the tracking system is in its lowest possible electricity consumption state to save energy.

We used one module for measuring the *I–V* characteristics and the other for measuring the cell temperature, because measuring the solar cell temperature in a CPV module is difficult procedure and it is usually not possible without damaging the supporting elements surrounding the solar cell. The thermocouples and the Pt100 sensor located on the back surface of the module are shown in Figure 6(c). Zooming in Fig. 6(c) shows the distance between the Pt100 sensor and the thermocouples (T-1 represents Pt100 and T-2 to T-4 represent the thermocouples attached to the back surface of the CPV module).

We drilled a hole in the aluminum chassis of one module up to the aluminum stage (no further drilling was carried out, for fear of damaging the solar cell, see Fig. 4-3). The Pt100 sensor was inserted into the drilled hole and greased using a high-thermal-conductance silicone. Three T-type thermocouples were used to measure the thermal performance on the back surface of the chassis at different points. The thermocouples were fixed on the back surface using an aluminum tape. The temperature difference between the solar cell and the back surface of the CPV module can be large, but the

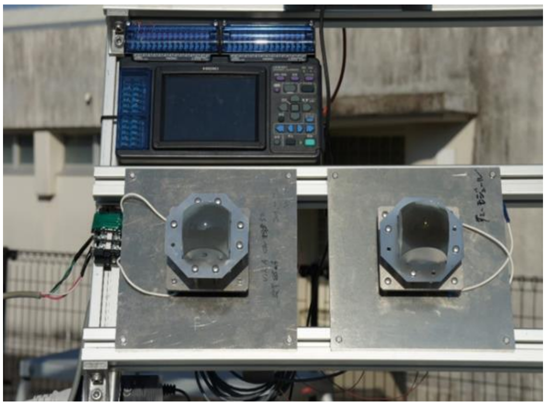

(a)

(b)

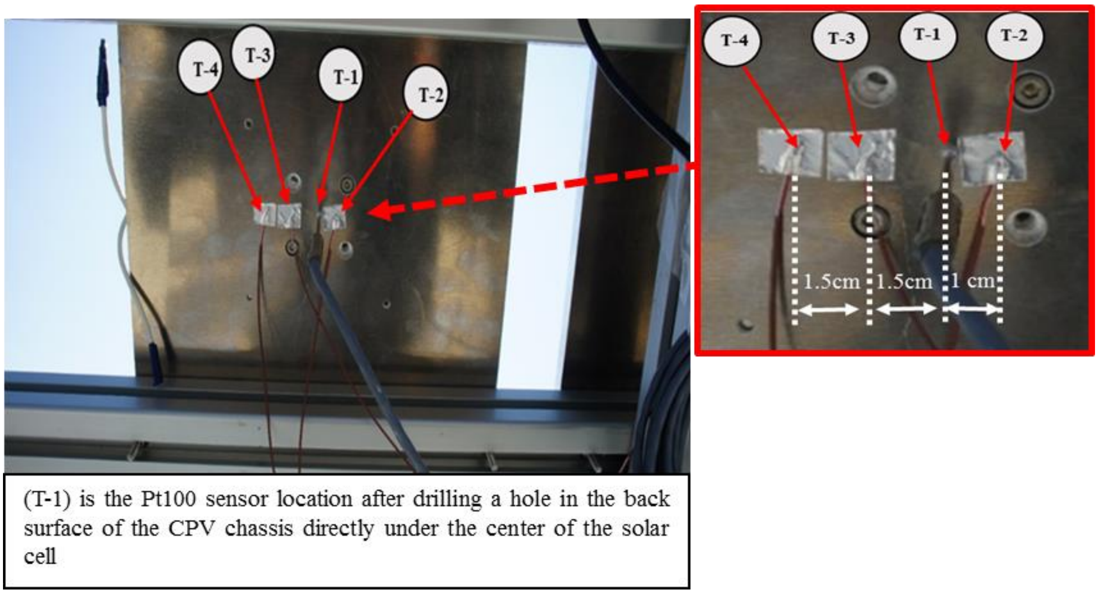

(c)

Fig. 4- 6: Experimental procedure equipment, (a) The two wide acceptance angle CPV modules mounted on the tracking system. (b) Advanced feed forward tracking system. (c) Thermocouples and Pt100 sensor located on the back surface of the module.

previously mentioned drilling procedure allowed a better understanding of the thermal performance and higher accuracy in the measurements of solar cell temperature.

We used a data logger (HIOKI, LR8401) to register the temperatures at 1-s intervals from 8:30 to 15:30 on February 15, 2017.

We measured the DNI using a pyrheliometer (EKO, MS-56). The spectral characteristics of the solar irradiance were obtained using a spectroradiometer (EKO, MS-700N) for the wavelength range of 350–1050 nm, while another spectroradiometer (EKO, MS-712) was used for the wavelength range of 900–1700 nm.

We traced the *I*–*V* characteristics of the CPV module using *I*–*V* tracers (EKO, MP-160), where electrical characteristics such as the open circuit voltage (V_{oc}), short circuit current (I_{sc}), maximum power point (P_{mp}), maximum power voltage (V_{mp}), maximum power current (I_{mp}), and fill factor (*FF*) were registered. The *I*–*V* measurements were logged on a computer once per minute and then transferred to a database.

4.4. Results and discussion

4.4.1. Optical simulation results

We conducted Monte-Carlo ray tracing simulations in ZEMAX and results showed good uniform irradiance over the multijunction solar cell surface, with a peak irradiance of 9.13 W/cm^2, as shown in Fig. 4-7. The peak to average irradiance ratio (PAR) was 1.15, which was an acceptable value for the multijunction solar cell knowing that the ideal value is 1. The achieved total optical efficiency of the model was 86.9%, which was calculated from the ratio of the total irradiance value on the solar cell surface to the irradiance value on the optical system. We calculated the relationship of relative optical efficiency (defined as the ratio of the optical efficiency at zero tracking error to the optical efficiency at a particular tracking error) with tracking error on the *x*- and *y*-axes of the tracker, and the results are shown in Fig. 4-8. The projection of the 0.9 relative optical efficiency line on the *x*-and *y*-axes in the contour plot in Fig. 4-8 determines the acceptance angle value, as a result, we obtained a wide-acceptance-angle of 4.5° for the CPV module at 0.9 relative optical efficiency.

The maximum tracking error reached 3.65° on the *x*-axis for the module using 30-min intermittent tracking in the period between 12:15 and 12:45, while the *y*-axis tracking error angle was considerably lower. These tracking error angles can be obtained from the dotted black line projection on the *x*- and *y*-axes in Fig. 4-8. The sun movement at noon is generally on the *x*-axis direction, which indicates a marked change in the azimuth angle. The tracking error angle change in the morning between 8:45 and 9:15 is also illustrated in Fig. 4-8 and indecated by the green dotted line. The sun movement on both the x- and y-axes directions in the morning indicates a big change in the altitude and azimuth angles. The results showed that the relative optical efficiencies of the module in the worst case in the morning and at noon were considerably high (≥99%), which means that the tracking error angle for 30-min intermittent tracking at its maximum was within the acceptable range for the module to operate at a maximum efficiency.

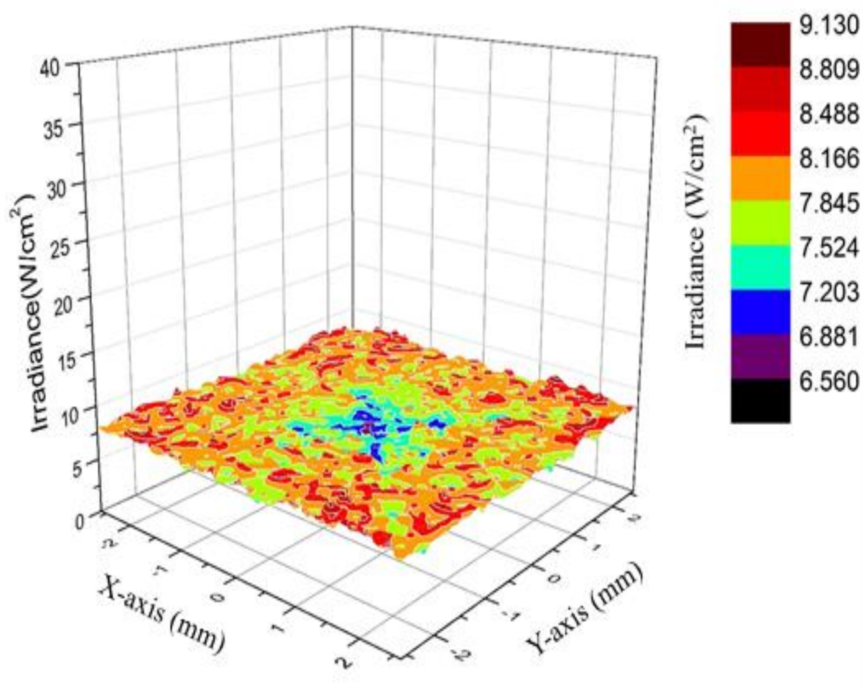

Fig. 4- 7: Irradiance distribution on the surface of the multijunction solar cell.

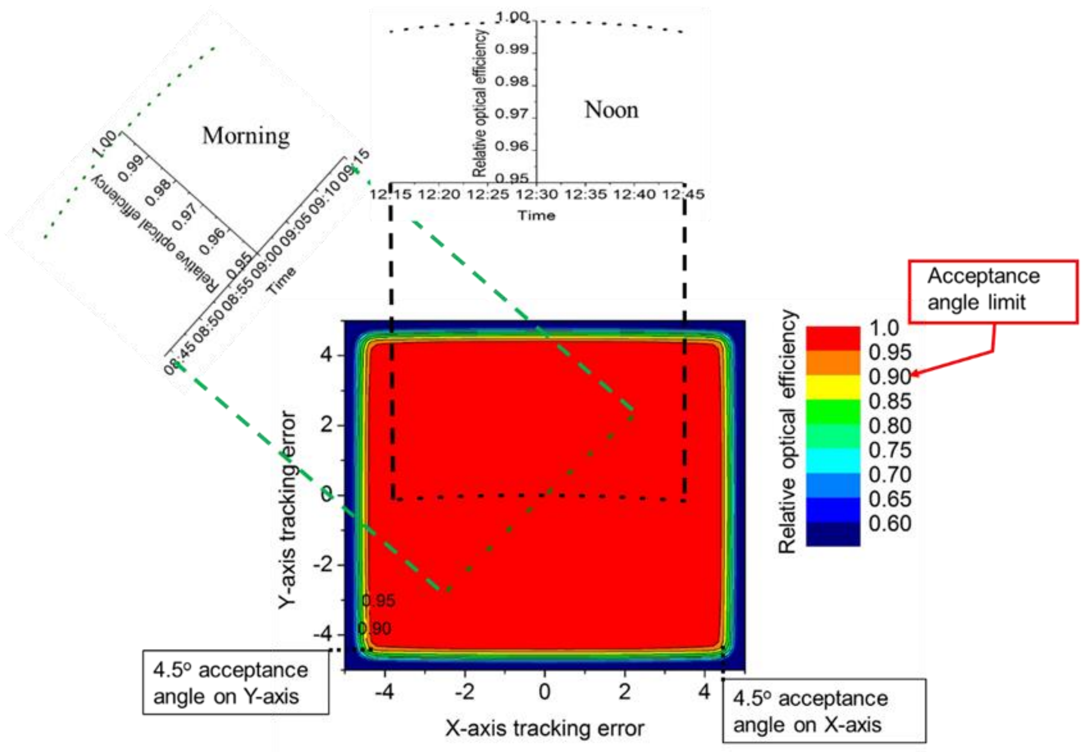

Fig. 4- 8: Relative optical efficiency relation with tracking error on the *x* and *y*-axis of the tracker.

4.4.2. Thermal simulation and experiment results

We measured the temperatures of the chassis's back and upper surfaces through the experimental procedure described in Section 4.3 in this chapter. The temperatures measured throughout the day on February 15, 2017 are shown in Fig. 4-9. We can easily observe the temperature difference between the back surface, indicated by T-2, T-3, and T-4 (see Fig. 6(c)), and the upper surface temperature of the chassis, indicated by T-1 closer to the multijunction solar cell where the Pt100 sensor was located. The difference at some points between the upper and back surfaces reached approximately 5°C and it is indicated with arrows in Fig. 4-9.

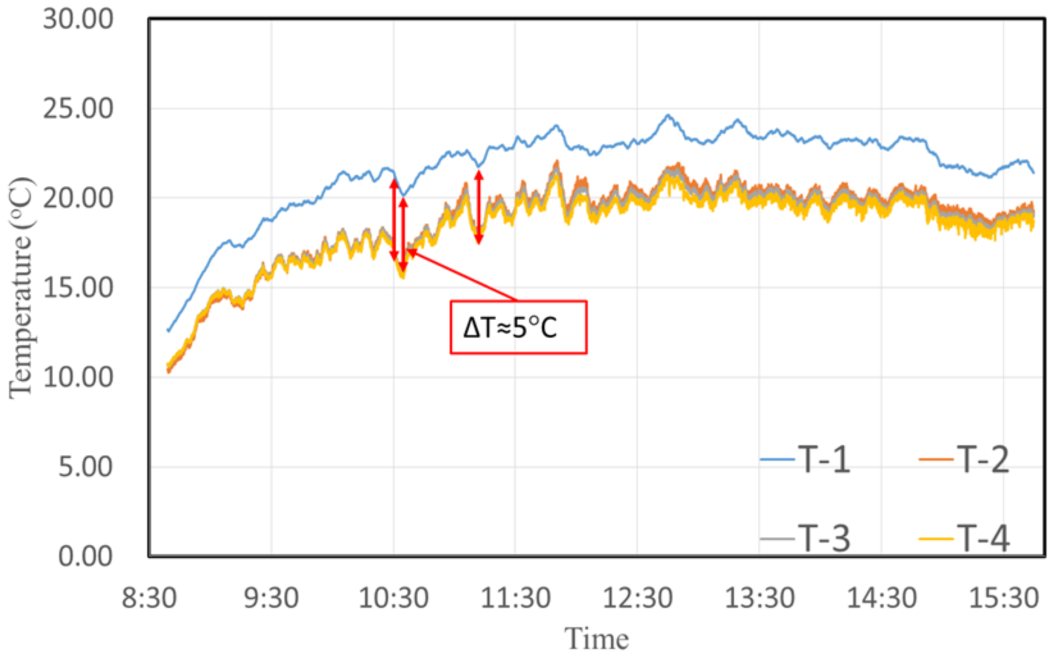

Fig. 4- 9: Measured CPV back surface and chassis temperatures on February 15, 2017 throughout the day.

We obtained the thermal simulation parameters from measurements at an intermediate time of day: at 12:30 when the tracking error angle was 0°, and at 12:15 when the tracking error angle was at its highest value. The temperatures measured at 12:30 and 12:15 are shown in Table 4-3. The results for the thermal simulation at 12:30

are shown in Figs.4-10(a) and 4-10(b), where Fig. 4-10(a) illustrates the temperature distribution across the multijunction solar cell, while Fig. 4-10(b) shows the distribution on the top surface of the chassis, where the Pt100 sensor was located. The simulation results (Fig. 4-10(b)) show good agreement with the experimental results (T-1 in Table 4-3), with less than 2% difference. The temperature of the multijunction solar cell reached a maximum of 28.2°C (Fig.4- 10(a)).

Table 4- 3: Measured experimental temperatures in the CPV module

Time	T-1(°C)	T-2(°C)	T-3(°C)	T-4(°C)
12:30	23.02	20.47	20.19	19.8
12:15	22.87	19.73	19.53	19.16

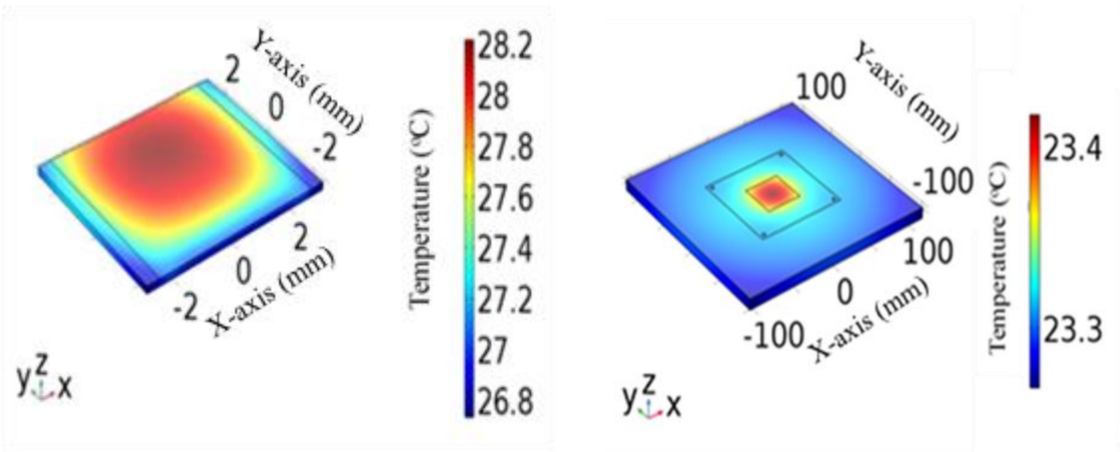

(a) Temperature distribution on the multijunction solar cell.

(b) Temperature distribution on the upper surface of the CPV chassis.

Fig. 4- 10: Thermal simulation results at 12:30 on February 15.

Although the change in the temperature across the solar cell surface is less than 1.4°C, there was a noticeable decrease in the temperature in the front part of the multijunction solar cell (y = -1 mm to y = -2 mm). This was because of the structure of the copper ribbon electrode in that area. The copper ribbon worked as a heat conductor and released heat from the front part of the multijunction solar cell, owing to its high thermal conductivity and relatively large area in the front part of the structure.

We did the same calculation for the heat transfer model at 12:15, when the tracking error angle reached 3.65°. By doing this calculation, we were able to show the effect of the tracking error on the multijunction solar cell thermal performance. Fig. 4-11(a) shows the temperature distribution on the surface of the multijunction solar cell, while Fig. 4-11(b) shows the temperature distribution on the upper surface of the chassis. Although we integrated the irradiance distribution in the heat transfer model to show the effect of the tracking error on the temperature distribution, the results showed no significant change in the temperature distribution for a tracking error of 3.65°, owing to the large acceptance angle of the lens. The maximum resulting temperature of the multijunction solar cell was 27.6 °C (Fig. 4-11(a)). Fig. 4-11(b) shows the upper surface temperature of the chassis, which was 22.8 °C, while the experimental resulted temperature measured by the T-1 sensor was 22.87 °C at 12:15 as shown in Table 4-3, which represented less than 2% difference from the experimental results. The resulted temperature differences across the multijunction solar cell surface for both cases at 12:30 and 12:15 showed a small change in the temperature of the cell (≤ 1.4 °C). Most multijunction solar cells used in CPV systems are designed to work at temperatures below 80°C [28], which means that there will be no problem with respect to the solar cell temperature for the current CPV system.

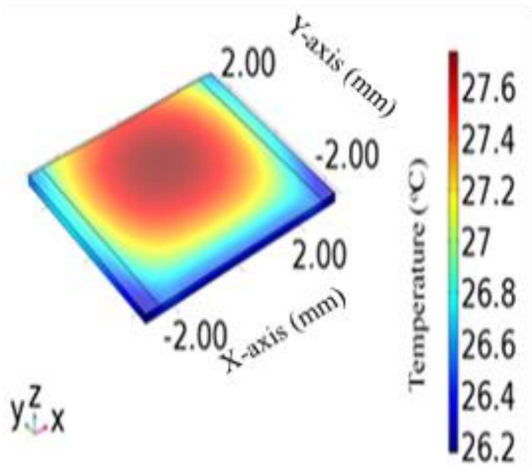

(a)

Temperature distribution on the solar cell.

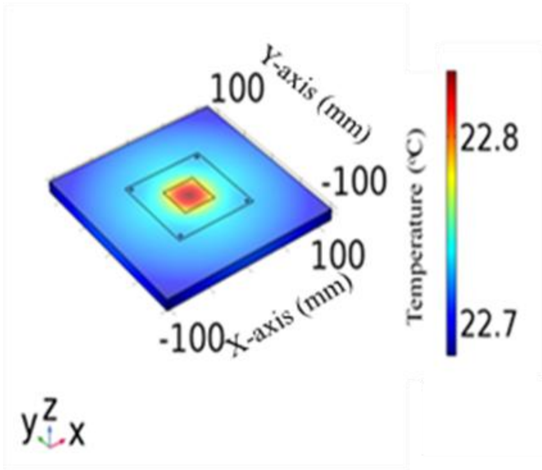

(b)

Temperature distribution on the upper surface of the CPV chassis.

Fig. 4- 11: Thermal results at 12:15 on February 15.

An analysis of the heating in the focal point of the lens was conducted to determine the effects of the concentration at the focal point on the lens material and optical performance. The difference in collected power of the optical model between two detectors fixed above and beneath the focal point was calculated to obtain the total power at the focal point, as shown in Fig. 4-12. We also analyzed the distribution of the resulting irradiance at the focal point in ZEMAX and then integrated it into a COMSOL thermal model to obtain the heat power distribution. Fig. 4-12 shows the heat power distribution at the focal point. The highest heat power value was 6×10^6 W/m^3. The heat distribution at the focal point showed that power was along the *z*-axis and not concentrated at a single point, with heat power decreasing from the focal point toward the outside. The temperature change along the *z*-axis between the two detectors was between 12.8°C and 13.9°C, which means an increase of 1°C. The results proved that there were no significant changes in the lens' optical characteristics because of the low temperature at the focal point. The low temperature was due to the low absorption coefficient for S-TIM2 glass, and this temperature was within the accepted temperature range for S-TIM2 glass.

A larger increase in temperature and release of heat at the focal point are expected for lenses made from PMMA, or lenses with higher absorption coefficients.

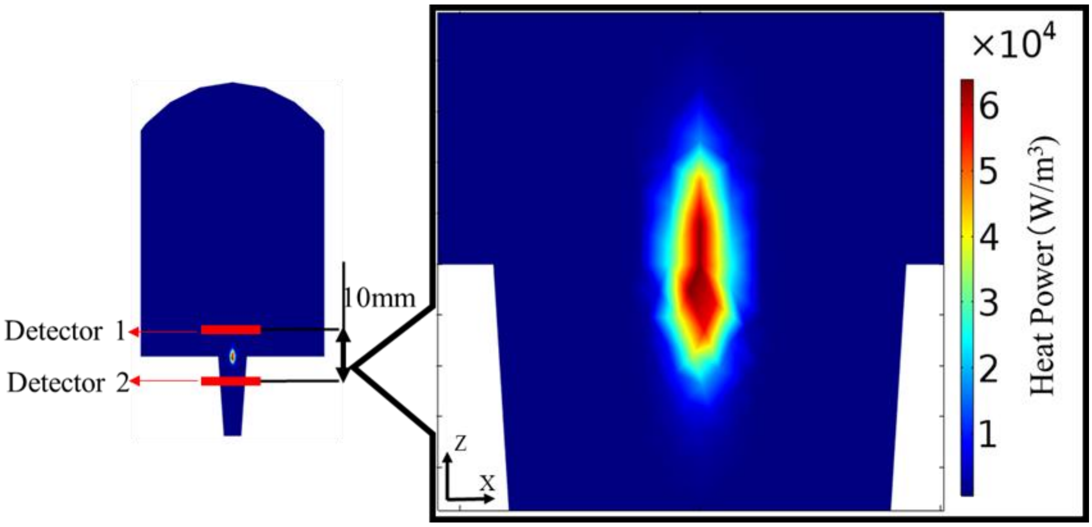

Fig. 4- 12: CPV focal point heat power distribution.

4.4.3. Electrical simulation and experiment results

We calculated the generated photocurrents in the top, middle, and bottom sub-cells using the artificial spectrum resulting from Eq. (4.2) in ZEMAX simulation. The resulting photocurrents distribution at 12:30 without tracking error and at 12:15 with the maximum tracking error are shown in Figs. 4-13(a) and 4-13(b), respectively. The tracking error showed a more pronounced effect on the photocurrent distribution than the temperature distribution in the multijunction solar cell.

The resulting photocurrents in each sub-cell at two different times of the day for multijunction solar cell with and without concentration condition are shown in Table 4-4. The measured DNI value at 12:30 was 850.96 W/m^2, while it was slightly higher at 12:15, with a value of 865.22 W/m^2, which explains the slightly higher resulting photocurrents at 12:15.

Table 4- 4: Resulting photocurrent for each sub-cell at 12:30 and 12:15 on 15 February 2017.

	Time	**Top sub-cell**	**Middle sub-cell**	**Bottom sub-cell**
without concentration	12:30	3.283 (mA)	3.676 (mA)	4.808 (mA)
	12:15	3.338 (mA)	3.738 (mA)	4.889 (mA)
with concentration	12:30	0.3162 (A)	0.3770 (A)	0.4918 (A)
	12:15	0.3203 (A)	0.3820 (A)	0.4985 (A)

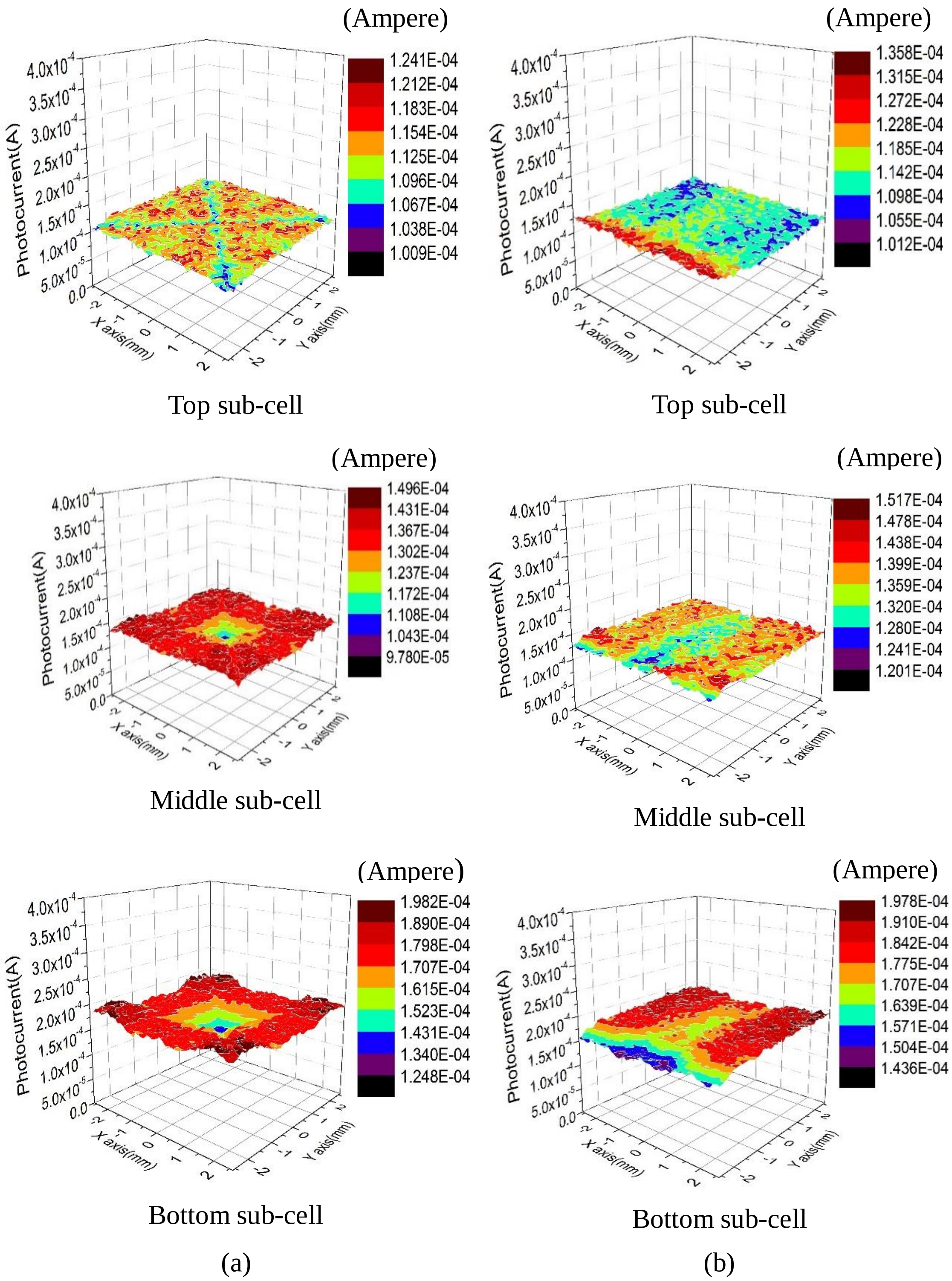

Fig. 4- 13: Resulting distribution of photocurrent generated from each sub-cell (top sub-cell, middle sub-cell, and bottom sub-cell), (a) Distribution of photocurrent at 12:30. (b) Distribution of photocurrent at 12:15.

The current matching ratio for the multijunction solar cell without concentration was calculated from the following:

$$\mathrm{CM}_{Mid}^{Top}(E_{RS}) = \frac{I_{p,top}(E_{RS})}{I_{p,mid}(E_{RS})} \quad , \tag{4.3}$$

where the $I_{\mathrm{p,top}}(E_{RS})$ was the top sub-cell photocurrent and $I_{\mathrm{p,mid}}(E_{RS})$ was the middle sub-cell photocurrent both calculated for the real spectrum.

The current matching ratio for the multijunction solar cell with concentration was calculated from:

$$\mathrm{CM}_{Mid}^{Top}(E_{RS}.Con) = \frac{I_{p,top}(E_{RS}.Con)}{I_{p,mid}(E_{RS}.Con)} \ , \tag{4.4}$$

where $I_{\mathrm{p,top}}(E_{RS}.Con)$ was the top sub-cell photocurrent and $I_{\mathrm{p,mid}}(E_{RS}.Con)$ was the middle sub-cell photocurrent both calculated for the real spectrum after concentration.

Similar to the previous equation, we can calculate optical matching value OM from Eqs. (4.3) and (4.4) using the following equation:

$$\mathrm{OM}_{Mid}^{Top} = \frac{\mathrm{CM}_{Mid}^{Top}(E_{RS}.Con)}{\mathrm{CM}_{Mid}^{Top}(E_{RS})} \ . \tag{4.5}$$

The results for current matching and optical matching are shown in Table 4-5. A four digit number was decided as a significant figure after we carried out the calculations for 10 times to inspect the change in the values due to errors in simulation. We can notice the decrease in the solar cell current matching ratio after concentration compared to the case without concentration due to the losses and spectral sensitivity of the optical system. The change in the current matching ratio after concentration between the case at 12:30 with no tracking error and at 12:15 with the largest tracking error (tracking error angle of 3.65°) is significantly small and almost neglected which indicates the validity of the optical system with wide acceptance angle of 4.5°.

Table 4- 5: Resulting current matching and optical matching ratios for the multijunction solar cell.

Time	CM for solar cell without concentration	CM for solar cell with concentration	OM
12:30	0.8931	0.8387	0.9391
12:15	0.8931	0.8385	0.9388

OM value can become higher than 1 in the following case; $\mathrm{CM}_{Mid}^{Top}(AM1.5) \leq 1$ for top limited sub-cell and we used a concentrator with an optical material which has higher transmittance for spectrum in the top sub-cell wavelength range than middle-sub cell wavelength range (optical material transmittance which is highly wavelength dependent or selectively absorb light). This will lead to lower photocurrent in the middle sub-cell under concentration. In the special case when middle sub-cell photocurrent become smaller than the top sub-cell photocurrent then $\mathrm{CM}_{Mid}^{Top}(E_{RS}.Con) > 1.$ In this case the overall $\mathrm{OM}_{Mid}^{Top} > 1$, which indicates that the solar cell short current will be decided by the middle sub-cell beneath the concentrator, although the cell was originally designed to be top sub-cell limited. In this system, OM is less than one, which means that the transmittance was lower for the optics in the short wavelength range (rich red spectrum) and the solar cell performance was most affected by the top sub-cell [29].

We calculate the *I–V* curve characteristics and compare them to the real experimental results. We conducted the simulation using a single unit equivalent circuit model in SPICE and the *I–V* curve results for the cases at both 12:30 and 12:15 are shown in Fig. 4-14(a) and Fig. 4-14(b), respectively. The experiment electrical results and simulation characteristics at 12:30 are shown in Table 4-6. There were noticeable differences in short circuit current and module efficiency between the simulation and experimental values. These differences are expected to be caused by the excessive use of silicone sealing in the real module, which was not considered in the current optical model.

The results for the 12:15 tracking error conditions are shown in Fig. 4-14(b) and Table 4-7. As in previous results, the main differences were observed in the short circuit current and module efficiency, and the expected reason for the difference was the excessive silicone sealing around the multijunction solar cell.

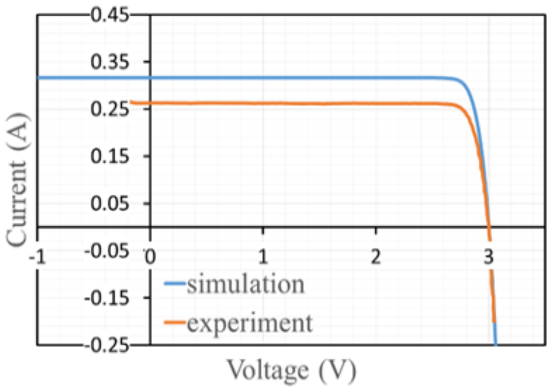

(a) *I–V* characteristic curves at 12:30.

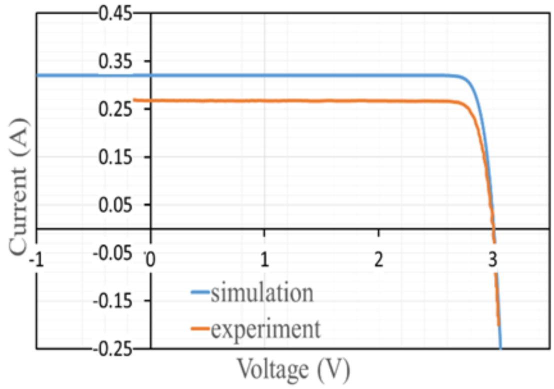

(b) *I–V* characteristic curves at 12:15.

Fig. 4- 14: Simulated and experimental *I–V* characteristic curves of the CPV module.

Table 4- 6: Electrical characteristics of the multijunction solar cell at 12:30.

Simulation				
I_{sc} (A)	V_{oc} (V)	P_m (W)	*FF*	Module efficiency (%)
0.3162	3.0012	0.8489	0.8945	32.9874
Experiment				
I_{sc} (A)	V_{oc} (V)	P_m (W)	*FF*	Module efficiency (%)
0.2628	3.0007	0.6979	0.8852	27.1147

Table 4- 7: Electrical characteristics of the multijunction solar cell at 12:15.

Simulation				
I_{sc} (A)	V_{oc} (V)	P_m (W)	*FF*	Module efficiency (%)
0.3203	3.0079	0.8624	0.8949	32.9500
Experiment				
I_{sc} (A)	V_{oc} (V)	P_m (W)	*FF*	Module efficiency (%)
0.2679	3.0037	0.7127	0.8857	27.2303

4.5. Sensitivity analysis results

One of the biggest performance degradation reasons in the real CPV modules is the silicone sealing around or between the homogenizer exit and the solar cell. To address the effect of silicone sealing on the CPV performance a sensitivity analysis was performed.

An improved optical model was built to analyze the sensitivity of the CPV module design for two parameters. These two parameters were the silicone sealing around the base of the homogenizer and the silicone sealing between the homogenizer exit surface and the surface of the multijunction solar cell. The starting point for the design was a silicone height of 0.4 mm around the base of the homogenizer with thickness 0.3 mm. We also added silicone of thickness 0.1 mm between the exit surface of the homogenizer and the surface of the multijunction solar cell as shown in Fig. 4-15. A sensitivity analysis for short circuit current and module efficiency was conducted with the two aforementioned factors considered as the varying parameters. The first parameter (the silicone height around the homogenizer) was varied in the range from 0% to 100%, which means from 0 to 1 mm. The second parameter (the silicone thickness between the exit surface of the homogenizer and the multijunction solar cell surface) was also varied in the same manner from 0% to 100%.

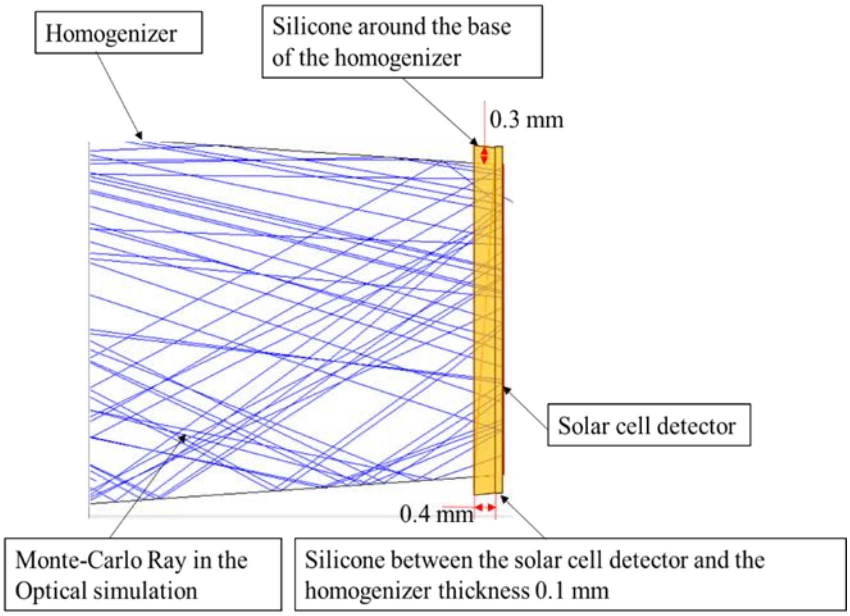

Fig. 4- 15: Basic optical structure around the base of the homogenizer used in the short circuit current and module efficiency sensitivity analysis.

The effects of the silicone height change around the base of the homogenizer on the short circuit current and module efficiency are illustrated in Fig. 4-16(a), while Fig. 4-16(b) shows the effects of the thickness of silicone between the exit surface of the homogenizer and the surface of the multijunction solar cell. To estimate which parameter has the most significant effect on the short circuit current and module efficiency, we calculated the elasticities, which are measures of the percentage change in a dependent variable (e.g. the short circuit current) divided by the percentage change in an independent variable (e.g. the parameter of silicone thickness), as follows:

$$\mathrm{e} = \frac{\%\Delta Y}{\%\Delta X} \quad (4.6)$$

The results show that for the first case, in which the change of silicone height around the base of the homogenizer was considered the parameter, for every percentage point that the silicone height increases, the short circuit current decreases by 0.0809%, and the module efficiency decreases by 0.0831%. For the second case, in which the silicone thickness between the surface of the homogenizer and the solar cell is varied, we noticed a bigger change in short circuit current, with a decrease of 0.1306% for every percentage point that the silicone thickness increases, while the module efficiency decreases by 0.1359% for every percentage point that the silicone thickness increase. The achieved module efficiency using the basic module without silicone sealing was 32.98%, which showed a 5.87% difference from the measured efficiency presented in Table 4-6.

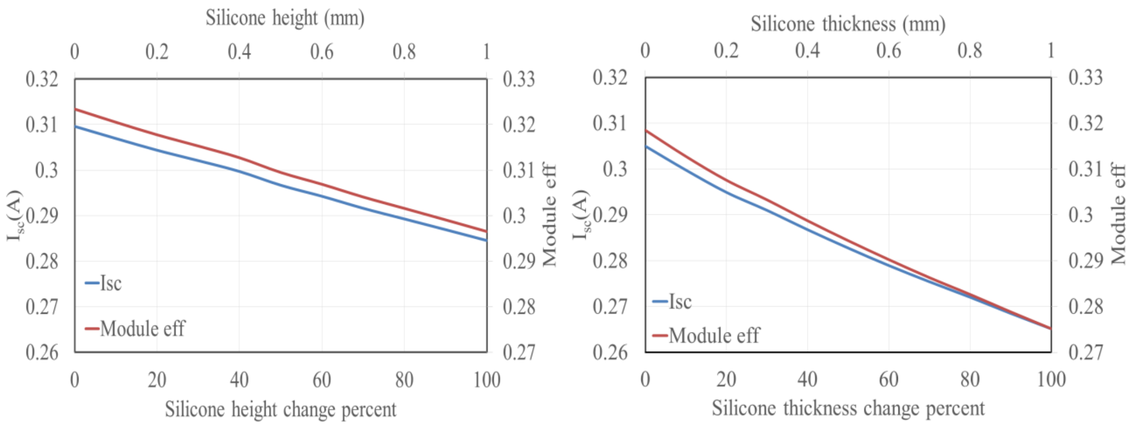

(a) (b)

Fig. 4- 16: Sensitivity analysis. (a) Sensitivity analysis with the variable parameter being the silicone height around the base of the homogenizer. (b) Sensitivity analysis with the variable parameter being the thickness of silicone between the exit surface of the homogenizer and the surface of the multijunction solar cell.

If we look to the real module closely and carefully, and after measuring the silicone sealing, we can conclude that the meniscus height is more than 1 mm, while the thickness of the silicone is 0.5 – 0.6 mm.

Analyzing these results using our obtained elasticity we get the same measured electrical results for the MCPV module, which indicates the accuracy of our sensitivity analysis.

By using the silicone sensitivity analysis, we proved that the calculated efficiency could decrease dramatically to reach values close to the measured efficiency, leading to a better agreement with experimental results by changing the two previously varied parameters (silicone height and thickness).

All CPV modules use silicone sealing, that is why it was important to clarify the effect of excessive silicone sealing use on the performance of the CPV module, either it's around or between the solar cell and the homogenizer surface. The previous sensitivity analysis proved that the main factor that we should take into careful consideration when designing and optimizing a CPV module was the thickness of silicone sealing between the exit surface of the homogenizer and the surface of the multijunction solar cell, because it will lead to significant decrease in the real module outputs compared to the designed CPV outputs especially regarding the electrical characteristics of the system.

4.6. Conclusion

The performance of a wide-acceptance-angle CPV system with 30-min intermittent tracking system was evaluated by experimental and simulation procedures in this study. Optical, electrical, and thermal simulations were conducted for the 111-sun optical concentrator system with a InGaP/InGaAs/Ge multijunction solar cell. The main strong point that we were able to prove using this system was that the performance of the CPV system was not affected by the large tracking error due to the use of low precision tracking system (30-min intermittent tracking). As a result of using this tracking system the complexity and cost of the CPV system will be reduced and the power consumption will be also decreased drastically because the system moves every 30 minute while it goes to power saving mode the rest of the time instead of moving every minute.

The achieved optical efficiency of the system was 86.9%, and the relation between the optics output and tracking error was evaluated in details. The system showed good optical performance with an acceptable homogenized irradiance distribution and wide acceptance angle of 4.5°. The experimental and simulated thermal results on February 15, 2017 at 12:30 (without tracking error) and at 12:15 (largest tracking error) showed good agreement with a small difference of less than 2%. The heating at the focal point of the lens was also evaluated and it was within the acceptable range for S-TIM2 glass and the highest calculated heat power value was 6×10^6 W/m^3. The heating at the focal point did not lead to any significant change in the optical characteristics of the lens.

An electrical characterization of the system performance showed decrease in the solar cell current matching ratio after concentration compared to the case with no concentration due to the losses and spectrum sensitivity of the optical system. The optical matching ratio was less than one, which means that the transmittance was lower for the optics in the short wavelength range (rich red spectrum) and the solar cell performance was mostly affected by the top sub-cell. The change in the electrical characteristics between the case without tracking error and with the largest tracking error was significantly small which indicated the validity of the used CPV design. Electrical evaluation also showed differences in the short circuit current and module efficiency between the experiment and simulation results due to the excessive silicone sealing around the solar cell.

A sensitivity analysis of short circuit current and module efficiency was conducted based on two main parameters. The results showed that the parameter that has the highest influence on the electrical performance was the thickness of the silicone between the multijunction solar cell surface and the homogenizer output surface.

From previous results, we can conclude two main points. First, because of the large acceptance angle compared to the highest tracking error angle of 3.65°, further optimization for the 30-min intermittent tracking can be implemented and longer intervals for the tracking system can be achieved. Second, the silicone sealing should be done with more precision and with lower thickness of silicone between the multijunction solar cell surface and the homogenizer output surface, in order to obtain better electrical and overall performance for the system.

References

1) R. Winston, J. C. Miñano, and P. Benítez, *Nonimaging Optics* (Elsevier Academic Press, London, 2004) p. 43.

2) J. M. Gordon, in *Concentrator Photovoltaics*, eds. A. L. Luque and V. M. Andreev (Springer, Heidelberg, 2007) p.113.

3) J. C. Miñano, P. Benítez, P. Zamora, M. Buljan, R. Mohedano, and A. Santamaría, Free-form optics for Fresnel-lens-based photovoltaic concentrators,Opt. Express **21**, A494 (2013).

4) B. M. Coughenour, T. Stalcup, B. Wheelwright, A. Geary, K. Hammer, and R. Angel, Dish-based high concentration PV system with Köhler optics, Opt. Express **22,** A211 (2014).

5) M. Bosi and C. Pelosi, The Potential of III-V Semiconductors as Terrestrial Photovoltaic Devices, Prog. Photovoltaics **15**, 51 (2007).

6) A. Aldossary, A. Algarue, S. Mahmoud, and R. K. AL-Dadah, Performance of Multi Junction Photovoltaic Cells with High Concentration Ratio, Energy Procedia **61**, 2258 (2014).

7) T. Takamoto, M. Kaneiwa, M. Imaizumi, and M. Yamaguchi, InGaP/GaAs-based Multijunction Solar Cells, Prog. Photovoltaics **13**, 495 (2005).

8) M. Yamaguchi, T. Takamoto, and K. Araki, Super high-efficiency multi-junction and concentrator solar cells, Sol. Energy Mater. Sol. Cells **90**, 3068 (2006).

9) J. F. Geisz, S. Kurtz, M. W. Wanlass, J. S. Ward, A. Duda, D. J. Friedman, J. M. Olson, W. E. McMahon, T. E. Moriarty, and J. T. Kiehl, High-efficiency Ga In

P/Ga As/In Ga As triple-junction solar cells grown inverted with a metamorphic bottom junction, Appl. Phys. Lett. **91**, 023502 (2007).

10) W. Guter, J. Schöne, S. P. Philipps, M. Steiner, G. Siefer, A. Wekkeli, E. Welser, E. Oliva, A. W. Bett, and F. Dimroth, Current-matched triple-junction solar cell reaching 41.1% conversion efficiency under concentrated sunlight, Appl. Phys. Lett. **94**, 223504 (2009).

11) V. Sabnis, H. Yuen, and M. Wiemer, High-efficiency multijunction solar cells employing dilute nitrides, AIP Conf. Proc. **1477**, 14 (2012).

12) K. Sasaki, T. Agui, K. Nakaido, N. Takahashi, R. Onitsuka, and T. Takamoto, Development of InGaP/GaAs/InGaAs inverted triple junction concentrator solar cells, AIP Conf. Proc. **1556**, 22 (2013).

13) F. Dimroth, M. Grave, P. Beutel, U. Fiedeler, C. Karcher, T. N. D. Tibbits, E. Oliva, G. Siefer, M. Schachtner, A. Wekkeli, A. W. Bett, R. Krause, M. Piccin, N. Blanc, C. Drazek, E. Guiot, B. Ghyselen, T. Salvetat, A. Tauzin, T. Signamarcheix, A. Dobrich, T. Hannappel, and K. Schwarzburg, Wafer bonded four-junction GaInP/GaAs//GaInAsP/GaInAs concentrator solar cells with 44.7% efficiency, Prog. Photovoltaics **22**, 277 (2014).

14) R. Swanson, in *Handbook of Photovoltaic Science,* eds. A, Luque and S. Hegedus, (John Wiley & Sons, Ltd, Chichester, 2003) p. 449.

15) K. Araki, Y. Ota, K. Lee, K. Nishioka, and M. Yamaguchi, Intermittent tracking (30 minutes interval) using a wide acceptance CPV module, AIP Conf. Proc. **1766**, 050001 (2016).

16) K. K. Chong and C. W. Wong, in *Solar Collectors and Panels, Theory and Applications,* ed. R. M. Ochieng, (Sciyo, Rijeka, 2010) p. 263.

17) N. Hayashi, A. Matsushita, D. Inoue, M. Matsumoto, T. Nagata, H. Higuchi, Y. Aya, and T. Nakagawa, Nonuniformity Sunlight-Irradiation Effect on Photovoltaic Performance of Concentrating Photovoltaic Using Microsolar Cells Without Secondary Optics , IEEE J. Photovolt. **6**, 350 (2016).

18) K. Araki, M, Kondo, H. Uozumi, and M. Yamaguchi, Experimental proof and theoretical analysis on effectiveness of passive homogenizers to 3J concentrator solar cells, Proc. 3rd WCPEC, 2003, p. 853.

19) S. R. Kurtz and M. J. O'Neill. Estimating and controlling chromatic aberration losses for two-junction, two terminal devices in refractive concentrator systems, 25th IEEE Photovoltaic Specialists Conf. (PVSC), 1996, p. 361.

20) V. Díaz, J. L. Álvarez, J. Alonso, A. Luque, and C. Mateos, Towards a technology for mass production of very high concentration flat panels, Proc. 19th EUPVSEC, 2004, p. 2086.

21) Web [http://rredc.nrel.gov/solar/spectra/am1.5/]

22) M. Theristis, E. F. Fernández, F. Almonacid, and P. Pérez-Higueras, Spectral Corrections Based on Air Mass, Aerosol Optical Depth, and Precipitable Water for CPV Performance Modeling, IEEE J. Photovolt. **6,** 1598 (2016).

23) I. Antón, M. Martínez, F. Rubio, R. Núñez, R. Herrero, C. Domínguez, M. Victoria, S. Askins, and G. Sala, Power rating of CPV systems based on spectrally corrected DNI, AIP Conf. Proc. **1477**, 331 (2012).

24) C. Domínguez, I. Antón, G. Sala, and S. Askins, Current-matching estimation for multijunction cells within a CPV module by means of component cells, Prog. Photovolt: Res. Appl. **21**, 1478 (2013).

25) G. Siefer and A.W. Bett, Analysis of temperature coefficients for III–V multijunction concentrator cells, Prog. Photovolt: Res. Appl. **22**, 515 (2014).

26) Y. Ota and K. Nishioka, Estimation of operating temperature and energy output of concentrator photovoltaic module under concentration conditions, Jap. J. Appl. Phys. **53**, 122301 (2014).

27) Y. Ota and K. Nishioka, Three-dimensional simulating of concentrator photovoltaic modules using ray trace and equivalent circuit simulators, Sol. Energy **86**, 476 (2012).

28) K. Nishioka, Y. Ota, K. Tamura, and K. Araki, Heat reduction of concentrator photovoltaic module using high radiation coating, Surf. Coat. Technol. **215**, 472 (2013).

29) M. V. Pérez, Dr. Thesis, New concepts and techniques for the development of high-efficiency concentrating photovoltaic modules, Faculty of ETS Telecommunications Engineering, The Technical University of Madrid, Madrid (2014).

Chapter 5

Summary and conclusion

5.1. Conclusion

In this thesis we presented different techniques to optimize and improve the performance of CPV systems based on two main approaches. The first approach was to improve the solar cell performance and lifetime by reducing its temperature using long-wavelength cut thin-film filter that allows only the solar irradiance in the effective spectrum range to reach it, while reflecting the spectrum which would be converted into heat and not utilized in solar cell. The study was done for different types of solar cells and the system with the best potentials was decided. We evaluated the performance of the system with thin-film filter by conducting optical, thermal, electrical and lifetime simulation to identify the performance enhancement achieved by using this technique.

The second introduced approach was a MCPV system with a wide-acceptance-angle lens that allows the use of 30-min intermittent tracking. The main benefits of using this system were the ability to use low precision tracker system which means less complex, less expensive and less power consumption by the CPV system. An experiment to measure the thermal and electrical performance was conducted, and the performance without tracking error and with the highest tracking error was evaluated to prove the feasibility of using this approach in optimizing CPV systems.

Chapter 2

Solar cells are sensitive to temperature. Increases in temperature reduce the band gap of a semiconductor, thereby affecting most of the semiconductor material parameters. In a solar cell, the parameter most affected by an increase in temperature is the open-circuit voltage. As the temperature increases, the open-circuit voltage decreases, thereby decreasing the fill factor and finally decreasing the efficiency of a solar cell. In this chapter, we introduced a new simple way to reduce the temperature of the solar cell by reflecting the solar spectrum in the long-wavelength which is not utilized in the solar cell and allowing only the effective solar spectrum (where the EQE is high) to reach the solar cell. This method was evaluated for a CPV system with two types of multijunction solar cells. The first solar cell was InGaP/InGaAs/Ge triple junction solar cell with high spectral response in the wavelength range of 400−1700 nm. The second solar cell was InGaP/GaAs/InGaAs triple junction solar cell with high spectral response in the wavelength range of 400−1100 nm. Two thin-films was developed based on the previous multijunction solar cells effective spectrum response range. The resulted thin-films were a 1700 nm cutoff thin film with a structure consisted of 65 layers and another 1100 nm cutoff thin-film filter with 91 layers. The two filters were implemented on the entry aperture of the CPV homogenizer in the optical model.

The optical and thermal performance of the system for three cases was evaluated. The first case was for the system without thin film-filter, the second case was for the system with 1700 nm cutoff thin-film filter and the third case was for the system with 1100 nm cutoff thin-film filter.

The optical simulation showed good irradiance uniformity due to the use of homogenizer in all three cases. The highest peak irradiance value was as expected for the CPV system without the thin-film filter. The optical efficiency of the system under all the solar spectrum without thin-film was 84.4%. This optical efficiency dropped to 80.29% for the system with 1700 nm cutoff thin-film filter and to 67.72% for the system with 1100 nm cutoff thin-film filter.

The thermal simulation showed that the maximum temperature for the solar cell in the system without thin-film filter reached to 118.7°C, while the temperature dropped to 114.5°C for the system with 1700 nm cutoff thin-film filter. The lowest operation temperature was achieved by the system with 1100 nm cutoff thin-film filter where it reached to 100.5°C, which mean that the temperature decreased by 18.2°C. The case with 1100 nm cutoff thin-film filter also achieved the lowest temperature distribution change on the solar cell with only 5°C difference across the surface of the solar cell.

From the previous results we were able to conclude that we can drastically decrease the solar cell temperature using thin-film filter in CPV systems. We also concluded that the system with the best thermal performance was the system, which uses InGaP/GaAs/InGaAs triple junction solar cell with 1100 nm cutoff thin-film filter. After deciding the system which fits our desired thermal performance the next step in this thesis was to evaluate the electrical performance of the system and the effects of using thin-film filter on the lifetime of the system.

Chapter 3

In this chapter we propose an improved thermal and new electrical model with a full CPV system performance and lifetime estimation using unreliability calculations for the CPV module with InGaP/GaAs/InGaAs solar cell previously introduced in the chapter 2. Further analysis for the used solar cell performance showed that the EQE had the highest response in the wavelength range of 400–1300 nm. A new thin-film was designed in this section which can transmit the solar spectrum in the range 400–1300 nm, while reflecting the rest of the spectrum.

In the new thermal model we separated the solar spectrum into three parts: one was the spectrum of 400–1300 nm, which is utilized in the solar cell we are using, the second was the ultraviolet spectrum range, and the third was the rest of the spectrum above 1300 nm. We added three heat sources to the COMSOL model, the first source for the ultraviolet spectrum and the second source for the efficient spectrum were added on the surface of the solar cell, the third source for the IR spectrum was added on the rear surface of the solar cell.

Equivalent circuit calculations were carried out using the SPICE and single unit equivalent circuit model was used to simulate the electrical performance.

A new average Arrhenius–Weibull model was introduced in this chapter taking into account the different temperatures and irradiation fluctuation throughout the year in Miyazaki City. To obtain the average Arrhenius–Weibull model, we used the calculated temperatures based on the DNI data for Miyazaki City. We obtained the DNI from the METPV database.

Optical simulation results for both the system with thin-film filter and for system without thin-film filter showed that the total optical efficiency of the model was 84.4% without the thin-film filter and 74.2% with the thin-film filter. The peak irradiance value was higher for the model without thin-film filter and the irradiance distribution uniformity on the solar cell surface decreased a little after using the thin-film filter.

The temperature of the solar cell without the thin-film filter reached to a maximum of 121°C while it was decreased to 95.7°C (with the thin film filter), representing a total decrease of 25.3°C. The highest repeated calculated temperatures for the model with thin-film filter throughout the year using the registered DNI data of Miyazaki city was in the range of 85°C to 90°C. These results demonstrated a sizeable decrease in the operation temperature range.

Electrical simulation showed that the open-circuit voltage (V_{oc}) increased due to the decrease in the cell temperature, while the current dropped a small amount due to the presence of the thin-film filter. We obtained almost the same maximum power (P_m) and the module efficiency increased in the optical model with a thin-film filter due to the sizable decrease in temperature.

The use of thin-film filter also demonstrated a big increase in the lifetime of the solar cell by more than 65 years for a failure population of 5%. This implied that the lifetime was increased to 2×10^5 h, while the operating time for a multijunction solar cell was assumed to be 8 h per day.

This chapter proved that there were big benefits of using thin-film filter in CPV systems. These benefits were mainly a sizable decrease in the temperature and drastic increase in the lifetime of the solar cell under concentration. Despite the decrease in irradiance intensity and cutting almost half of the spectrum using the thin-film filter the electrical characteristics and performance of the system was almost the same. The total module efficiency was actually improved and noticeable increase in the solar cell lifetime was obtained. Because of the small thin-film area and based on the assumption that the heat sink usually cost 5% of the CPV unit cost we expect that applying the thin-film filter will be efficient from economical point of view especially in the case of mass production.

Chapter 4

In this chapter a new approach to improve the performance and reduce the cost of CPV systems was introduced. The new approach utilized a wide acceptance angle concentrator lens that allowed us to use 30-min intermittent tracking method which did not require a special high-precision CPV tracking system. The rationale idea behind this approach is that it will allow us to reduce the cost and complexity of the system, because a large percentage of the cost and complexity of a typical CPV system comes from the expensive accurate tracking system.

In this chapter, an optical, thermal, and electrical model was designed and the concentrator performance was characterized and compared to the experimental results.

The optical system used a refractive and dielectric concentrator consisting of a primary optical lens coupled with dielectric kaleidoscope (homogenizer), S-TIM2 glass was used as an optical material. The geometric concentration ratio for this system was 111.

A thermal COMSOL Multiphysics model based on the real module was built. The multijunction solar cell was modeled as a heat source. The heat power was integrated into the heat transfer model and was calculated from the direct normal irradiance. The ambient temperature and DNI were measured throughout the day on February 15, 2017 and were used in the thermal model.

An electrical model was designed based on the used solar cell characteristics. Photocurrent distribution for each sub-cell was calculated. We used the real spectrum in the calculations, because the current–voltage (*I–V*) characteristics are significantly affected by the spectrum. Single unit equivalent circuit model was used.

The experimental procedure used two CPV modules; one for electrical measurements and the other for *I–V* characteristics measurements. A Pt100 sensor and three T-type thermocouples were used to measure the thermal performance. Temperatures, DNI and spectral characteristics of the solar irradiance were obtained using experimental equipment. The *I–V* characteristics of the CPV module were also traced by *I–V* tracer.

The optical simulation showed a total optical efficiency of 86.9% and a wide-acceptance-angle for the CPV module of 4.5º for 0.9 relative optical efficiency. The biggest tracking error for the module using 30-min intermittent tracking in the period between 12:15 and 12:45 reached to 3.65º on the *x*-axis. Results showed that the relative optical efficiency of the module even at the worst case in the morning and at noon was considerably high which means that the system optical performance was not affected by the higher tracking error angle.

Thermal simulation results for the solar cell temperature showed less than 2% difference from the experimental results. The resulted solar cell temperature at 12:30 was 28.2ºC, which means that there will be no problem with respect to the solar cell temperature in the current CPV system. The temperature distribution on the solar cell surface was almost identical at zero tracking and at the highest tracking error. An analysis of the heating in the focal point of the lens was conducted. The results proved that there were no significant changes in the lens' optical characteristics because of the low temperature at the focal point.

Electrical characteristics outputs of the solar cell showed that tracking error had more pronounced effect on the photocurrent distribution than the temperature distribution in the multijunction solar cell. Results also showed a decrease in the solar cell current matching ratio after concentration and a significantly small change between the case with zero tracking error and the highest tracking error. The *I–V* curve results showed that there werer noticeable differences in short circuit current and module efficiency between the simulation and experimental values. These differences were expected to be caused by the excessive use of silicone sealing. A sensitivity analysis for the silicon sealing in the CPV system proved that the main factor that we should take into careful consideration when designing and optimizing a CPV module was the thickness of silicone sealing between the exit surface of the homogenizer and the surface of the multijunction solar cell.

This chapter results proved that a CPV system in the medium concentration range could work with low precision tracking system, which can lead to a sizable decrease in the system complexity and cost, beside the decrease in the energy consumption because the system doesn’t need to move every minute rather move only one time every 30 minute.

5.2. Future work

The main drawback of using a thin-film filter is that it adds complexity to the CPV system design, which can be difficult to realize in the real CPV module. The previous simulation results in chapter 2 and chapter 3 showed great benefits of using such thin-film filter to reduce the temperature of the solar cell. For future work, we suggest producing the real thin-film filter and depositing it on the homogenizer entry aperture and testing the CPV system electrical and thermal performance. The thin-film can be sensitive to incident ray angle and this can be evaluated in the experimental procedure. Another suggestion for improving the total efficiency of the system with thin-film filter is to utilize the reflected spectrum in another PV solar cell receiver or in a thermal receiver, which will convert the CPV system into concentrator photovoltaic thermal system (CPVT) and result in increase in the total system efficiency.

As for the second CPV system approach with 30-min intermittent tracking, the system evaluation revealed that there are two main optimization possibilities for developing the system. The first is the possibility of using longer intermittent tracking intervals because under current tracking interval the relative optical efficiency was about 99%, while the accepted limit for the relative optical efficiency is 90%. This means that 40-min intermittent tracking could be feasible in this system. The second mean of optimization is by improving the silicone sealing. Results showed a significant decrease in real system performance because of excessive silicone sealing. This can be solved by more care for the sealing process especially for the silicone sealing between the surface of the homogenizer exit and the solar cell.

Appendix A:1700 nm cutoff thin-film filter

Illuminant: WHITE Reference wavelength (nm): 550.0
Incident medium: AIR
Substrate: BK7

Transmittance (%)

nm	Ave	nm	Ave	nm	Ave	nm	Ave	nm	Ave	nm	Ave
250.0	0.0000	312.0	0.0000	374.0	4.0207	436.0	91.6827	498.0	93.1868	560.0	93.3656
251.0	0.0000	313.0	0.0000	375.0	4.6801	437.0	91.7507	499.0	93.0642	561.0	93.5587
252.0	0.0000	314.0	0.0000	376.0	5.4166	438.0	91.7956	500.0	92.8957	562.0	93.8012
253.0	0.0000	315.0	0.0000	377.0	6.2332	439.0	91.8137	501.0	92.7040	563.0	94.0910
254.0	0.0000	316.0	0.0000	378.0	7.1326	440.0	91.8077	502.0	92.5144	564.0	94.4228
255.0	0.0000	317.0	0.0000	379.0	8.1244	441.0	91.7854	503.0	92.3525	565.0	94.7879
256.0	0.0000	318.0	0.0000	380.0	9.2290	442.0	91.7569	504.0	92.2407	566.0	95.1743
257.0	0.0000	319.0	0.0000	381.0	10.4743	443.0	91.7305	505.0	92.1953	567.0	95.5673
258.0	0.0000	320.0	0.0000	382.0	11.8859	444.0	91.7102	506.0	92.2242	568.0	95.9501
259.0	0.0000	321.0	0.0000	383.0	13.4760	445.0	91.6941	507.0	92.3265	569.0	96.3047
260.0	0.0000	322.0	0.0000	384.0	15.2390	446.0	91.6743	508.0	92.4924	570.0	96.6131
261.0	0.0000	323.0	0.0000	385.0	17.1611	447.0	91.6396	509.0	92.7044	571.0	96.8581
262.0	0.0000	324.0	0.0000	386.0	19.2401	448.0	91.5793	510.0	92.9394	572.0	97.0251
263.0	0.0000	325.0	0.0000	387.0	21.5045	449.0	91.4872	511.0	93.1715	573.0	97.1025
264.0	0.0000	326.0	0.0000	388.0	24.0159	450.0	91.3657	512.0	93.3743	574.0	97.0833
265.0	0.0000	327.0	0.0000	389.0	26.8539	451.0	91.2284	513.0	93.5251	575.0	96.9655
266.0	0.0000	328.0	0.0000	390.0	30.0911	452.0	91.0976	514.0	93.6065	576.0	96.7521
267.0	0.0000	329.0	0.0000	391.0	33.7723	453.0	91.0034	515.0	93.6092	577.0	96.4514
268.0	0.0000	330.0	0.0000	392.0	37.9084	454.0	90.9782	516.0	93.5324	578.0	96.0763
269.0	0.0000	331.0	0.0000	393.0	42.4891	455.0	91.0511	517.0	93.3837	579.0	95.6437
270.0	0.0000	332.0	0.0000	394.0	47.5090	456.0	91.2417	518.0	93.1778	580.0	95.1730
271.0	0.0000	333.0	0.0000	395.0	52.9906	457.0	91.5558	519.0	92.9342	581.0	94.6854
272.0	0.0000	334.0	0.0000	396.0	58.9891	458.0	91.9818	520.0	92.6746	582.0	94.2025
273.0	0.0000	335.0	0.0000	397.0	65.5777	459.0	92.4898	521.0	92.4205	583.0	93.7456
274.0	0.0000	336.0	0.0000	398.0	72.8263	460.0	93.0336	522.0	92.1909	584.0	93.3342
275.0	0.0000	337.0	0.0000	399.0	80.7896	461.0	93.5558	523.0	92.0004	585.0	92.9857
276.0	0.0000	338.0	0.0000	400.0	89.5132	462.0	93.9952	524.0	91.8582	586.0	92.7148
277.0	0.0000	339.0	0.0000	401.0	89.6205	463.0	94.2970	525.0	91.7679	587.0	92.5329
278.0	0.0000	340.0	0.0000	402.0	89.7165	464.0	94.4221	526.0	91.7275	588.0	92.4481
279.0	0.0000	341.0	0.0000	403.0	89.8085	465.0	94.3555	527.0	91.7302	589.0	92.4647
280.0	0.0000	342.0	0.0000	404.0	89.9005	466.0	94.1093	528.0	91.7657	590.0	92.5837
281.0	0.0000	343.0	0.0001	405.0	89.9931	467.0	93.7212	529.0	91.8217	591.0	92.8024
282.0	0.0000	344.0	0.0003	406.0	90.0846	468.0	93.2484	530.0	91.8855	592.0	93.1146
283.0	0.0000	345.0	0.0006	407.0	90.1736	469.0	92.7581	531.0	91.9453	593.0	93.5109
284.0	0.0000	346.0	0.0015	408.0	90.2598	470.0	92.3171	532.0	91.9920	594.0	93.9789
285.0	0.0000	347.0	0.0033	409.0	90.3446	471.0	91.9833	533.0	92.0197	595.0	94.5035
286.0	0.0000	348.0	0.0073	410.0	90.4300	472.0	91.7988	534.0	92.0266	596.0	95.0676
287.0	0.0000	349.0	0.0155	411.0	90.5172	473.0	91.7853	535.0	92.0145	597.0	95.6522
288.0	0.0000	350.0	0.0318	412.0	90.6054	474.0	91.9435	536.0	91.9888	598.0	96.2377
289.0	0.0000	351.0	0.0338	413.0	90.6921	475.0	92.2526	537.0	91.9570	599.0	96.8043
290.0	0.0000	352.0	0.0362	414.0	90.7741	476.0	92.6741	538.0	91.9279	600.0	97.3329
291.0	0.0000	353.0	0.0394	415.0	90.8488	477.0	93.1561	539.0	91.9105	601.0	97.7811
292.0	0.0000	354.0	0.0437	416.0	90.9162	478.0	93.6398	540.0	91.9124	602.0	98.1644
293.0	0.0000	355.0	0.0496	417.0	90.9794	479.0	94.0674	541.0	91.9390	603.0	98.4726
294.0	0.0000	356.0	0.0579	418.0	91.0435	480.0	94.3903	542.0	91.9932	604.0	98.6985
295.0	0.0000	357.0	0.0697	419.0	91.1142	481.0	94.5759	543.0	92.0744	605.0	98.8387
296.0	0.0000	358.0	0.0865	420.0	91.1953	482.0	94.6116	544.0	92.1794	606.0	98.8936
297.0	0.0000	359.0	0.1106	421.0	91.2863	483.0	94.5065	545.0	92.3023	607.0	98.8672
298.0	0.0000	360.0	0.1452	422.0	91.3818	484.0	94.2874	546.0	92.4354	608.0	98.7665
299.0	0.0000	361.0	0.1949	423.0	91.4722	485.0	93.9942	547.0	92.5702	609.0	98.6016
300.0	0.0000	362.0	0.2650	424.0	91.5459	486.0	93.6722	548.0	92.6986	610.0	98.3845
301.0	0.0000	363.0	0.3609	425.0	91.5924	487.0	93.3648	549.0	92.8137	611.0	98.1286
302.0	0.0000	364.0	0.4870	426.0	91.6058	488.0	93.1082	550.0	92.9111	612.0	97.8479
303.0	0.0000	365.0	0.6455	427.0	91.5871	489.0	92.9269	551.0	92.9540	613.0	97.5567
304.0	0.0000	366.0	0.8377	428.0	91.5443	490.0	92.8315	552.0	92.9799	614.0	97.2685
305.0	0.0000	367.0	1.0661	429.0	91.4912	491.0	92.8191	553.0	92.9925	615.0	96.9957
306.0	0.0000	368.0	1.3352	430.0	91.4440	492.0	92.8747	554.0	92.9979	616.0	96.7495
307.0	0.0000	369.0	1.6507	431.0	91.4175	493.0	92.9741	555.0	93.0040	617.0	96.5390
308.0	0.0000	370.0	2.0168	432.0	91.4214	494.0	93.0883	556.0	93.0198	618.0	96.3715
309.0	0.0000	371.0	2.4350	433.0	91.4579	495.0	93.1878	557.0	93.0551	619.0	96.2521
310.0	0.0000	372.0	2.9058	434.0	91.5219	496.0	93.2472	558.0	93.1192	620.0	96.1841
311.0	0.0000	373.0	3.4321	435.0	91.6017	497.0	93.2492	559.0	93.2205	621.0	96.1684

nm	Ave	nm	Ave	nm	Ave	nm	Ave	nm	Ave	nm	Ave
622.0	96.2040	693.0	91.5105	764.0	96.5075	835.0	96.5711	906.0	93.3803	977.0	95.1203
623.0	96.2879	694.0	91.5184	765.0	96.6894	836.0	96.6454	907.0	93.4515	978.0	94.9678
624.0	96.4157	695.0	91.5213	766.0	96.8557	837.0	96.6992	908.0	93.5238	979.0	94.8143
625.0	96.5811	696.0	91.5188	767.0	97.0044	838.0	96.7325	909.0	93.5974	980.0	94.6602
626.0	96.7767	697.0	91.5109	768.0	97.1336	839.0	96.7454	910.0	93.6725	981.0	94.5061
627.0	96.9941	698.0	91.4973	769.0	97.2415	840.0	96.7382	911.0	93.7490	982.0	94.3524
628.0	97.2241	699.0	91.4782	770.0	97.3267	841.0	96.7112	912.0	93.8271	983.0	94.1998
629.0	97.4571	700.0	91.4538	771.0	97.3878	842.0	96.6652	913.0	93.9069	984.0	94.0486
630.0	97.6833	701.0	91.4245	772.0	97.4238	843.0	96.6009	914.0	93.9885	985.0	93.8993
631.0	97.8932	702.0	91.3906	773.0	97.4338	844.0	96.5193	915.0	94.0719	986.0	93.7523
632.0	98.0780	703.0	91.3525	774.0	97.4174	845.0	96.4215	916.0	94.1573	987.0	93.6081
633.0	98.2295	704.0	91.3110	775.0	97.3743	846.0	96.3088	917.0	94.2446	988.0	93.4671
634.0	98.3410	705.0	91.2666	776.0	97.3046	847.0	96.1823	918.0	94.3340	989.0	93.3297
635.0	98.4068	706.0	91.2202	777.0	97.2088	848.0	96.0436	919.0	94.4254	990.0	93.1961
636.0	98.4230	707.0	91.1724	778.0	97.0876	849.0	95.8939	920.0	94.5189	991.0	93.0667
637.0	98.3873	708.0	91.1242	779.0	96.9421	850.0	95.7349	921.0	94.6143	992.0	92.9419
638.0	98.2989	709.0	91.0764	780.0	96.7737	851.0	95.5687	922.0	94.7117	993.0	92.8218
639.0	98.1587	710.0	91.0297	781.0	96.5839	852.0	95.3963	923.0	94.8110	994.0	92.7068
640.0	97.9693	711.0	90.9850	782.0	96.3746	853.0	95.2189	924.0	94.9120	995.0	92.5969
641.0	97.7341	712.0	90.9429	783.0	96.1480	854.0	95.0381	925.0	95.0147	996.0	92.4925
642.0	97.4582	713.0	90.9042	784.0	95.9062	855.0	94.8552	926.0	95.1187	997.0	92.3936
643.0	97.1471	714.0	90.8694	785.0	95.6518	856.0	94.6717	927.0	95.2240	998.0	92.3005
644.0	96.8070	715.0	90.8391	786.0	95.3873	857.0	94.4887	928.0	95.3304	999.0	92.2131
645.0	96.4446	716.0	90.8136	787.0	95.1153	858.0	94.3075	929.0	95.4375	1000.0	92.1316
646.0	96.0665	717.0	90.7934	788.0	94.8386	859.0	94.1293	930.0	95.5451	1001.0	92.0565
647.0	95.6793	718.0	90.7787	789.0	94.5598	860.0	93.9550	931.0	95.6528	1002.0	91.9873
648.0	95.2892	719.0	90.7697	790.0	94.2816	861.0	93.7857	932.0	95.7604	1003.0	91.9240
649.0	94.9019	720.0	90.7665	791.0	94.0068	862.0	93.6223	933.0	95.8675	1004.0	91.8665
650.0	94.5227	721.0	90.7692	792.0	93.7377	863.0	93.4654	934.0	95.9736	1005.0	91.8148
651.0	94.1564	722.0	90.7777	793.0	93.4769	864.0	93.3159	935.0	96.0784	1006.0	91.7687
652.0	93.8065	723.0	90.7919	794.0	93.2268	865.0	93.1743	936.0	96.1815	1007.0	91.7282
653.0	93.4758	724.0	90.8118	795.0	92.9895	866.0	93.0410	937.0	96.2825	1008.0	91.6932
654.0	93.1669	725.0	90.8371	796.0	92.7671	867.0	92.9166	938.0	96.3808	1009.0	91.6634
655.0	92.8812	726.0	90.8679	797.0	92.5614	868.0	92.8012	939.0	96.4761	1010.0	91.6387
656.0	92.6199	727.0	90.9039	798.0	92.3741	869.0	92.6953	940.0	96.5679	1011.0	91.6189
657.0	92.3832	728.0	90.9450	799.0	92.2067	870.0	92.5989	941.0	96.6556	1012.0	91.6038
658.0	92.1711	729.0	90.9912	800.0	92.0604	871.0	92.5120	942.0	96.7390	1013.0	91.5932
659.0	91.9830	730.0	91.0423	801.0	91.9368	872.0	92.4348	943.0	96.8174	1014.0	91.5869
660.0	91.8180	731.0	91.0984	802.0	91.8359	873.0	92.3671	944.0	96.8905	1015.0	91.5845
661.0	91.6748	732.0	91.1596	803.0	91.7585	874.0	92.3088	945.0	96.9579	1016.0	91.5858
662.0	91.5520	733.0	91.2259	804.0	91.7049	875.0	92.2598	946.0	97.0190	1017.0	91.5905
663.0	91.4480	734.0	91.2975	805.0	91.6754	876.0	92.2198	947.0	97.0736	1018.0	91.5984
664.0	91.3610	735.0	91.3747	806.0	91.6700	877.0	92.1884	948.0	97.1212	1019.0	91.6091
665.0	91.2893	736.0	91.4577	807.0	91.6885	878.0	92.1655	949.0	97.1615	1020.0	91.6224
666.0	91.2314	737.0	91.5468	808.0	91.7306	879.0	92.1506	950.0	97.1942	1021.0	91.6379
667.0	91.1854	738.0	91.6425	809.0	91.7956	880.0	92.1433	951.0	97.2190	1022.0	91.6553
668.0	91.1500	739.0	91.7451	810.0	91.8828	881.0	92.1433	952.0	97.2358	1023.0	91.6744
669.0	91.1238	740.0	91.8551	811.0	91.9913	882.0	92.1501	953.0	97.2443	1024.0	91.6948
670.0	91.1054	741.0	91.9729	812.0	92.1200	883.0	92.1633	954.0	97.2443	1025.0	91.7162
671.0	91.0939	742.0	92.0989	813.0	92.2676	884.0	92.1824	955.0	97.2357	1026.0	91.7383
672.0	91.0884	743.0	92.2335	814.0	92.4327	885.0	92.2070	956.0	97.2184	1027.0	91.7608
673.0	91.0880	744.0	92.3770	815.0	92.6138	886.0	92.2367	957.0	97.1923	1028.0	91.7834
674.0	91.0920	745.0	92.5297	816.0	92.8090	887.0	92.2710	958.0	97.1575	1029.0	91.8059
675.0	91.1001	746.0	92.6918	817.0	93.0167	888.0	92.3095	959.0	97.1140	1030.0	91.8279
676.0	91.1118	747.0	92.8633	818.0	93.2350	889.0	92.3518	960.0	97.0619	1031.0	91.8492
677.0	91.1266	748.0	93.0443	819.0	93.4617	890.0	92.3975	961.0	97.0013	1032.0	91.8695
678.0	91.1444	749.0	93.2345	820.0	93.6948	891.0	92.4462	962.0	96.9323	1033.0	91.8887
679.0	91.1648	750.0	93.4336	821.0	93.9323	892.0	92.4976	963.0	96.8552	1034.0	91.9064
680.0	91.1876	751.0	93.6352	822.0	94.1720	893.0	92.5514	964.0	96.7702	1035.0	91.9225
681.0	91.2124	752.0	93.8445	823.0	94.4116	894.0	92.6073	965.0	96.6777	1036.0	91.9367
682.0	91.2390	753.0	94.0606	824.0	94.6490	895.0	92.6651	966.0	96.5779	1037.0	91.9490
683.0	91.2670	754.0	94.2827	825.0	94.8821	896.0	92.7245	967.0	96.4711	1038.0	91.9591
684.0	91.2959	755.0	94.5096	826.0	95.1089	897.0	92.7854	968.0	96.3578	1039.0	91.9670
685.0	91.3254	756.0	94.7400	827.0	95.3272	898.0	92.8475	969.0	96.2385	1040.0	91.9724
686.0	91.3548	757.0	94.9725	828.0	95.5353	899.0	92.9108	970.0	96.1134	1041.0	91.9754
687.0	91.3837	758.0	95.2055	829.0	95.7312	900.0	92.9752	971.0	95.9832	1042.0	91.9757
688.0	91.4114	759.0	95.4372	830.0	95.9134	901.0	93.0403	972.0	95.8482	1043.0	91.9735
689.0	91.4372	760.0	95.6657	831.0	96.0803	902.0	93.1064	973.0	95.7090	1044.0	91.9685
690.0	91.4607	761.0	95.8890	832.0	96.2305	903.0	93.1734	974.0	95.5661	1045.0	91.9609
691.0	91.4811	762.0	96.1052	833.0	96.3631	904.0	93.2413	975.0	95.4200	1046.0	91.9506
692.0	91.4979	763.0	96.3121	834.0	96.4768	905.0	93.3103	976.0	95.2712	1047.0	91.9377

nm	Ave	nm	Ave	nm	Ave	nm	Ave	nm	Ave	nm	Ave
1048.0	91.9222	1119.0	95.1289	1190.0	96.6891	1261.0	92.5578	1332.0	99.6663	1403.0	91.0973
1049.0	91.9041	1120.0	95.3102	1191.0	96.5181	1262.0	92.6740	1333.0	99.6100	1404.0	91.0548
1050.0	91.8836	1121.0	95.4923	1192.0	96.3462	1263.0	92.7940	1334.0	99.5479	1405.0	91.0173
1051.0	91.8613	1122.0	95.6752	1193.0	96.1736	1264.0	92.9177	1335.0	99.4800	1406.0	90.9848
1052.0	91.8367	1123.0	95.8583	1194.0	96.0005	1265.0	93.0450	1336.0	99.4065	1407.0	90.9572
1053.0	91.8100	1124.0	96.0414	1195.0	95.8274	1266.0	93.1757	1337.0	99.3276	1408.0	90.9347
1054.0	91.7815	1125.0	96.2241	1196.0	95.6543	1267.0	93.3096	1338.0	99.2433	1409.0	90.9172
1055.0	91.7512	1126.0	96.4062	1197.0	95.4817	1268.0	93.4466	1339.0	99.1537	1410.0	90.9047
1056.0	91.7193	1127.0	96.5871	1198.0	95.3097	1269.0	93.5866	1340.0	99.0591	1411.0	90.8973
1057.0	91.6861	1128.0	96.7667	1199.0	95.1387	1270.0	93.7292	1341.0	98.9596	1412.0	90.8949
1058.0	91.6517	1129.0	96.9446	1200.0	94.9688	1271.0	93.8745	1342.0	98.8553	1413.0	90.8976
1059.0	91.6163	1130.0	97.1204	1201.0	94.8005	1272.0	94.0221	1343.0	98.7464	1414.0	90.9053
1060.0	91.5803	1131.0	97.2938	1202.0	94.6339	1273.0	94.1719	1344.0	98.6330	1415.0	90.9180
1061.0	91.5438	1132.0	97.4644	1203.0	94.4692	1274.0	94.3238	1345.0	98.5155	1416.0	90.9358
1062.0	91.5071	1133.0	97.6319	1204.0	94.3066	1275.0	94.4775	1346.0	98.3938	1417.0	90.9586
1063.0	91.4704	1134.0	97.7960	1205.0	94.1463	1276.0	94.6328	1347.0	98.2683	1418.0	90.9864
1064.0	91.4340	1135.0	97.9563	1206.0	93.9886	1277.0	94.7895	1348.0	98.1391	1419.0	91.0191
1065.0	91.3981	1136.0	98.1125	1207.0	93.8336	1278.0	94.9474	1349.0	98.0064	1420.0	91.0568
1066.0	91.3630	1137.0	98.2643	1208.0	93.6817	1279.0	95.1064	1350.0	97.8704	1421.0	91.0993
1067.0	91.3290	1138.0	98.4114	1209.0	93.5328	1280.0	95.2661	1351.0	97.7314	1422.0	91.1467
1068.0	91.2963	1139.0	98.5534	1210.0	93.3874	1281.0	95.4264	1352.0	97.5895	1423.0	91.1989
1069.0	91.2653	1140.0	98.6902	1211.0	93.2454	1282.0	95.5872	1353.0	97.4448	1424.0	91.2558
1070.0	91.2361	1141.0	98.8214	1212.0	93.1071	1283.0	95.7480	1354.0	97.2978	1425.0	91.3175
1071.0	91.2090	1142.0	98.9466	1213.0	92.9727	1284.0	95.9088	1355.0	97.1484	1426.0	91.3838
1072.0	91.1843	1143.0	99.0658	1214.0	92.8423	1285.0	96.0694	1356.0	96.9971	1427.0	91.4547
1073.0	91.1622	1144.0	99.1786	1215.0	92.7160	1286.0	96.2294	1357.0	96.8439	1428.0	91.5301
1074.0	91.1430	1145.0	99.2848	1216.0	92.5941	1287.0	96.3887	1358.0	96.6891	1429.0	91.6099
1075.0	91.1269	1146.0	99.3842	1217.0	92.4766	1288.0	96.5470	1359.0	96.5329	1430.0	91.6941
1076.0	91.1142	1147.0	99.4765	1218.0	92.3636	1289.0	96.7041	1360.0	96.3755	1431.0	91.7826
1077.0	91.1050	1148.0	99.5617	1219.0	92.2553	1290.0	96.8599	1361.0	96.2172	1432.0	91.8752
1078.0	91.0996	1149.0	99.6394	1220.0	92.1518	1291.0	97.0140	1362.0	96.0581	1433.0	91.9720
1079.0	91.0982	1150.0	99.7097	1221.0	92.0532	1292.0	97.1662	1363.0	95.8984	1434.0	92.0728
1080.0	91.1010	1151.0	99.7721	1222.0	91.9597	1293.0	97.3164	1364.0	95.7384	1435.0	92.1776
1081.0	91.1082	1152.0	99.8267	1223.0	91.8712	1294.0	97.4642	1365.0	95.5783	1436.0	92.2861
1082.0	91.1199	1153.0	99.8735	1224.0	91.7879	1295.0	97.6095	1366.0	95.4182	1437.0	92.3984
1083.0	91.1363	1154.0	99.9124	1225.0	91.7098	1296.0	97.7521	1367.0	95.2584	1438.0	92.5142
1084.0	91.1576	1155.0	99.9433	1226.0	91.6371	1297.0	97.8918	1368.0	95.0991	1439.0	92.6336
1085.0	91.1839	1156.0	99.9661	1227.0	91.5698	1298.0	98.0282	1369.0	94.9405	1440.0	92.7563
1086.0	91.2153	1157.0	99.9808	1228.0	91.5079	1299.0	98.1613	1370.0	94.7827	1441.0	92.8822
1087.0	91.2520	1158.0	99.9875	1229.0	91.4515	1300.0	98.2908	1371.0	94.6260	1442.0	93.0112
1088.0	91.2940	1159.0	99.9861	1230.0	91.4007	1301.0	98.4163	1372.0	94.4706	1443.0	93.1433
1089.0	91.3414	1160.0	99.9767	1231.0	91.3555	1302.0	98.5377	1373.0	94.3165	1444.0	93.2781
1090.0	91.3943	1161.0	99.9593	1232.0	91.3159	1303.0	98.6551	1374.0	94.1641	1445.0	93.4157
1091.0	91.4528	1162.0	99.9339	1233.0	91.2820	1304.0	98.7680	1375.0	94.0135	1446.0	93.5558
1092.0	91.5169	1163.0	99.9006	1234.0	91.2537	1305.0	98.8765	1376.0	93.8648	1447.0	93.6983
1093.0	91.5866	1164.0	99.8596	1235.0	91.2312	1306.0	98.9803	1377.0	93.7183	1448.0	93.8431
1094.0	91.6620	1165.0	99.8110	1236.0	91.2143	1307.0	99.0792	1378.0	93.5740	1449.0	93.9900
1095.0	91.7430	1166.0	99.7548	1237.0	91.2032	1308.0	99.1731	1379.0	93.4322	1450.0	94.1388
1096.0	91.8296	1167.0	99.6912	1238.0	91.1978	1309.0	99.2619	1380.0	93.2930	1451.0	94.2892
1097.0	91.9219	1168.0	99.6204	1239.0	91.1981	1310.0	99.3453	1381.0	93.1566	1452.0	94.4413
1098.0	92.0197	1169.0	99.5425	1240.0	91.2040	1311.0	99.4234	1382.0	93.0231	1453.0	94.5948
1099.0	92.1230	1170.0	99.4577	1241.0	91.2156	1312.0	99.4958	1383.0	92.8926	1454.0	94.7495
1100.0	92.2318	1171.0	99.3663	1242.0	91.2329	1313.0	99.5626	1384.0	92.7653	1455.0	94.9053
1101.0	92.3458	1172.0	99.2684	1243.0	91.2558	1314.0	99.6235	1385.0	92.6413	1456.0	95.0620
1102.0	92.4650	1173.0	99.1643	1244.0	91.2843	1315.0	99.6786	1386.0	92.5207	1457.0	95.2195
1103.0	92.5893	1174.0	99.0541	1245.0	91.3183	1316.0	99.7277	1387.0	92.4037	1458.0	95.3774
1104.0	92.7186	1175.0	98.9382	1246.0	91.3577	1317.0	99.7707	1388.0	92.2904	1459.0	95.5357
1105.0	92.8528	1176.0	98.8167	1247.0	91.4027	1318.0	99.8076	1389.0	92.1809	1460.0	95.6942
1106.0	92.9916	1177.0	98.6900	1248.0	91.4529	1319.0	99.8383	1390.0	92.0753	1461.0	95.8526
1107.0	93.1349	1178.0	98.5582	1249.0	91.5086	1320.0	99.8628	1391.0	91.9737	1462.0	96.0107
1108.0	93.2826	1179.0	98.4217	1250.0	91.5694	1321.0	99.8810	1392.0	91.8761	1463.0	96.1685
1109.0	93.4344	1180.0	98.2808	1251.0	91.6353	1322.0	99.8929	1393.0	91.7828	1464.0	96.3256
1110.0	93.5902	1181.0	98.1356	1252.0	91.7063	1323.0	99.8985	1394.0	91.6938	1465.0	96.4819
1111.0	93.7496	1182.0	97.9866	1253.0	91.7823	1324.0	99.8977	1395.0	91.6091	1466.0	96.6371
1112.0	93.9125	1183.0	97.8340	1254.0	91.8632	1325.0	99.8906	1396.0	91.5289	1467.0	96.7911
1113.0	94.0787	1184.0	97.6780	1255.0	91.9489	1326.0	99.8772	1397.0	91.4531	1468.0	96.9437
1114.0	94.2479	1185.0	97.5190	1256.0	92.0392	1327.0	99.8575	1398.0	91.3820	1469.0	97.0947
1115.0	94.4198	1186.0	97.3573	1257.0	92.1342	1328.0	99.8316	1399.0	91.3155	1470.0	97.2438
1116.0	94.5941	1187.0	97.1932	1258.0	92.2337	1329.0	99.7994	1400.0	91.2537	1471.0	97.3909
1117.0	94.7706	1188.0	97.0269	1259.0	92.3375	1330.0	99.7611	1401.0	91.1968	1472.0	97.5358
1118.0	94.9490	1189.0	96.8588	1260.0	92.4456	1331.0	99.7167	1402.0	91.1446	1473.0	97.6783

nm	Ave	nm	Ave	nm	Ave	nm	Ave	nm	Ave	nm	Ave
1474.0	97.8181	1545.0	95.3633	1616.0	91.8043	1687.0	95.8727	1758.0	39.7556	1829.0	14.0035
1475.0	97.9551	1546.0	95.1930	1617.0	91.9459	1688.0	95.4313	1759.0	39.1081	1830.0	13.8341
1476.0	98.0892	1547.0	95.0227	1618.0	92.0927	1689.0	94.9663	1760.0	38.4713	1831.0	13.6678
1477.0	98.2200	1548.0	94.8526	1619.0	92.2446	1690.0	94.4780	1761.0	37.8452	1832.0	13.5045
1478.0	98.3474	1549.0	94.6830	1620.0	92.4014	1691.0	93.9665	1762.0	37.2298	1833.0	13.3442
1479.0	98.4713	1550.0	94.5139	1621.0	92.5630	1692.0	93.4319	1763.0	36.6250	1834.0	13.1867
1480.0	98.5914	1551.0	94.3457	1622.0	92.7292	1693.0	92.8747	1764.0	36.0306	1835.0	13.0321
1481.0	98.7076	1552.0	94.1786	1623.0	92.8999	1694.0	92.2951	1765.0	35.4467	1836.0	12.8803
1482.0	98.8197	1553.0	94.0126	1624.0	93.0748	1695.0	91.6934	1766.0	34.8730	1837.0	12.7312
1483.0	98.9276	1554.0	93.8480	1625.0	93.2539	1696.0	91.0702	1767.0	34.3095	1838.0	12.5848
1484.0	99.0310	1555.0	93.6850	1626.0	93.4369	1697.0	90.4259	1768.0	33.7561	1839.0	12.4409
1485.0	99.1298	1556.0	93.5237	1627.0	93.6236	1698.0	89.7609	1769.0	33.2127	1840.0	12.2997
1486.0	99.2239	1557.0	93.3643	1628.0	93.8137	1699.0	89.0760	1770.0	32.6792	1841.0	12.1609
1487.0	99.3132	1558.0	93.2071	1629.0	94.0071	1700.0	88.3716	1771.0	32.1554	1842.0	12.0246
1488.0	99.3974	1559.0	93.0521	1630.0	94.2035	1701.0	87.6474	1772.0	31.6413	1843.0	11.8908
1489.0	99.4765	1560.0	92.8996	1631.0	94.4026	1702.0	86.9051	1773.0	31.1366	1844.0	11.7592
1490.0	99.5503	1561.0	92.7497	1632.0	94.6042	1703.0	86.1453	1774.0	30.6413	1845.0	11.6300
1491.0	99.6187	1562.0	92.6026	1633.0	94.8079	1704.0	85.3688	1775.0	30.1552	1846.0	11.5030
1492.0	99.6816	1563.0	92.4584	1634.0	95.0136	1705.0	84.5764	1776.0	29.6782	1847.0	11.3783
1493.0	99.7389	1564.0	92.3173	1635.0	95.2207	1706.0	83.7688	1777.0	29.2102	1848.0	11.2557
1494.0	99.7906	1565.0	92.1795	1636.0	95.4291	1707.0	82.9469	1778.0	28.7510	1849.0	11.1353
1495.0	99.8364	1566.0	92.0451	1637.0	95.6384	1708.0	82.1115	1779.0	28.3005	1850.0	11.0169
1496.0	99.8764	1567.0	91.9143	1638.0	95.8482	1709.0	81.2635	1780.0	27.8585	1851.0	10.9006
1497.0	99.9104	1568.0	91.7871	1639.0	96.0581	1710.0	80.4038	1781.0	27.4250	1852.0	10.7863
1498.0	99.9384	1569.0	91.6637	1640.0	96.2678	1711.0	79.5332	1782.0	26.9997	1853.0	10.6739
1499.0	99.9604	1570.0	91.5444	1641.0	96.4768	1712.0	78.6526	1783.0	26.5826	1854.0	10.5635
1500.0	99.9763	1571.0	91.4291	1642.0	96.6846	1713.0	77.7630	1784.0	26.1734	1855.0	10.4549
1501.0	99.9861	1572.0	91.3180	1643.0	96.8910	1714.0	76.8651	1785.0	25.7721	1856.0	10.3482
1502.0	99.9898	1573.0	91.2113	1644.0	97.0954	1715.0	75.9599	1786.0	25.3785	1857.0	10.2433
1503.0	99.9872	1574.0	91.1091	1645.0	97.2973	1716.0	75.0484	1787.0	24.9925	1858.0	10.1402
1504.0	99.9785	1575.0	91.0114	1646.0	97.4963	1717.0	74.1312	1788.0	24.6140	1859.0	10.0388
1505.0	99.9637	1576.0	90.9184	1647.0	97.6918	1718.0	73.2094	1789.0	24.2427	1860.0	9.9391
1506.0	99.9427	1577.0	90.8303	1648.0	97.8833	1719.0	72.2838	1790.0	23.8786	1861.0	9.8411
1507.0	99.9156	1578.0	90.7470	1649.0	98.0703	1720.0	71.3552	1791.0	23.5216	1862.0	9.7448
1508.0	99.8824	1579.0	90.6687	1650.0	98.2523	1721.0	70.4245	1792.0	23.1714	1863.0	9.6500
1509.0	99.8431	1580.0	90.5956	1651.0	98.4285	1722.0	69.4924	1793.0	22.8281	1864.0	9.5568
1510.0	99.7978	1581.0	90.5276	1652.0	98.5986	1723.0	68.5597	1794.0	22.4913	1865.0	9.4652
1511.0	99.7466	1582.0	90.4649	1653.0	98.7619	1724.0	67.6273	1795.0	22.1611	1866.0	9.3751
1512.0	99.6895	1583.0	90.4075	1654.0	98.9178	1725.0	66.6958	1796.0	21.8373	1867.0	9.2865
1513.0	99.6266	1584.0	90.3556	1655.0	99.0657	1726.0	65.7660	1797.0	21.5197	1868.0	9.1993
1514.0	99.5580	1585.0	90.3092	1656.0	99.2050	1727.0	64.8385	1798.0	21.2083	1869.0	9.1135
1515.0	99.4837	1586.0	90.2683	1657.0	99.3351	1728.0	63.9140	1799.0	20.9029	1870.0	9.0292
1516.0	99.4039	1587.0	90.2332	1658.0	99.4553	1729.0	62.9932	1800.0	20.6033	1871.0	8.9462
1517.0	99.3187	1588.0	90.2037	1659.0	99.5649	1730.0	62.0766	1801.0	20.3094	1872.0	8.8646
1518.0	99.2282	1589.0	90.1800	1660.0	99.6633	1731.0	61.1649	1802.0	20.0211	1873.0	8.7843
1519.0	99.1325	1590.0	90.1622	1661.0	99.7499	1732.0	60.2586	1803.0	19.7384	1874.0	8.7053
1520.0	99.0318	1591.0	90.1502	1662.0	99.8240	1733.0	59.3582	1804.0	19.4611	1875.0	8.6276
1521.0	98.9261	1592.0	90.1441	1663.0	99.8849	1734.0	58.4641	1805.0	19.1891	1876.0	8.5511
1522.0	98.8157	1593.0	90.1440	1664.0	99.9320	1735.0	57.5770	1806.0	18.9223	1877.0	8.4759
1523.0	98.7006	1594.0	90.1498	1665.0	99.9646	1736.0	56.6972	1807.0	18.6606	1878.0	8.4019
1524.0	98.5811	1595.0	90.1618	1666.0	99.9821	1737.0	55.8250	1808.0	18.4039	1879.0	8.3290
1525.0	98.4573	1596.0	90.1797	1667.0	99.9838	1738.0	54.9610	1809.0	18.1522	1880.0	8.2573
1526.0	98.3294	1597.0	90.2038	1668.0	99.9691	1739.0	54.1054	1810.0	17.9052	1881.0	8.1867
1527.0	98.1975	1598.0	90.2339	1669.0	99.9373	1740.0	53.2586	1811.0	17.6629	1882.0	8.1173
1528.0	98.0618	1599.0	90.2701	1670.0	99.8879	1741.0	52.4208	1812.0	17.4252	1883.0	8.0490
1529.0	97.9226	1600.0	90.3125	1671.0	99.8203	1742.0	51.5924	1813.0	17.1921	1884.0	7.9817
1530.0	97.7799	1601.0	90.3609	1672.0	99.7338	1743.0	50.7736	1814.0	16.9633	1885.0	7.9155
1531.0	97.6339	1602.0	90.4154	1673.0	99.6280	1744.0	49.9646	1815.0	16.7389	1886.0	7.8503
1532.0	97.4850	1603.0	90.4761	1674.0	99.5022	1745.0	49.1656	1816.0	16.5187	1887.0	7.7862
1533.0	97.3332	1604.0	90.5428	1675.0	99.3561	1746.0	48.3768	1817.0	16.3026	1888.0	7.7230
1534.0	97.1787	1605.0	90.6156	1676.0	99.1891	1747.0	47.5984	1818.0	16.0906	1889.0	7.6609
1535.0	97.0218	1606.0	90.6944	1677.0	99.0007	1748.0	46.8304	1819.0	15.8826	1890.0	7.5997
1536.0	96.8627	1607.0	90.7792	1678.0	98.7907	1749.0	46.0731	1820.0	15.6785	1891.0	7.5394
1537.0	96.7015	1608.0	90.8700	1679.0	98.5585	1750.0	45.3264	1821.0	15.4781	1892.0	7.4801
1538.0	96.5385	1609.0	90.9667	1680.0	98.3038	1751.0	44.5921	1822.0	15.2815	1893.0	7.4217
1539.0	96.3738	1610.0	91.0693	1681.0	98.0264	1752.0	43.8686	1823.0	15.0886	1894.0	7.3642
1540.0	96.2078	1611.0	91.1777	1682.0	97.7259	1753.0	43.1559	1824.0	14.8992	1895.0	7.3076
1541.0	96.0405	1612.0	91.2918	1683.0	97.4023	1754.0	42.4541	1825.0	14.7134	1896.0	7.2518
1542.0	95.8722	1613.0	91.4117	1684.0	97.0552	1755.0	41.7632	1826.0	14.5310	1897.0	7.1969
1543.0	95.7031	1614.0	91.5371	1685.0	96.6846	1756.0	41.0831	1827.0	14.3519	1898.0	7.1428
1544.0	95.5334	1615.0	91.6680	1686.0	96.2905	1757.0	40.4139	1828.0	14.1761	1899.0	7.0896

nm	Ave	nm	Ave	nm	Ave	nm	Ave	nm	Ave	nm	Ave
1900.0	7.0371	1971.0	4.7503	2042.0	3.9798	2113.0	3.9371	2184.0	4.4564	2255.0	5.6725
1901.0	6.9855	1972.0	4.7321	2043.0	3.9749	2114.0	3.9405	2185.0	4.4680	2256.0	5.6963
1902.0	6.9346	1973.0	4.7142	2044.0	3.9702	2115.0	3.9440	2186.0	4.4798	2257.0	5.7203
1903.0	6.8845	1974.0	4.6965	2045.0	3.9656	2116.0	3.9476	2187.0	4.4917	2258.0	5.7445
1904.0	6.8352	1975.0	4.6791	2046.0	3.9612	2117.0	3.9513	2188.0	4.5038	2259.0	5.7690
1905.0	6.7866	1976.0	4.6619	2047.0	3.9569	2118.0	3.9551	2189.0	4.5160	2260.0	5.7937
1906.0	6.7387	1977.0	4.6450	2048.0	3.9527	2119.0	3.9591	2190.0	4.5283	2261.0	5.8186
1907.0	6.6916	1978.0	4.6284	2049.0	3.9486	2120.0	3.9631	2191.0	4.5408	2262.0	5.8438
1908.0	6.6451	1979.0	4.6120	2050.0	3.9447	2121.0	3.9673	2192.0	4.5534	2263.0	5.8692
1909.0	6.5993	1980.0	4.5959	2051.0	3.9410	2122.0	3.9715	2193.0	4.5662	2264.0	5.8948
1910.0	6.5543	1981.0	4.5800	2052.0	3.9373	2123.0	3.9759	2194.0	4.5791	2265.0	5.9207
1911.0	6.5099	1982.0	4.5643	2053.0	3.9338	2124.0	3.9803	2195.0	4.5921	2266.0	5.9468
1912.0	6.4661	1983.0	4.5489	2054.0	3.9305	2125.0	3.9849	2196.0	4.6053	2267.0	5.9731
1913.0	6.4230	1984.0	4.5337	2055.0	3.9272	2126.0	3.9896	2197.0	4.6186	2268.0	5.9997
1914.0	6.3805	1985.0	4.5188	2056.0	3.9241	2127.0	3.9944	2198.0	4.6321	2269.0	6.0266
1915.0	6.3387	1986.0	4.5040	2057.0	3.9211	2128.0	3.9993	2199.0	4.6457	2270.0	6.0537
1916.0	6.2975	1987.0	4.4895	2058.0	3.9182	2129.0	4.0043	2200.0	4.6594	2271.0	6.0810
1917.0	6.2569	1988.0	4.4753	2059.0	3.9155	2130.0	4.0094	2201.0	4.6733	2272.0	6.1086
1918.0	6.2168	1989.0	4.4612	2060.0	3.9129	2131.0	4.0147	2202.0	4.6874	2273.0	6.1364
1919.0	6.1774	1990.0	4.4474	2061.0	3.9104	2132.0	4.0200	2203.0	4.7016	2274.0	6.1646
1920.0	6.1386	1991.0	4.4338	2062.0	3.9080	2133.0	4.0254	2204.0	4.7159	2275.0	6.1929
1921.0	6.1003	1992.0	4.4204	2063.0	3.9057	2134.0	4.0310	2205.0	4.7304	2276.0	6.2215
1922.0	6.0625	1993.0	4.4072	2064.0	3.9036	2135.0	4.0367	2206.0	4.7451	2277.0	6.2504
1923.0	6.0254	1994.0	4.3942	2065.0	3.9016	2136.0	4.0425	2207.0	4.7599	2278.0	6.2796
1924.0	5.9887	1995.0	4.3815	2066.0	3.8997	2137.0	4.0483	2208.0	4.7748	2279.0	6.3090
1925.0	5.9526	1996.0	4.3689	2067.0	3.8979	2138.0	4.0543	2209.0	4.7899	2280.0	6.3387
1926.0	5.9171	1997.0	4.3565	2068.0	3.8962	2139.0	4.0605	2210.0	4.8052	2281.0	6.3687
1927.0	5.8820	1998.0	4.3444	2069.0	3.8947	2140.0	4.0667	2211.0	4.8206	2282.0	6.3990
1928.0	5.8474	1999.0	4.3324	2070.0	3.8933	2141.0	4.0730	2212.0	4.8362	2283.0	6.4295
1929.0	5.8134	2000.0	4.3207	2071.0	3.8919	2142.0	4.0795	2213.0	4.8519	2284.0	6.4603
1930.0	5.7798	2001.0	4.3090	2072.0	3.8907	2143.0	4.0860	2214.0	4.8678	2285.0	6.4914
1931.0	5.7467	2002.0	4.2976	2073.0	3.8897	2144.0	4.0927	2215.0	4.8839	2286.0	6.5228
1932.0	5.7142	2003.0	4.2864	2074.0	3.8887	2145.0	4.0995	2216.0	4.9001	2287.0	6.5545
1933.0	5.6820	2004.0	4.2753	2075.0	3.8878	2146.0	4.1064	2217.0	4.9165	2288.0	6.5864
1934.0	5.6504	2005.0	4.2644	2076.0	3.8871	2147.0	4.1134	2218.0	4.9330	2289.0	6.6187
1935.0	5.6192	2006.0	4.2538	2077.0	3.8865	2148.0	4.1205	2219.0	4.9497	2290.0	6.6513
1936.0	5.5884	2007.0	4.2433	2078.0	3.8860	2149.0	4.1277	2220.0	4.9666	2291.0	6.6841
1937.0	5.5581	2008.0	4.2330	2079.0	3.8856	2150.0	4.1351	2221.0	4.9836	2292.0	6.7173
1938.0	5.5282	2009.0	4.2228	2080.0	3.8853	2151.0	4.1426	2222.0	5.0008	2293.0	6.7508
1939.0	5.4988	2010.0	4.2129	2081.0	3.8851	2152.0	4.1501	2223.0	5.0182	2294.0	6.7846
1940.0	5.4697	2011.0	4.2031	2082.0	3.8851	2153.0	4.1578	2224.0	5.0358	2295.0	6.8187
1941.0	5.4411	2012.0	4.1935	2083.0	3.8851	2154.0	4.1657	2225.0	5.0535	2296.0	6.8531
1942.0	5.4129	2013.0	4.1841	2084.0	3.8853	2155.0	4.1736	2226.0	5.0714	2297.0	6.8878
1943.0	5.3851	2014.0	4.1748	2085.0	3.8856	2156.0	4.1816	2227.0	5.0895	2298.0	6.9228
1944.0	5.3577	2015.0	4.1657	2086.0	3.8859	2157.0	4.1898	2228.0	5.1077	2299.0	6.9582
1945.0	5.3307	2016.0	4.1568	2087.0	3.8864	2158.0	4.1981	2229.0	5.1262	2300.0	6.9939
1946.0	5.3041	2017.0	4.1481	2088.0	3.8871	2159.0	4.2065	2230.0	5.1448	2301.0	7.0299
1947.0	5.2779	2018.0	4.1395	2089.0	3.8878	2160.0	4.2150	2231.0	5.1636	2302.0	7.0663
1948.0	5.2521	2019.0	4.1311	2090.0	3.8886	2161.0	4.2236	2232.0	5.1825	2303.0	7.1030
1949.0	5.2266	2020.0	4.1228	2091.0	3.8895	2162.0	4.2324	2233.0	5.2017	2304.0	7.1400
1950.0	5.2015	2021.0	4.1147	2092.0	3.8906	2163.0	4.2413	2234.0	5.2210	2305.0	7.1774
1951.0	5.1767	2022.0	4.1068	2093.0	3.8917	2164.0	4.2503	2235.0	5.2406	2306.0	7.2151
1952.0	5.1523	2023.0	4.0990	2094.0	3.8930	2165.0	4.2594	2236.0	5.2603	2307.0	7.2532
1953.0	5.1283	2024.0	4.0914	2095.0	3.8944	2166.0	4.2686	2237.0	5.2802	2308.0	7.2916
1954.0	5.1046	2025.0	4.0839	2096.0	3.8959	2167.0	4.2780	2238.0	5.3003	2309.0	7.3304
1955.0	5.0812	2026.0	4.0766	2097.0	3.8974	2168.0	4.2875	2239.0	5.3205	2310.0	7.3696
1956.0	5.0582	2027.0	4.0695	2098.0	3.8991	2169.0	4.2971	2240.0	5.3410	2311.0	7.4091
1957.0	5.0355	2028.0	4.0625	2099.0	3.9010	2170.0	4.3068	2241.0	5.3617	2312.0	7.4489
1958.0	5.0131	2029.0	4.0556	2100.0	3.9029	2171.0	4.3167	2242.0	5.3826	2313.0	7.4892
1959.0	4.9911	2030.0	4.0489	2101.0	3.9049	2172.0	4.3266	2243.0	5.4036	2314.0	7.5298
1960.0	4.9694	2031.0	4.0424	2102.0	3.9070	2173.0	4.3367	2244.0	5.4249	2315.0	7.5708
1961.0	4.9480	2032.0	4.0360	2103.0	3.9092	2174.0	4.3470	2245.0	5.4464	2316.0	7.6122
1962.0	4.9269	2033.0	4.0297	2104.0	3.9115	2175.0	4.3573	2246.0	5.4680	2317.0	7.6540
1963.0	4.9061	2034.0	4.0236	2105.0	3.9139	2176.0	4.3678	2247.0	5.4899	2318.0	7.6962
1964.0	4.8856	2035.0	4.0176	2106.0	3.9164	2177.0	4.3784	2248.0	5.5120	2319.0	7.7387
1965.0	4.8654	2036.0	4.0118	2107.0	3.9191	2178.0	4.3892	2249.0	5.5343	2320.0	7.7817
1966.0	4.8455	2037.0	4.0061	2108.0	3.9218	2179.0	4.4000	2250.0	5.5568	2321.0	7.8250
1967.0	4.8259	2038.0	4.0006	2109.0	3.9246	2180.0	4.4110	2251.0	5.5795	2322.0	7.8688
1968.0	4.8066	2039.0	3.9952	2110.0	3.9276	2181.0	4.4222	2252.0	5.6024	2323.0	7.9130
1969.0	4.7875	2040.0	3.9899	2111.0	3.9307	2182.0	4.4334	2253.0	5.6256	2324.0	7.9576
1970.0	4.7688	2041.0	3.9848	2112.0	3.9338	2183.0	4.4448	2254.0	5.6489	2325.0	8.0026

nm	Ave	nm	Ave	nm	Ave
2326.0	8.0480	2397.0	12.6849	2468.0	22.0970
2327.0	8.0939	2398.0	12.7758	2469.0	22.2845
2328.0	8.1402	2399.0	12.8677	2470.0	22.4738
2329.0	8.1869	2400.0	12.9606	2471.0	22.6652
2330.0	8.2340	2401.0	13.0543	2472.0	22.8585
2331.0	8.2817	2402.0	13.1490	2473.0	23.0538
2332.0	8.3297	2403.0	13.2446	2474.0	23.2511
2333.0	8.3782	2404.0	13.3413	2475.0	23.4504
2334.0	8.4272	2405.0	13.4388	2476.0	23.6517
2335.0	8.4766	2406.0	13.5374	2477.0	23.8551
2336.0	8.5265	2407.0	13.6370	2478.0	24.0606
2337.0	8.5769	2408.0	13.7375	2479.0	24.2682
2338.0	8.6278	2409.0	13.8391	2480.0	24.4779
2339.0	8.6791	2410.0	13.9417	2481.0	24.6898
2340.0	8.7309	2411.0	14.0454	2482.0	24.9038
2341.0	8.7832	2412.0	14.1501	2483.0	25.1199
2342.0	8.8361	2413.0	14.2558	2484.0	25.3383
2343.0	8.8894	2414.0	14.3626	2485.0	25.5589
2344.0	8.9432	2415.0	14.4706	2486.0	25.7817
2345.0	8.9975	2416.0	14.5796	2487.0	26.0067
2346.0	9.0524	2417.0	14.6897	2488.0	26.2341
2347.0	9.1078	2418.0	14.8009	2489.0	26.4637
2348.0	9.1637	2419.0	14.9133	2490.0	26.6956
2349.0	9.2201	2420.0	15.0268	2491.0	26.9299
2350.0	9.2771	2421.0	15.1415	2492.0	27.1665
2351.0	9.3346	2422.0	15.2574	2493.0	27.4055
2352.0	9.3927	2423.0	15.3744	2494.0	27.6468
2353.0	9.4513	2424.0	15.4926	2495.0	27.8906
2354.0	9.5105	2425.0	15.6121	2496.0	28.1368
2355.0	9.5703	2426.0	15.7327	2497.0	28.3854
2356.0	9.6307	2427.0	15.8546	2498.0	28.6365
2357.0	9.6916	2428.0	15.9777	2499.0	28.8901
2358.0	9.7531	2429.0	16.1021	2500.0	29.1462
2359.0	9.8152	2430.0	16.2278		
2360.0	9.8779	2431.0	16.3548		
2361.0	9.9412	2432.0	16.4831		
2362.0	10.0052	2433.0	16.6127		
2363.0	10.0697	2434.0	16.7436		
2364.0	10.1349	2435.0	16.8758		
2365.0	10.2007	2436.0	17.0095		
2366.0	10.2671	2437.0	17.1445		
2367.0	10.3342	2438.0	17.2809		
2368.0	10.4020	2439.0	17.4187		
2369.0	10.4704	2440.0	17.5579		
2370.0	10.5395	2441.0	17.6985		
2371.0	10.6092	2442.0	17.8406		
2372.0	10.6796	2443.0	17.9842		
2373.0	10.7508	2444.0	18.1292		
2374.0	10.8226	2445.0	18.2758		
2375.0	10.8951	2446.0	18.4238		
2376.0	10.9683	2447.0	18.5734		
2377.0	11.0423	2448.0	18.7245		
2378.0	11.1169	2449.0	18.8772		
2379.0	11.1924	2450.0	19.0315		
2380.0	11.2685	2451.0	19.1873		
2381.0	11.3454	2452.0	19.3448		
2382.0	11.4231	2453.0	19.5039		
2383.0	11.5015	2454.0	19.6646		
2384.0	11.5807	2455.0	19.8270		
2385.0	11.6607	2456.0	19.9910		
2386.0	11.7415	2457.0	20.1568		
2387.0	11.8231	2458.0	20.3243		
2388.0	11.9054	2459.0	20.4935		
2389.0	11.9886	2460.0	20.6644		
2390.0	12.0727	2461.0	20.8371		
2391.0	12.1576	2462.0	21.0116		
2392.0	12.2433	2463.0	21.1879		
2393.0	12.3298	2464.0	21.3660		
2394.0	12.4173	2465.0	21.5460		
2395.0	12.5056	2466.0	21.7278		
2396.0	12.5948	2467.0	21.9114		

Appendix B:1100 nm cutoff thin-film filter

Illuminant: WHITE Reference wavelength (nm): 550.0
Incident medium: AIR
Substrate: BK7

Transmittance (%)

nm	Ave	nm	Ave	nm	Ave	nm	Ave	nm	Ave	nm	Ave
250.0	0.0000	312.0	0.0000	374.0	0.8274	436.0	89.8048	498.0	90.4563	560.0	93.9835
251.0	0.0000	313.0	0.0000	375.0	0.9590	437.0	89.5965	499.0	90.2651	561.0	94.7254
252.0	0.0000	314.0	0.0000	376.0	1.1055	438.0	89.3617	500.0	89.9509	562.0	95.4884
253.0	0.0000	315.0	0.0000	377.0	1.2734	439.0	89.1853	501.0	89.5749	563.0	96.2543
254.0	0.0000	316.0	0.0000	378.0	1.4834	440.0	89.1352	502.0	89.2141	564.0	96.9996
255.0	0.0000	317.0	0.0000	379.0	1.7743	441.0	89.2408	503.0	88.9503	565.0	97.6955
256.0	0.0000	318.0	0.0000	380.0	2.2027	442.0	89.4840	504.0	88.8559	566.0	98.3093
257.0	0.0000	319.0	0.0000	381.0	2.8411	443.0	89.8063	505.0	88.9833	567.0	98.8064
258.0	0.0000	320.0	0.0000	382.0	3.7616	444.0	90.1284	506.0	89.3576	568.0	99.1531
259.0	0.0000	321.0	0.0000	383.0	4.9972	445.0	90.3779	507.0	89.9723	569.0	99.3201
260.0	0.0000	322.0	0.0000	384.0	6.4984	446.0	90.5130	508.0	90.7893	570.0	99.2859
261.0	0.0000	323.0	0.0000	385.0	8.1614	447.0	90.5352	509.0	91.7415	571.0	99.0401
262.0	0.0000	324.0	0.0000	386.0	9.9364	448.0	90.4837	510.0	92.7405	572.0	98.5849
263.0	0.0000	325.0	0.0000	387.0	11.8858	449.0	90.4169	511.0	93.6868	573.0	97.9359
264.0	0.0000	326.0	0.0000	388.0	14.1342	450.0	90.3869	512.0	94.4847	574.0	97.1213
265.0	0.0000	327.0	0.0000	389.0	16.7924	451.0	90.4196	513.0	95.0572	575.0	96.1790
266.0	0.0000	328.0	0.0000	390.0	19.9171	452.0	90.5047	514.0	95.3582	576.0	95.1537
267.0	0.0000	329.0	0.0000	391.0	23.5043	453.0	90.6013	515.0	95.3789	577.0	94.0929
268.0	0.0000	330.0	0.0000	392.0	27.5154	454.0	90.6529	516.0	95.1460	578.0	93.0433
269.0	0.0000	331.0	0.0000	393.0	31.9360	455.0	90.6101	517.0	94.7131	579.0	92.0476
270.0	0.0000	332.0	0.0000	394.0	36.8447	456.0	90.4507	518.0	94.1480	580.0	91.1424
271.0	0.0000	333.0	0.0000	395.0	42.4318	457.0	90.1911	519.0	93.5196	581.0	90.3568
272.0	0.0000	334.0	0.0000	396.0	48.9365	458.0	89.8835	520.0	92.8872	582.0	89.7110
273.0	0.0000	335.0	0.0000	397.0	56.5413	459.0	89.6007	521.0	92.2945	583.0	89.2169
274.0	0.0000	336.0	0.0000	398.0	65.3080	460.0	89.4148	522.0	91.7672	584.0	88.8777
275.0	0.0000	337.0	0.0000	399.0	75.2203	461.0	89.3772	523.0	91.3148	585.0	88.6889
276.0	0.0000	338.0	0.0000	400.0	86.3087	462.0	89.5044	524.0	90.9341	586.0	88.6385
277.0	0.0000	339.0	0.0000	401.0	86.4560	463.0	89.7734	525.0	90.6144	587.0	88.7085
278.0	0.0000	340.0	0.0000	402.0	86.5842	464.0	90.1268	526.0	90.3426	588.0	88.8758
279.0	0.0000	341.0	0.0000	403.0	86.7117	465.0	90.4862	527.0	90.1074	589.0	89.1135
280.0	0.0000	342.0	0.0000	404.0	86.8381	466.0	90.7715	528.0	89.9022	590.0	89.3924
281.0	0.0000	343.0	0.0000	405.0	86.9586	467.0	90.9216	529.0	89.7259	591.0	89.6829
282.0	0.0000	344.0	0.0000	406.0	87.0731	468.0	90.9104	530.0	89.5818	592.0	89.9567
283.0	0.0000	345.0	0.0000	407.0	87.1865	469.0	90.7526	531.0	89.4759	593.0	90.1887
284.0	0.0000	346.0	0.0000	408.0	87.3033	470.0	90.4990	532.0	89.4140	594.0	90.3586
285.0	0.0000	347.0	0.0001	409.0	87.4228	471.0	90.2222	533.0	89.3983	595.0	90.4521
286.0	0.0000	348.0	0.0003	410.0	87.5404	472.0	89.9994	534.0	89.4265	596.0	90.4616
287.0	0.0000	349.0	0.0009	411.0	87.6518	473.0	89.8963	535.0	89.4897	597.0	90.3866
288.0	0.0000	350.0	0.0030	412.0	87.7577	474.0	89.9554	536.0	89.5739	598.0	90.2332
289.0	0.0000	351.0	0.0040	413.0	87.8629	475.0	90.1906	537.0	89.6611	599.0	90.0129
290.0	0.0000	352.0	0.0054	414.0	87.9723	476.0	90.5860	538.0	89.7320	600.0	89.7418
291.0	0.0000	353.0	0.0073	415.0	88.0860	477.0	91.0992	539.0	89.7698	601.0	89.4295
292.0	0.0000	354.0	0.0097	416.0	88.1978	478.0	91.6679	540.0	89.7627	602.0	89.1061
293.0	0.0000	355.0	0.0129	417.0	88.2994	479.0	92.2183	541.0	89.7063	603.0	88.7912
294.0	0.0000	356.0	0.0168	418.0	88.3873	480.0	92.6759	542.0	89.6047	604.0	88.5038
295.0	0.0000	357.0	0.0217	419.0	88.4676	481.0	92.9763	543.0	89.4701	605.0	88.2614
296.0	0.0000	358.0	0.0278	420.0	88.5544	482.0	93.0753	544.0	89.3210	606.0	88.0800
297.0	0.0000	359.0	0.0358	421.0	88.6618	483.0	92.9562	545.0	89.1796	607.0	87.9734
298.0	0.0000	360.0	0.0464	422.0	88.7939	484.0	92.6319	546.0	89.0689	608.0	87.9532
299.0	0.0000	361.0	0.0608	423.0	88.9382	485.0	92.1434	547.0	89.0099	609.0	88.0286
300.0	0.0000	362.0	0.0798	424.0	89.0682	486.0	91.5524	548.0	89.0194	610.0	88.2067
301.0	0.0000	363.0	0.1040	425.0	89.1551	487.0	90.9321	549.0	89.1092	611.0	88.4921
302.0	0.0000	364.0	0.1332	426.0	89.1833	488.0	90.3555	550.0	89.2853	612.0	88.8870
303.0	0.0000	365.0	0.1665	427.0	89.1620	489.0	89.8865	551.0	89.4798	613.0	89.3907
304.0	0.0000	366.0	0.2038	428.0	89.1255	490.0	89.5706	552.0	89.7434	614.0	90.0001
305.0	0.0000	367.0	0.2463	429.0	89.1206	491.0	89.4297	553.0	90.0733	615.0	90.7087
306.0	0.0000	368.0	0.2965	430.0	89.1863	492.0	89.4592	554.0	90.4663	616.0	91.5064
307.0	0.0000	369.0	0.3571	431.0	89.3348	493.0	89.6286	555.0	90.9192	617.0	92.3794
308.0	0.0000	370.0	0.4293	432.0	89.5412	494.0	89.8846	556.0	91.4292	618.0	93.3098
309.0	0.0000	371.0	0.5124	433.0	89.7496	495.0	90.1597	557.0	91.9939	619.0	94.2754
310.0	0.0000	372.0	0.6057	434.0	89.8916	496.0	90.3830	558.0	92.6106	620.0	95.2495
311.0	0.0000	373.0	0.7099	435.0	89.9146	497.0	90.4942	559.0	93.2756	621.0	96.2018

nm	Ave	nm	Ave	nm	Ave	nm	Ave	nm	Ave	nm	Ave
622.0	97.0990	693.0	89.6037	764.0	90.0486	835.0	88.8893	906.0	92.8668	977.0	91.1845
623.0	97.9059	694.0	89.2710	765.0	89.6260	836.0	88.4510	907.0	93.4195	978.0	90.6062
624.0	98.5876	695.0	89.0070	766.0	89.2574	837.0	88.0788	908.0	93.9592	979.0	90.0484
625.0	99.1111	696.0	88.8315	767.0	88.9453	838.0	87.7792	909.0	94.4792	980.0	89.5161
626.0	99.4487	697.0	88.7611	768.0	88.6900	839.0	87.5575	910.0	94.9731	981.0	89.0139
627.0	99.5794	698.0	88.8090	769.0	88.4901	840.0	87.4178	911.0	95.4353	982.0	88.5460
628.0	99.4919	699.0	88.9844	770.0	88.3427	841.0	87.3630	912.0	95.8605	983.0	88.1164
629.0	99.1853	700.0	89.2924	771.0	88.2433	842.0	87.3949	913.0	96.2445	984.0	87.7284
630.0	98.6701	701.0	89.7335	772.0	88.1864	843.0	87.5141	914.0	96.5838	985.0	87.3852
631.0	97.9679	702.0	90.3040	773.0	88.1654	844.0	87.7200	915.0	96.8760	986.0	87.0896
632.0	97.1093	703.0	90.9952	774.0	88.1729	845.0	88.0112	916.0	97.1194	987.0	86.8439
633.0	96.1326	704.0	91.7938	775.0	88.2013	846.0	88.3847	917.0	97.3137	988.0	86.6500
634.0	95.0807	705.0	92.6813	776.0	88.2426	847.0	88.8367	918.0	97.4593	989.0	86.5095
635.0	93.9986	706.0	93.6346	777.0	88.2892	848.0	89.3620	919.0	97.5577	990.0	86.4237
636.0	92.9309	707.0	94.6260	778.0	88.3335	849.0	89.9543	920.0	97.6112	991.0	86.3934
637.0	91.9198	708.0	95.6241	779.0	88.3691	850.0	90.6061	921.0	97.6231	992.0	86.4191
638.0	91.0033	709.0	96.5945	780.0	88.3900	851.0	91.3047	922.0	97.5971	993.0	86.5010
639.0	90.2146	710.0	97.5012	781.0	88.3919	852.0	92.0438	923.0	97.5377	994.0	86.6388
640.0	89.5810	711.0	98.3085	782.0	88.3714	853.0	92.8124	924.0	97.4499	995.0	86.8318
641.0	89.1238	712.0	98.9827	783.0	88.3269	854.0	93.5986	925.0	97.3390	996.0	87.0792
642.0	88.8584	713.0	99.4944	784.0	88.2581	855.0	94.3896	926.0	97.2103	997.0	87.3796
643.0	88.7939	714.0	99.8204	785.0	88.1662	856.0	95.1720	927.0	97.0695	998.0	87.7311
644.0	88.9335	715.0	99.9455	786.0	88.0542	857.0	95.9318	928.0	96.9219	999.0	88.1315
645.0	89.2741	716.0	99.8635	787.0	87.9260	858.0	96.6550	929.0	96.7730	1000.0	88.5782
646.0	89.8066	717.0	99.5778	788.0	87.7868	859.0	97.3278	930.0	96.6279	1001.0	89.0658
647.0	90.5150	718.0	99.1008	789.0	87.6428	860.0	97.9368	931.0	96.4912	1002.0	89.5928
648.0	91.3770	719.0	98.4533	790.0	87.5008	861.0	98.4698	932.0	96.3674	1003.0	90.1552
649.0	92.3634	720.0	97.6627	791.0	87.3681	862.0	98.9158	933.0	96.2604	1004.0	90.7485
650.0	93.4386	721.0	96.7608	792.0	87.2521	863.0	99.2655	934.0	96.1734	1005.0	91.3677
651.0	94.5594	722.0	95.7825	793.0	87.1602	864.0	99.5119	935.0	96.1095	1006.0	92.0075
652.0	95.6812	723.0	94.7628	794.0	87.0995	865.0	99.6500	936.0	96.0707	1007.0	92.6620
653.0	96.7553	724.0	93.7362	795.0	87.0766	866.0	99.6775	937.0	96.0589	1008.0	93.3248
654.0	97.7325	725.0	92.7346	796.0	87.0974	867.0	99.5944	938.0	96.0750	1009.0	93.9893
655.0	98.5665	726.0	91.7865	797.0	87.1671	868.0	99.4036	939.0	96.1195	1010.0	94.6485
656.0	99.2172	727.0	90.9168	798.0	87.2898	869.0	99.1100	940.0	96.1922	1011.0	95.2952
657.0	99.6537	728.0	90.1459	799.0	87.4683	870.0	98.7208	941.0	96.2923	1012.0	95.9218
658.0	99.8569	729.0	89.4902	800.0	87.7046	871.0	98.2452	942.0	96.4185	1013.0	96.5210
659.0	99.8214	730.0	88.9618	801.0	87.9988	872.0	97.6937	943.0	96.5688	1014.0	97.0853
660.0	99.5554	731.0	88.5689	802.0	88.3497	873.0	97.0782	944.0	96.7405	1015.0	97.6075
661.0	99.0800	732.0	88.3160	803.0	88.7550	874.0	96.4110	945.0	96.9307	1016.0	98.0805
662.0	98.4266	733.0	88.2040	804.0	89.2113	875.0	95.7051	946.0	97.1357	1017.0	98.4980
663.0	97.6344	734.0	88.2305	805.0	89.7134	876.0	94.9733	947.0	97.3516	1018.0	98.8539
664.0	96.7468	735.0	88.3901	806.0	90.2550	877.0	94.2284	948.0	97.5738	1019.0	99.1432
665.0	95.8082	736.0	88.6742	807.0	90.8280	878.0	93.4825	949.0	97.7975	1020.0	99.3615
666.0	94.8611	737.0	89.0715	808.0	91.4235	879.0	92.7469	950.0	98.0177	1021.0	99.5055
667.0	93.9445	738.0	89.5678	809.0	92.0310	880.0	92.0322	951.0	98.2283	1022.0	99.5727
668.0	93.0915	739.0	90.1465	810.0	92.6391	881.0	91.3479	952.0	98.4247	1023.0	99.5620
669.0	92.3292	740.0	90.7886	811.0	93.2358	882.0	90.7026	953.0	98.6018	1024.0	99.4732
670.0	91.6777	741.0	91.4732	812.0	93.8083	883.0	90.1037	954.0	98.7540	1025.0	99.3074
671.0	91.1505	742.0	92.1779	813.0	94.3438	884.0	89.5577	955.0	98.8764	1026.0	99.0668
672.0	90.7545	743.0	92.8793	814.0	94.8298	885.0	89.0697	956.0	98.9642	1027.0	98.7544
673.0	90.4902	744.0	93.5540	815.0	95.2543	886.0	88.6443	957.0	99.0130	1028.0	98.3746
674.0	90.3527	745.0	94.1792	816.0	95.6063	887.0	88.2847	958.0	99.0190	1029.0	97.9323
675.0	90.3315	746.0	94.7339	817.0	95.8766	888.0	87.9934	959.0	98.9788	1030.0	97.4333
676.0	90.4117	747.0	95.1996	818.0	96.0576	889.0	87.7720	960.0	98.8900	1031.0	96.8841
677.0	90.5742	748.0	95.5610	819.0	96.1440	890.0	87.6214	961.0	98.7507	1032.0	96.2915
678.0	90.7968	749.0	95.8071	820.0	96.1331	891.0	87.5415	962.0	98.5600	1033.0	95.6629
679.0	91.0551	750.0	95.9316	821.0	96.0246	892.0	87.5317	963.0	98.3178	1034.0	95.0055
680.0	91.3237	751.0	95.9367	822.0	95.8209	893.0	87.5905	964.0	98.0247	1035.0	94.3271
681.0	91.5775	752.0	95.8261	823.0	95.5270	894.0	87.7160	965.0	97.6824	1036.0	93.6350
682.0	91.7927	753.0	95.6066	824.0	95.1501	895.0	87.9054	966.0	97.2931	1037.0	92.9367
683.0	91.9490	754.0	95.2888	825.0	94.6995	896.0	88.1553	967.0	96.8601	1038.0	92.2393
684.0	92.0303	755.0	94.8859	826.0	94.1864	897.0	88.4620	968.0	96.3872	1039.0	91.5496
685.0	92.0260	756.0	94.4133	827.0	93.6228	898.0	88.8209	969.0	95.8788	1040.0	90.8742
686.0	91.9316	757.0	93.8876	828.0	93.0221	899.0	89.2271	970.0	95.3398	1041.0	90.2190
687.0	91.7494	758.0	93.3258	829.0	92.3978	900.0	89.6750	971.0	94.7755	1042.0	89.5899
688.0	91.4875	759.0	92.7446	830.0	91.7636	901.0	90.1569	972.0	94.1917	1043.0	88.9919
689.0	91.1599	760.0	92.1600	831.0	91.1328	902.0	90.6679	973.0	93.5940	1044.0	88.4300
690.0	90.7851	761.0	91.5863	832.0	90.5185	903.0	91.2015	974.0	92.9886	1045.0	87.9083
691.0	90.3848	762.0	91.0363	833.0	89.9325	904.0	91.7506	975.0	92.3813	1046.0	87.4308
692.0	89.9829	763.0	90.5209	834.0	89.3861	905.0	92.3081	976.0	91.7780	1047.0	87.0010

nm	Ave	nm	Ave	nm	Ave	nm	Ave	nm	Ave	nm	Ave
1048.0	86.6218	1119.0	58.5966	1190.0	27.0279	1261.0	14.6144	1332.0	12.9838	1403.0	14.7256
1049.0	86.2959	1120.0	57.8086	1191.0	26.2372	1262.0	14.7566	1333.0	12.8683	1404.0	14.8669
1050.0	86.0255	1121.0	57.0767	1192.0	25.4772	1263.0	14.9021	1334.0	12.7572	1405.0	15.0095
1051.0	85.8127	1122.0	56.3999	1193.0	24.7478	1264.0	15.0503	1335.0	12.6503	1406.0	15.1534
1052.0	85.6585	1123.0	55.7774	1194.0	24.0486	1265.0	15.2011	1336.0	12.5478	1407.0	15.2984
1053.0	85.5642	1124.0	55.2081	1195.0	23.3791	1266.0	15.3538	1337.0	12.4497	1408.0	15.4443
1054.0	85.5306	1125.0	54.6907	1196.0	22.7388	1267.0	15.5080	1338.0	12.3560	1409.0	15.5908
1055.0	85.5582	1126.0	54.2242	1197.0	22.1271	1268.0	15.6633	1339.0	12.2666	1410.0	15.7379
1056.0	85.6472	1127.0	53.8073	1198.0	21.5432	1269.0	15.8190	1340.0	12.1817	1411.0	15.8852
1057.0	85.7976	1128.0	53.4385	1199.0	20.9862	1270.0	15.9746	1341.0	12.1012	1412.0	16.0326
1058.0	86.0086	1129.0	53.1167	1200.0	20.4556	1271.0	16.1295	1342.0	12.0251	1413.0	16.1798
1059.0	86.2796	1130.0	52.8402	1201.0	19.9500	1272.0	16.2830	1343.0	11.9533	1414.0	16.3266
1060.0	86.6091	1131.0	52.6077	1202.0	19.4690	1273.0	16.4346	1344.0	11.8860	1415.0	16.4727
1061.0	86.9956	1132.0	52.4175	1203.0	19.0117	1274.0	16.5835	1345.0	11.8230	1416.0	16.6180
1062.0	87.4370	1133.0	52.2681	1204.0	18.5772	1275.0	16.7290	1346.0	11.7643	1417.0	16.7622
1063.0	87.9305	1134.0	52.1577	1205.0	18.1646	1276.0	16.8705	1347.0	11.7099	1418.0	16.9050
1064.0	88.4731	1135.0	52.0844	1206.0	17.7732	1277.0	17.0072	1348.0	11.6598	1419.0	17.0462
1065.0	89.0612	1136.0	52.0465	1207.0	17.4021	1278.0	17.1385	1349.0	11.6139	1420.0	17.1855
1066.0	89.6903	1137.0	52.0417	1208.0	17.0506	1279.0	17.2636	1350.0	11.5723	1421.0	17.3227
1067.0	90.3556	1138.0	52.0678	1209.0	16.7178	1280.0	17.3818	1351.0	11.5346	1422.0	17.4576
1068.0	91.0516	1139.0	52.1225	1210.0	16.4031	1281.0	17.4924	1352.0	11.5010	1423.0	17.5900
1069.0	91.7718	1140.0	52.2031	1211.0	16.1057	1282.0	17.5949	1353.0	11.4716	1424.0	17.7195
1070.0	92.5092	1141.0	52.3068	1212.0	15.8250	1283.0	17.6885	1354.0	11.4463	1425.0	17.8460
1071.0	93.2562	1142.0	52.4306	1213.0	15.5603	1284.0	17.7728	1355.0	11.4251	1426.0	17.9692
1072.0	94.0042	1143.0	52.5712	1214.0	15.3110	1285.0	17.8471	1356.0	11.4080	1427.0	18.0890
1073.0	94.7441	1144.0	52.7250	1215.0	15.0764	1286.0	17.9110	1357.0	11.3949	1428.0	18.2051
1074.0	95.4661	1145.0	52.8882	1216.0	14.8561	1287.0	17.9640	1358.0	11.3858	1429.0	18.3173
1075.0	96.1598	1146.0	53.0566	1217.0	14.6496	1288.0	18.0059	1359.0	11.3807	1430.0	18.4256
1076.0	96.8144	1147.0	53.2260	1218.0	14.4562	1289.0	18.0363	1360.0	11.3795	1431.0	18.5296
1077.0	97.4190	1148.0	53.3916	1219.0	14.2755	1290.0	18.0550	1361.0	11.3823	1432.0	18.6293
1078.0	97.9622	1149.0	53.5484	1220.0	14.1072	1291.0	18.0619	1362.0	11.3890	1433.0	18.7245
1079.0	98.4329	1150.0	53.6915	1221.0	13.9506	1292.0	18.0569	1363.0	11.3996	1434.0	18.8150
1080.0	98.8203	1151.0	53.8147	1222.0	13.8056	1293.0	18.0400	1364.0	11.4141	1435.0	18.9009
1081.0	99.1140	1152.0	53.9134	1223.0	13.6716	1294.0	18.0114	1365.0	11.4325	1436.0	18.9820
1082.0	99.3047	1153.0	53.9822	1224.0	13.5483	1295.0	17.9713	1366.0	11.4546	1437.0	19.0581
1083.0	99.3837	1154.0	54.0156	1225.0	13.4355	1296.0	17.9198	1367.0	11.4806	1438.0	19.1294
1084.0	99.3439	1155.0	54.0082	1226.0	13.3327	1297.0	17.8572	1368.0	11.5104	1439.0	19.1957
1085.0	99.1797	1156.0	53.9549	1227.0	13.2397	1298.0	17.7841	1369.0	11.5439	1440.0	19.2569
1086.0	98.8871	1157.0	53.8508	1228.0	13.1562	1299.0	17.7008	1370.0	11.5812	1441.0	19.3132
1087.0	98.4641	1158.0	53.6915	1229.0	13.0821	1300.0	17.6078	1371.0	11.6223	1442.0	19.3645
1088.0	97.9103	1159.0	53.4730	1230.0	13.0169	1301.0	17.5058	1372.0	11.6670	1443.0	19.4109
1089.0	97.2277	1160.0	53.1923	1231.0	12.9605	1302.0	17.3953	1373.0	11.7155	1444.0	19.4523
1090.0	96.4197	1161.0	52.8466	1232.0	12.9128	1303.0	17.2769	1374.0	11.7677	1445.0	19.4889
1091.0	95.4920	1162.0	52.4343	1233.0	12.8734	1304.0	17.1512	1375.0	11.8235	1446.0	19.5207
1092.0	94.4516	1163.0	51.9546	1234.0	12.8423	1305.0	17.0188	1376.0	11.8830	1447.0	19.5479
1093.0	93.3070	1164.0	51.4076	1235.0	12.8193	1306.0	16.8804	1377.0	11.9461	1448.0	19.5705
1094.0	92.0681	1165.0	50.7943	1236.0	12.8041	1307.0	16.7368	1378.0	12.0128	1449.0	19.5886
1095.0	90.7455	1166.0	50.1168	1237.0	12.7967	1308.0	16.5884	1379.0	12.0831	1450.0	19.6024
1096.0	89.3507	1167.0	49.3778	1238.0	12.7969	1309.0	16.4361	1380.0	12.1569	1451.0	19.6120
1097.0	87.8952	1168.0	48.5810	1239.0	12.8046	1310.0	16.2804	1381.0	12.2343	1452.0	19.6175
1098.0	86.3910	1169.0	47.7309	1240.0	12.8196	1311.0	16.1219	1382.0	12.3151	1453.0	19.6191
1099.0	84.8499	1170.0	46.8325	1241.0	12.8419	1312.0	15.9613	1383.0	12.3995	1454.0	19.6170
1100.0	83.2833	1171.0	45.8912	1242.0	12.8713	1313.0	15.7992	1384.0	12.4872	1455.0	19.6115
1101.0	81.7045	1172.0	44.9129	1243.0	12.9077	1314.0	15.6360	1385.0	12.5784	1456.0	19.6026
1102.0	80.1214	1173.0	43.9038	1244.0	12.9510	1315.0	15.4724	1386.0	12.6728	1457.0	19.5905
1103.0	78.5433	1174.0	42.8700	1245.0	13.0011	1316.0	15.3088	1387.0	12.7706	1458.0	19.5755
1104.0	76.9790	1175.0	41.8177	1246.0	13.0578	1317.0	15.1457	1388.0	12.8717	1459.0	19.5577
1105.0	75.4363	1176.0	40.7529	1247.0	13.1212	1318.0	14.9835	1389.0	12.9759	1460.0	19.5373
1106.0	73.9221	1177.0	39.6814	1248.0	13.1909	1319.0	14.8227	1390.0	13.0833	1461.0	19.5145
1107.0	72.4424	1178.0	38.6086	1249.0	13.2671	1320.0	14.6635	1391.0	13.1938	1462.0	19.4895
1108.0	71.0024	1179.0	37.5396	1250.0	13.3494	1321.0	14.5064	1392.0	13.3072	1463.0	19.4626
1109.0	69.6066	1180.0	36.4790	1251.0	13.4375	1322.0	14.3516	1393.0	13.4236	1464.0	19.4338
1110.0	68.2587	1181.0	35.4310	1252.0	13.5316	1323.0	14.1995	1394.0	13.5428	1465.0	19.4034
1111.0	66.9617	1182.0	34.3993	1253.0	13.6315	1324.0	14.0503	1395.0	13.6648	1466.0	19.3715
1112.0	65.7178	1183.0	33.3872	1254.0	13.7369	1325.0	13.9042	1396.0	13.7894	1467.0	19.3384
1113.0	64.5290	1184.0	32.3974	1255.0	13.8478	1326.0	13.7615	1397.0	13.9166	1468.0	19.3042
1114.0	63.3964	1185.0	31.4321	1256.0	13.9639	1327.0	13.6222	1398.0	14.0462	1469.0	19.2691
1115.0	62.3211	1186.0	30.4934	1257.0	14.0850	1328.0	13.4867	1399.0	14.1781	1470.0	19.2332
1116.0	61.3034	1187.0	29.5826	1258.0	14.2108	1329.0	13.3549	1400.0	14.3123	1471.0	19.1968
1117.0	60.3436	1188.0	28.7010	1259.0	14.3412	1330.0	13.2271	1401.0	14.4482	1472.0	19.1600
1118.0	59.4414	1189.0	27.8492	1260.0	14.4759	1331.0	13.1034	1402.0	14.5860	1473.0	19.1229

nm	Ave	nm	Ave	nm	Ave	nm	Ave	nm	Ave	nm	Ave
1474.0	19.0857	1545.0	19.4898	1616.0	20.3315	1687.0	20.7679	1758.0	15.8501	1829.0	11.3656
1475.0	19.0485	1546.0	19.5288	1617.0	20.3267	1688.0	20.7592	1759.0	15.7513	1830.0	11.3446
1476.0	19.0115	1547.0	19.5675	1618.0	20.3223	1689.0	20.7487	1760.0	15.6531	1831.0	11.3246
1477.0	18.9748	1548.0	19.6059	1619.0	20.3183	1690.0	20.7366	1761.0	15.5554	1832.0	11.3059
1478.0	18.9385	1549.0	19.6440	1620.0	20.3146	1691.0	20.7227	1762.0	15.4583	1833.0	11.2882
1479.0	18.9027	1550.0	19.6816	1621.0	20.3114	1692.0	20.7070	1763.0	15.3619	1834.0	11.2717
1480.0	18.8676	1551.0	19.7187	1622.0	20.3086	1693.0	20.6895	1764.0	15.2662	1835.0	11.2563
1481.0	18.8332	1552.0	19.7552	1623.0	20.3064	1694.0	20.6701	1765.0	15.1712	1836.0	11.2420
1482.0	18.7997	1553.0	19.7912	1624.0	20.3046	1695.0	20.6487	1766.0	15.0769	1837.0	11.2289
1483.0	18.7671	1554.0	19.8265	1625.0	20.3033	1696.0	20.6254	1767.0	14.9835	1838.0	11.2169
1484.0	18.7356	1555.0	19.8612	1626.0	20.3025	1697.0	20.6001	1768.0	14.8909	1839.0	11.2060
1485.0	18.7051	1556.0	19.8951	1627.0	20.3023	1698.0	20.5728	1769.0	14.7991	1840.0	11.1962
1486.0	18.6758	1557.0	19.9283	1628.0	20.3027	1699.0	20.5435	1770.0	14.7083	1841.0	11.1875
1487.0	18.6478	1558.0	19.9606	1629.0	20.3036	1700.0	20.5120	1771.0	14.6183	1842.0	11.1799
1488.0	18.6211	1559.0	19.9922	1630.0	20.3051	1701.0	20.4782	1772.0	14.5293	1843.0	11.1735
1489.0	18.5958	1560.0	20.0228	1631.0	20.3072	1702.0	20.4423	1773.0	14.4413	1844.0	11.1681
1490.0	18.5719	1561.0	20.0525	1632.0	20.3099	1703.0	20.4043	1774.0	14.3543	1845.0	11.1639
1491.0	18.5495	1562.0	20.0812	1633.0	20.3131	1704.0	20.3641	1775.0	14.2683	1846.0	11.1607
1492.0	18.5286	1563.0	20.1090	1634.0	20.3170	1705.0	20.3217	1776.0	14.1833	1847.0	11.1587
1493.0	18.5093	1564.0	20.1358	1635.0	20.3215	1706.0	20.2772	1777.0	14.0994	1848.0	11.1577
1494.0	18.4916	1565.0	20.1615	1636.0	20.3266	1707.0	20.2306	1778.0	14.0165	1849.0	11.1579
1495.0	18.4755	1566.0	20.1862	1637.0	20.3323	1708.0	20.1817	1779.0	13.9348	1850.0	11.1591
1496.0	18.4611	1567.0	20.2098	1638.0	20.3385	1709.0	20.1308	1780.0	13.8541	1851.0	11.1615
1497.0	18.4483	1568.0	20.2323	1639.0	20.3454	1710.0	20.0777	1781.0	13.7746	1852.0	11.1649
1498.0	18.4372	1569.0	20.2537	1640.0	20.3528	1711.0	20.0224	1782.0	13.6963	1853.0	11.1694
1499.0	18.4279	1570.0	20.2740	1641.0	20.3608	1712.0	19.9651	1783.0	13.6190	1854.0	11.1750
1500.0	18.4203	1571.0	20.2932	1642.0	20.3694	1713.0	19.9057	1784.0	13.5430	1855.0	11.1817
1501.0	18.4143	1572.0	20.3113	1643.0	20.3785	1714.0	19.8442	1785.0	13.4681	1856.0	11.1895
1502.0	18.4100	1573.0	20.3283	1644.0	20.3881	1715.0	19.7806	1786.0	13.3944	1857.0	11.1983
1503.0	18.4075	1574.0	20.3441	1645.0	20.3982	1716.0	19.7151	1787.0	13.3219	1858.0	11.2083
1504.0	18.4067	1575.0	20.3588	1646.0	20.4088	1717.0	19.6475	1788.0	13.2506	1859.0	11.2194
1505.0	18.4076	1576.0	20.3725	1647.0	20.4198	1718.0	19.5780	1789.0	13.1806	1860.0	11.2315
1506.0	18.4102	1577.0	20.3850	1648.0	20.4313	1719.0	19.5067	1790.0	13.1117	1861.0	11.2447
1507.0	18.4145	1578.0	20.3964	1649.0	20.4432	1720.0	19.4334	1791.0	13.0441	1862.0	11.2590
1508.0	18.4205	1579.0	20.4068	1650.0	20.4555	1721.0	19.3583	1792.0	12.9776	1863.0	11.2744
1509.0	18.4282	1580.0	20.4162	1651.0	20.4680	1722.0	19.2815	1793.0	12.9125	1864.0	11.2909
1510.0	18.4375	1581.0	20.4245	1652.0	20.4808	1723.0	19.2029	1794.0	12.8485	1865.0	11.3085
1511.0	18.4484	1582.0	20.4318	1653.0	20.4939	1724.0	19.1227	1795.0	12.7858	1866.0	11.3272
1512.0	18.4609	1583.0	20.4381	1654.0	20.5072	1725.0	19.0408	1796.0	12.7243	1867.0	11.3469
1513.0	18.4750	1584.0	20.4434	1655.0	20.5208	1726.0	18.9574	1797.0	12.6641	1868.0	11.3678
1514.0	18.4907	1585.0	20.4479	1656.0	20.5345	1727.0	18.8725	1798.0	12.6051	1869.0	11.3897
1515.0	18.5078	1586.0	20.4514	1657.0	20.5484	1728.0	18.7861	1799.0	12.5474	1870.0	11.4128
1516.0	18.5264	1587.0	20.4541	1658.0	20.5623	1729.0	18.6984	1800.0	12.4909	1871.0	11.4369
1517.0	18.5465	1588.0	20.4559	1659.0	20.5763	1730.0	18.6093	1801.0	12.4351	1872.0	11.4622
1518.0	18.5679	1589.0	20.4569	1660.0	20.5903	1731.0	18.5190	1802.0	12.3805	1873.0	11.4885
1519.0	18.5907	1590.0	20.4572	1661.0	20.6042	1732.0	18.4275	1803.0	12.3272	1874.0	11.5159
1520.0	18.6148	1591.0	20.4568	1662.0	20.6180	1733.0	18.3348	1804.0	12.2751	1875.0	11.5445
1521.0	18.6402	1592.0	20.4557	1663.0	20.6317	1734.0	18.2411	1805.0	12.2242	1876.0	11.5741
1522.0	18.6668	1593.0	20.4539	1664.0	20.6452	1735.0	18.1464	1806.0	12.1746	1877.0	11.6049
1523.0	18.6945	1594.0	20.4515	1665.0	20.6585	1736.0	18.0508	1807.0	12.1262	1878.0	11.6368
1524.0	18.7234	1595.0	20.4486	1666.0	20.6714	1737.0	17.9544	1808.0	12.0790	1879.0	11.6697
1525.0	18.7534	1596.0	20.4452	1667.0	20.6840	1738.0	17.8571	1809.0	12.0330	1880.0	11.7038
1526.0	18.7844	1597.0	20.4413	1668.0	20.6961	1739.0	17.7591	1810.0	11.9883	1881.0	11.7390
1527.0	18.8163	1598.0	20.4369	1669.0	20.7078	1740.0	17.6605	1811.0	11.9448	1882.0	11.7753
1528.0	18.8492	1599.0	20.4322	1670.0	20.7189	1741.0	17.5613	1812.0	11.9025	1883.0	11.8128
1529.0	18.8829	1600.0	20.4271	1671.0	20.7295	1742.0	17.4616	1813.0	11.8614	1884.0	11.8513
1530.0	18.9174	1601.0	20.4216	1672.0	20.7393	1743.0	17.3614	1814.0	11.8215	1885.0	11.8910
1531.0	18.9527	1602.0	20.4159	1673.0	20.7485	1744.0	17.2609	1815.0	11.7828	1886.0	11.9318
1532.0	18.9886	1603.0	20.4099	1674.0	20.7569	1745.0	17.1600	1816.0	11.7453	1887.0	11.9738
1533.0	19.0252	1604.0	20.4038	1675.0	20.7645	1746.0	17.0589	1817.0	11.7091	1888.0	12.0169
1534.0	19.0623	1605.0	20.3975	1676.0	20.7712	1747.0	16.9576	1818.0	11.6740	1889.0	12.0611
1535.0	19.0999	1606.0	20.3911	1677.0	20.7769	1748.0	16.8562	1819.0	11.6401	1890.0	12.1064
1536.0	19.1380	1607.0	20.3847	1678.0	20.7816	1749.0	16.7547	1820.0	11.6074	1891.0	12.1529
1537.0	19.1764	1608.0	20.3783	1679.0	20.7852	1750.0	16.6532	1821.0	11.5758	1892.0	12.2005
1538.0	19.2152	1609.0	20.3719	1680.0	20.7876	1751.0	16.5520	1822.0	11.5455	1893.0	12.2493
1539.0	19.2542	1610.0	20.3656	1681.0	20.7889	1752.0	16.4509	1823.0	11.5163	1894.0	12.2992
1540.0	19.2933	1611.0	20.3595	1682.0	20.7889	1753.0	16.3501	1824.0	11.4883	1895.0	12.3502
1541.0	19.3326	1612.0	20.3534	1683.0	20.7876	1754.0	16.2494	1825.0	11.4614	1896.0	12.4024
1542.0	19.3720	1613.0	20.3476	1684.0	20.7849	1755.0	16.1490	1826.0	11.4358	1897.0	12.4558
1543.0	19.4113	1614.0	20.3420	1685.0	20.7808	1756.0	16.0490	1827.0	11.4112	1898.0	12.5103
1544.0	19.4506	1615.0	20.3366	1686.0	20.7751	1757.0	15.9493	1828.0	11.3879	1899.0	12.5660

nm	Ave	nm	Ave	nm	Ave	nm	Ave	nm	Ave	nm	Ave
1900.0	12.6228	1971.0	19.2711	2042.0	24.1092	2113.0	21.9257	2184.0	21.1081	2255.0	22.7933
1901.0	12.6808	1972.0	19.3858	2043.0	24.1081	2114.0	21.8928	2185.0	21.1187	2256.0	22.8239
1902.0	12.7399	1973.0	19.5002	2044.0	24.1054	2115.0	21.8604	2186.0	21.1298	2257.0	22.8546
1903.0	12.8002	1974.0	19.6143	2045.0	24.1008	2116.0	21.8285	2187.0	21.1414	2258.0	22.8852
1904.0	12.8617	1975.0	19.7280	2046.0	24.0946	2117.0	21.7971	2188.0	21.1536	2259.0	22.9158
1905.0	12.9243	1976.0	19.8414	2047.0	24.0868	2118.0	21.7662	2189.0	21.1663	2260.0	22.9464
1906.0	12.9881	1977.0	19.9542	2048.0	24.0773	2119.0	21.7359	2190.0	21.1795	2261.0	22.9769
1907.0	13.0530	1978.0	20.0665	2049.0	24.0663	2120.0	21.7062	2191.0	21.1932	2262.0	23.0074
1908.0	13.1192	1979.0	20.1782	2050.0	24.0537	2121.0	21.6770	2192.0	21.2074	2263.0	23.0378
1909.0	13.1864	1980.0	20.2893	2051.0	24.0398	2122.0	21.6484	2193.0	21.2221	2264.0	23.0682
1910.0	13.2549	1981.0	20.3997	2052.0	24.0245	2123.0	21.6203	2194.0	21.2373	2265.0	23.0985
1911.0	13.3245	1982.0	20.5094	2053.0	24.0077	2124.0	21.5929	2195.0	21.2529	2266.0	23.1287
1912.0	13.3953	1983.0	20.6183	2054.0	23.9896	2125.0	21.5660	2196.0	21.2691	2267.0	23.1589
1913.0	13.4672	1984.0	20.7263	2055.0	23.9702	2126.0	21.5397	2197.0	21.2857	2268.0	23.1890
1914.0	13.5403	1985.0	20.8334	2056.0	23.9495	2127.0	21.5141	2198.0	21.3027	2269.0	23.2189
1915.0	13.6145	1986.0	20.9395	2057.0	23.9276	2128.0	21.4890	2199.0	21.3202	2270.0	23.2488
1916.0	13.6899	1987.0	21.0446	2058.0	23.9044	2129.0	21.4646	2200.0	21.3382	2271.0	23.2786
1917.0	13.7665	1988.0	21.1486	2059.0	23.8802	2130.0	21.4408	2201.0	21.3566	2272.0	23.3082
1918.0	13.8442	1989.0	21.2515	2060.0	23.8548	2131.0	21.4176	2202.0	21.3754	2273.0	23.3377
1919.0	13.9230	1990.0	21.3532	2061.0	23.8283	2132.0	21.3950	2203.0	21.3947	2274.0	23.3671
1920.0	14.0030	1991.0	21.4537	2062.0	23.8009	2133.0	21.3731	2204.0	21.4144	2275.0	23.3964
1921.0	14.0841	1992.0	21.5529	2063.0	23.7724	2134.0	21.3518	2205.0	21.4345	2276.0	23.4255
1922.0	14.1664	1993.0	21.6507	2064.0	23.7431	2135.0	21.3311	2206.0	21.4550	2277.0	23.4545
1923.0	14.2497	1994.0	21.7472	2065.0	23.7128	2136.0	21.3111	2207.0	21.4759	2278.0	23.4833
1924.0	14.3342	1995.0	21.8422	2066.0	23.6817	2137.0	21.2918	2208.0	21.4972	2279.0	23.5120
1925.0	14.4198	1996.0	21.9357	2067.0	23.6498	2138.0	21.2730	2209.0	21.5189	2280.0	23.5405
1926.0	14.5065	1997.0	22.0277	2068.0	23.6172	2139.0	21.2550	2210.0	21.5409	2281.0	23.5689
1927.0	14.5943	1998.0	22.1181	2069.0	23.5838	2140.0	21.2376	2211.0	21.5633	2282.0	23.5970
1928.0	14.6832	1999.0	22.2069	2070.0	23.5497	2141.0	21.2208	2212.0	21.5861	2283.0	23.6250
1929.0	14.7732	2000.0	22.2939	2071.0	23.5151	2142.0	21.2047	2213.0	21.6093	2284.0	23.6528
1930.0	14.8642	2001.0	22.3792	2072.0	23.4798	2143.0	21.1893	2214.0	21.6327	2285.0	23.6804
1931.0	14.9563	2002.0	22.4626	2073.0	23.4439	2144.0	21.1745	2215.0	21.6566	2286.0	23.7079
1932.0	15.0494	2003.0	22.5443	2074.0	23.4076	2145.0	21.1604	2216.0	21.6807	2287.0	23.7351
1933.0	15.1436	2004.0	22.6241	2075.0	23.3707	2146.0	21.1469	2217.0	21.7052	2288.0	23.7621
1934.0	15.2388	2005.0	22.7021	2076.0	23.3334	2147.0	21.1341	2218.0	21.7300	2289.0	23.7889
1935.0	15.3350	2006.0	22.7781	2077.0	23.2958	2148.0	21.1220	2219.0	21.7551	2290.0	23.8155
1936.0	15.4321	2007.0	22.8522	2078.0	23.2577	2149.0	21.1105	2220.0	21.7804	2291.0	23.8419
1937.0	15.5303	2008.0	22.9243	2079.0	23.2193	2150.0	21.0997	2221.0	21.8061	2292.0	23.8681
1938.0	15.6294	2009.0	22.9944	2080.0	23.1806	2151.0	21.0895	2222.0	21.8321	2293.0	23.8940
1939.0	15.7295	2010.0	23.0624	2081.0	23.1417	2152.0	21.0800	2223.0	21.8583	2294.0	23.9198
1940.0	15.8304	2011.0	23.1284	2082.0	23.1025	2153.0	21.0712	2224.0	21.8848	2295.0	23.9453
1941.0	15.9323	2012.0	23.1923	2083.0	23.0632	2154.0	21.0630	2225.0	21.9116	2296.0	23.9705
1942.0	16.0351	2013.0	23.2541	2084.0	23.0236	2155.0	21.0554	2226.0	21.9386	2297.0	23.9956
1943.0	16.1387	2014.0	23.3138	2085.0	22.9840	2156.0	21.0485	2227.0	21.9659	2298.0	24.0203
1944.0	16.2432	2015.0	23.3713	2086.0	22.9442	2157.0	21.0423	2228.0	21.9934	2299.0	24.0449
1945.0	16.3485	2016.0	23.4266	2087.0	22.9044	2158.0	21.0367	2229.0	22.0211	2300.0	24.0692
1946.0	16.4545	2017.0	23.4798	2088.0	22.8646	2159.0	21.0317	2230.0	22.0490	2301.0	24.0931
1947.0	16.5614	2018.0	23.5308	2089.0	22.8247	2160.0	21.0274	2231.0	22.0771	2302.0	24.1168
1948.0	16.6690	2019.0	23.5796	2090.0	22.7848	2161.0	21.0237	2232.0	22.1055	2303.0	24.1402
1949.0	16.7773	2020.0	23.6263	2091.0	22.7450	2162.0	21.0207	2233.0	22.1340	2304.0	24.1634
1950.0	16.8862	2021.0	23.6707	2092.0	22.7053	2163.0	21.0183	2234.0	22.1627	2305.0	24.1863
1951.0	16.9959	2022.0	23.7129	2093.0	22.6657	2164.0	21.0166	2235.0	22.1916	2306.0	24.2090
1952.0	17.1061	2023.0	23.7529	2094.0	22.6262	2165.0	21.0154	2236.0	22.2207	2307.0	24.2314
1953.0	17.2170	2024.0	23.7907	2095.0	22.5868	2166.0	21.0149	2237.0	22.2499	2308.0	24.2535
1954.0	17.3284	2025.0	23.8263	2096.0	22.5476	2167.0	21.0150	2238.0	22.2793	2309.0	24.2754
1955.0	17.4404	2026.0	23.8597	2097.0	22.5086	2168.0	21.0157	2239.0	22.3088	2310.0	24.2971
1956.0	17.5528	2027.0	23.8909	2098.0	22.4699	2169.0	21.0171	2240.0	22.3384	2311.0	24.3185
1957.0	17.6657	2028.0	23.9200	2099.0	22.4313	2170.0	21.0190	2241.0	22.3682	2312.0	24.3396
1958.0	17.7790	2029.0	23.9469	2100.0	22.3931	2171.0	21.0216	2242.0	22.3980	2313.0	24.3604
1959.0	17.8927	2030.0	23.9717	2101.0	22.3549	2172.0	21.0248	2243.0	22.4280	2314.0	24.3811
1960.0	18.0067	2031.0	23.9943	2102.0	22.3171	2173.0	21.0285	2244.0	22.4581	2315.0	24.4014
1961.0	18.1210	2032.0	24.0148	2103.0	22.2795	2174.0	21.0329	2245.0	22.4883	2316.0	24.4215
1962.0	18.2356	2033.0	24.0332	2104.0	22.2424	2175.0	21.0378	2246.0	22.5186	2317.0	24.4413
1963.0	18.3504	2034.0	24.0496	2105.0	22.2055	2176.0	21.0434	2247.0	22.5489	2318.0	24.4609
1964.0	18.4654	2035.0	24.0639	2106.0	22.1691	2177.0	21.0495	2248.0	22.5793	2319.0	24.4802
1965.0	18.5805	2036.0	24.0762	2107.0	22.1330	2178.0	21.0562	2249.0	22.6098	2320.0	24.4993
1966.0	18.6957	2037.0	24.0865	2108.0	22.0974	2179.0	21.0634	2250.0	22.6403	2321.0	24.5181
1967.0	18.8109	2038.0	24.0948	2109.0	22.0621	2180.0	21.0712	2251.0	22.6708	2322.0	24.5367
1968.0	18.9261	2039.0	24.1012	2110.0	22.0273	2181.0	21.0796	2252.0	22.7014	2323.0	24.5550
1969.0	19.0412	2040.0	24.1057	2111.0	21.9930	2182.0	21.0886	2253.0	22.7320	2324.0	24.5731
1970.0	19.1563	2041.0	24.1084	2112.0	21.9591	2183.0	21.0981	2254.0	22.7627	2325.0	24.5910

TFCalc

nm	Ave	nm	Ave	nm	Ave
2326.0	24.6086	2397.0	25.5320	2468.0	27.4434
2327.0	24.6259	2398.0	25.5460	2469.0	27.4897
2328.0	24.6430	2399.0	25.5601	2470.0	27.5366
2329.0	24.6599	2400.0	25.5745	2471.0	27.5843
2330.0	24.6766	2401.0	25.5891	2472.0	27.6327
2331.0	24.6930	2402.0	25.6039	2473.0	27.6818
2332.0	24.7092	2403.0	25.6190	2474.0	27.7316
2333.0	24.7252	2404.0	25.6343	2475.0	27.7822
2334.0	24.7410	2405.0	25.6498	2476.0	27.8335
2335.0	24.7565	2406.0	25.6656	2477.0	27.8856
2336.0	24.7719	2407.0	25.6816	2478.0	27.9384
2337.0	24.7870	2408.0	25.6980	2479.0	27.9920
2338.0	24.8019	2409.0	25.7146	2480.0	28.0464
2339.0	24.8167	2410.0	25.7315	2481.0	28.1015
2340.0	24.8312	2411.0	25.7486	2482.0	28.1574
2341.0	24.8456	2412.0	25.7661	2483.0	28.2142
2342.0	24.8597	2413.0	25.7839	2484.0	28.2717
2343.0	24.8737	2414.0	25.8020	2485.0	28.3301
2344.0	24.8875	2415.0	25.8204	2486.0	28.3892
2345.0	24.9012	2416.0	25.8392	2487.0	28.4492
2346.0	24.9147	2417.0	25.8583	2488.0	28.5100
2347.0	24.9280	2418.0	25.8777	2489.0	28.5716
2348.0	24.9412	2419.0	25.8975	2490.0	28.6341
2349.0	24.9542	2420.0	25.9176	2491.0	28.6975
2350.0	24.9671	2421.0	25.9381	2492.0	28.7617
2351.0	24.9798	2422.0	25.9590	2493.0	28.8268
2352.0	24.9924	2423.0	25.9803	2494.0	28.8927
2353.0	25.0049	2424.0	26.0019	2495.0	28.9595
2354.0	25.0173	2425.0	26.0240	2496.0	29.0272
2355.0	25.0295	2426.0	26.0464	2497.0	29.0958
2356.0	25.0417	2427.0	26.0693	2498.0	29.1654
2357.0	25.0537	2428.0	26.0925	2499.0	29.2358
2358.0	25.0657	2429.0	26.1162	2500.0	29.3071
2359.0	25.0775	2430.0	26.1403		
2360.0	25.0893	2431.0	26.1649		
2361.0	25.1010	2432.0	26.1899		
2362.0	25.1127	2433.0	26.2153		
2363.0	25.1242	2434.0	26.2412		
2364.0	25.1358	2435.0	26.2676		
2365.0	25.1472	2436.0	26.2944		
2366.0	25.1587	2437.0	26.3218		
2367.0	25.1701	2438.0	26.3496		
2368.0	25.1814	2439.0	26.3779		
2369.0	25.1928	2440.0	26.4067		
2370.0	25.2041	2441.0	26.4360		
2371.0	25.2155	2442.0	26.4658		
2372.0	25.2268	2443.0	26.4961		
2373.0	25.2381	2444.0	26.5270		
2374.0	25.2495	2445.0	26.5584		
2375.0	25.2609	2446.0	26.5903		
2376.0	25.2723	2447.0	26.6228		
2377.0	25.2837	2448.0	26.6558		
2378.0	25.2952	2449.0	26.6894		
2379.0	25.3068	2450.0	26.7236		
2380.0	25.3184	2451.0	26.7583		
2381.0	25.3300	2452.0	26.7937		
2382.0	25.3418	2453.0	26.8296		
2383.0	25.3536	2454.0	26.8661		
2384.0	25.3655	2455.0	26.9032		
2385.0	25.3775	2456.0	26.9409		
2386.0	25.3897	2457.0	26.9792		
2387.0	25.4019	2458.0	27.0182		
2388.0	25.4142	2459.0	27.0578		
2389.0	25.4267	2460.0	27.0980		
2390.0	25.4393	2461.0	27.1389		
2391.0	25.4521	2462.0	27.1804		
2392.0	25.4650	2463.0	27.2225		
2393.0	25.4780	2464.0	27.2654		
2394.0	25.4913	2465.0	27.3089		
2395.0	25.5047	2466.0	27.3530		
2396.0	25.5182	2467.0	27.3979		

Appendix C:1300 nm cutoff thin-film filter

Illuminant: WHITE Reference wavelength (nm): 550.0
Incident medium: AIR
Substrate: BK7

Transmittance (%)

nm	Ave	nm	Ave	nm	Ave	nm	Ave	nm	Ave	nm	Ave
250.0	0.0000	312.0	0.0000	374.0	0.7424	436.0	89.5416	498.0	95.3623	560.0	90.2445
251.0	0.0000	313.0	0.0000	375.0	0.9957	437.0	89.3847	499.0	95.2532	561.0	90.1394
252.0	0.0000	314.0	0.0000	376.0	1.3003	438.0	89.2261	500.0	94.8859	562.0	90.0266
253.0	0.0000	315.0	0.0000	377.0	1.6490	439.0	89.1345	501.0	94.3513	563.0	89.9253
254.0	0.0000	316.0	0.0000	378.0	2.0350	440.0	89.1651	502.0	93.7582	564.0	89.8556
255.0	0.0000	317.0	0.0000	379.0	2.4472	441.0	89.3395	503.0	93.2172	565.0	89.8359
256.0	0.0000	318.0	0.0000	380.0	2.8653	442.0	89.6350	504.0	92.8221	566.0	89.8808
257.0	0.0000	319.0	0.0000	381.0	3.2701	443.0	89.9872	505.0	92.6381	567.0	89.9989
258.0	0.0000	320.0	0.0000	382.0	3.6654	444.0	90.3062	506.0	92.6944	568.0	90.1917
259.0	0.0000	321.0	0.0000	383.0	4.0924	445.0	90.5040	507.0	92.9822	569.0	90.4524
260.0	0.0000	322.0	0.0000	384.0	4.6254	446.0	90.5255	508.0	93.4558	570.0	90.7656
261.0	0.0000	323.0	0.0000	385.0	5.3628	447.0	90.3696	509.0	94.0383	571.0	91.1087
262.0	0.0000	324.0	0.0000	386.0	6.4225	448.0	90.0934	510.0	94.6314	572.0	91.4524
263.0	0.0000	325.0	0.0000	387.0	7.9401	449.0	89.7956	511.0	95.1290	573.0	91.7641
264.0	0.0000	326.0	0.0000	388.0	10.0520	450.0	89.5861	512.0	95.4349	574.0	92.0102
265.0	0.0000	327.0	0.0000	389.0	12.8487	451.0	89.5541	513.0	95.4801	575.0	92.1607
266.0	0.0000	328.0	0.0000	390.0	16.3151	452.0	89.7413	514.0	95.2355	576.0	92.1921
267.0	0.0000	329.0	0.0000	391.0	20.3222	453.0	90.1315	515.0	94.7169	577.0	92.0912
268.0	0.0000	330.0	0.0000	392.0	24.7253	454.0	90.6513	516.0	93.9806	578.0	91.8569
269.0	0.0000	331.0	0.0000	393.0	29.4988	455.0	91.1850	517.0	93.1102	579.0	91.5011
270.0	0.0000	332.0	0.0000	394.0	34.7732	456.0	91.6032	518.0	92.2006	580.0	91.0478
271.0	0.0000	333.0	0.0000	395.0	40.7604	457.0	91.7982	519.0	91.3419	581.0	90.5307
272.0	0.0000	334.0	0.0000	396.0	47.6519	458.0	91.7164	520.0	90.6070	582.0	89.9902
273.0	0.0000	335.0	0.0000	397.0	55.5620	459.0	91.3739	521.0	90.0445	583.0	89.4693
274.0	0.0000	336.0	0.0000	398.0	64.5381	460.0	90.8508	522.0	89.6757	584.0	89.0104
275.0	0.0000	337.0	0.0000	399.0	74.6262	461.0	90.2656	523.0	89.4954	585.0	88.6519
276.0	0.0000	338.0	0.0000	400.0	85.9435	462.0	89.7422	524.0	89.4760	586.0	88.4257
277.0	0.0000	339.0	0.0000	401.0	86.0931	463.0	89.3790	525.0	89.5726	587.0	88.3555
278.0	0.0000	340.0	0.0000	402.0	86.2275	464.0	89.2298	526.0	89.7310	588.0	88.4555
279.0	0.0000	341.0	0.0000	403.0	86.3591	465.0	89.2962	527.0	89.8959	589.0	88.7295
280.0	0.0000	342.0	0.0000	404.0	86.4888	466.0	89.5318	528.0	90.0191	590.0	89.1710
281.0	0.0000	343.0	0.0000	405.0	86.6146	467.0	89.8555	529.0	90.0665	591.0	89.7625
282.0	0.0000	344.0	0.0000	406.0	86.7359	468.0	90.1725	530.0	90.0223	592.0	90.4764
283.0	0.0000	345.0	0.0000	407.0	86.8551	469.0	90.3978	531.0	89.8902	593.0	91.2760
284.0	0.0000	346.0	0.0001	408.0	86.9744	470.0	90.4783	532.0	89.6898	594.0	92.1167
285.0	0.0000	347.0	0.0002	409.0	87.0936	471.0	90.4049	533.0	89.4520	595.0	92.9488
286.0	0.0000	348.0	0.0005	410.0	87.2104	472.0	90.2132	534.0	89.2115	596.0	93.7211
287.0	0.0000	349.0	0.0015	411.0	87.3225	473.0	89.9700	535.0	89.0008	597.0	94.3845
288.0	0.0000	350.0	0.0041	412.0	87.4302	474.0	89.7542	536.0	88.8450	598.0	94.8967
289.0	0.0000	351.0	0.0048	413.0	87.5370	475.0	89.6357	537.0	88.7583	599.0	95.2260
290.0	0.0000	352.0	0.0057	414.0	87.6476	476.0	89.6590	538.0	88.7434	600.0	95.3546
291.0	0.0000	353.0	0.0070	415.0	87.7641	477.0	89.8334	539.0	88.7924	601.0	95.2707
292.0	0.0000	354.0	0.0089	416.0	87.8840	478.0	90.1318	540.0	88.8893	602.0	95.0075
293.0	0.0000	355.0	0.0115	417.0	88.0004	479.0	90.4955	541.0	89.0138	603.0	94.5878
294.0	0.0000	356.0	0.0150	418.0	88.1050	480.0	90.8472	542.0	89.1452	604.0	94.0431
295.0	0.0000	357.0	0.0196	419.0	88.1930	481.0	91.1076	543.0	89.2666	605.0	93.4103
296.0	0.0000	358.0	0.0253	420.0	88.2648	482.0	91.2143	544.0	89.3674	606.0	92.7280
297.0	0.0000	359.0	0.0318	421.0	88.3261	483.0	91.1378	545.0	89.4448	607.0	92.0335
298.0	0.0000	360.0	0.0388	422.0	88.3839	484.0	90.8901	546.0	89.5035	608.0	91.3600
299.0	0.0000	361.0	0.0463	423.0	88.4427	485.0	90.5228	547.0	89.5542	609.0	90.7350
300.0	0.0000	362.0	0.0543	424.0	88.5030	486.0	90.1166	548.0	89.6100	610.0	90.1791
301.0	0.0000	363.0	0.0636	425.0	88.5626	487.0	89.7648	549.0	89.6839	611.0	89.7055
302.0	0.0000	364.0	0.0747	426.0	88.6208	488.0	89.5566	550.0	89.7851	612.0	89.3205
303.0	0.0000	365.0	0.0884	427.0	88.6827	489.0	89.5622	551.0	89.8663	613.0	89.0237
304.0	0.0000	366.0	0.1052	428.0	88.7600	490.0	89.8226	552.0	89.9641	614.0	88.8089
305.0	0.0000	367.0	0.1257	429.0	88.8668	491.0	90.3432	553.0	90.0715	615.0	88.6657
306.0	0.0000	368.0	0.1515	430.0	89.0118	492.0	91.0921	554.0	90.1784	616.0	88.5802
307.0	0.0000	369.0	0.1855	431.0	89.1903	493.0	92.0014	555.0	90.2725	617.0	88.5369
308.0	0.0000	370.0	0.2328	432.0	89.3794	494.0	92.9745	556.0	90.3421	618.0	88.5202
309.0	0.0000	371.0	0.3013	433.0	89.5417	495.0	93.8976	557.0	90.3771	619.0	88.5156
310.0	0.0000	372.0	0.4014	434.0	89.6367	496.0	94.6579	558.0	90.3719	620.0	88.5114
311.0	0.0000	373.0	0.5452	435.0	89.6367	497.0	95.1635	559.0	90.3258	621.0	88.4999

nm	Ave	nm	Ave	nm	Ave	nm	Ave	nm	Ave	nm	Ave
622.0	88.4780	693.0	89.4112	764.0	94.5770	835.0	91.5693	906.0	88.6307	977.0	90.6479
623.0	88.4475	694.0	89.1187	765.0	95.1854	836.0	91.2178	907.0	88.8586	978.0	90.7107
624.0	88.4153	695.0	88.9084	766.0	95.7458	837.0	90.8847	908.0	89.1126	979.0	90.7736
625.0	88.3926	696.0	88.7756	767.0	96.2454	838.0	90.5738	909.0	89.3908	980.0	90.8353
626.0	88.3941	697.0	88.7142	768.0	96.6727	839.0	90.2887	910.0	89.6911	981.0	90.8945
627.0	88.4368	698.0	88.7165	769.0	97.0177	840.0	90.0322	911.0	90.0112	982.0	90.9500
628.0	88.5388	699.0	88.7744	770.0	97.2723	841.0	89.8068	912.0	90.3484	983.0	91.0006
629.0	88.7175	700.0	88.8792	771.0	97.4308	842.0	89.6144	913.0	90.7002	984.0	91.0454
630.0	88.9890	701.0	89.0219	772.0	97.4898	843.0	89.4564	914.0	91.0635	985.0	91.0835
631.0	89.3662	702.0	89.1942	773.0	97.4485	844.0	89.3338	915.0	91.4353	986.0	91.1139
632.0	89.8579	703.0	89.3882	774.0	97.3086	845.0	89.2471	916.0	91.8124	987.0	91.1360
633.0	90.4681	704.0	89.5969	775.0	97.0745	846.0	89.1963	917.0	92.1914	988.0	91.1493
634.0	91.1947	705.0	89.8143	776.0	96.7526	847.0	89.1811	918.0	92.5690	989.0	91.1534
635.0	92.0291	706.0	90.0357	777.0	96.3513	848.0	89.2005	919.0	92.9419	990.0	91.1479
636.0	92.9557	707.0	90.2574	778.0	95.8808	849.0	89.2535	920.0	93.3065	991.0	91.1329
637.0	93.9515	708.0	90.4773	779.0	95.3524	850.0	89.3382	921.0	93.6596	992.0	91.1082
638.0	94.9865	709.0	90.6941	780.0	94.7782	851.0	89.4523	922.0	93.9980	993.0	91.0740
639.0	96.0240	710.0	90.9077	781.0	94.1706	852.0	89.5935	923.0	94.3185	994.0	91.0307
640.0	97.0226	711.0	91.1188	782.0	93.5424	853.0	89.7592	924.0	94.6182	995.0	90.9786
641.0	97.9375	712.0	91.3287	783.0	92.9059	854.0	89.9465	925.0	94.8943	996.0	90.9182
642.0	98.7237	713.0	91.5389	784.0	92.2729	855.0	90.1523	926.0	95.1445	997.0	90.8502
643.0	99.3391	714.0	91.7510	785.0	91.6544	856.0	90.3731	927.0	95.3665	998.0	90.7754
644.0	99.7480	715.0	91.9663	786.0	91.0606	857.0	90.6053	928.0	95.5586	999.0	90.6945
645.0	99.9243	716.0	92.1855	787.0	90.5007	858.0	90.8451	929.0	95.7192	1000.0	90.6084
646.0	99.8543	717.0	92.4090	788.0	89.9826	859.0	91.0887	930.0	95.8473	1001.0	90.5182
647.0	99.5381	718.0	92.6357	789.0	89.5132	860.0	91.3321	931.0	95.9422	1002.0	90.4247
648.0	98.9899	719.0	92.8641	790.0	89.0984	861.0	91.5713	932.0	96.0035	1003.0	90.3291
649.0	98.2364	720.0	93.0911	791.0	88.7428	862.0	91.8024	933.0	96.0313	1004.0	90.2323
650.0	97.3149	721.0	93.3131	792.0	88.4499	863.0	92.0217	934.0	96.0261	1005.0	90.1356
651.0	96.2710	722.0	93.5250	793.0	88.2222	864.0	92.2253	935.0	95.9888	1006.0	90.0397
652.0	95.1519	723.0	93.7212	794.0	88.0614	865.0	92.4100	936.0	95.9205	1007.0	89.9459
653.0	94.0062	724.0	93.8954	795.0	87.9680	866.0	92.5725	937.0	95.8227	1008.0	89.8551
654.0	92.8804	725.0	94.0409	796.0	87.9416	867.0	92.7101	938.0	95.6972	1009.0	89.7682
655.0	91.8169	726.0	94.1508	797.0	87.9812	868.0	92.8202	939.0	95.5462	1010.0	89.6861
656.0	90.8524	727.0	94.2186	798.0	88.0847	869.0	92.9009	940.0	95.3719	1011.0	89.6097
657.0	90.0174	728.0	94.2385	799.0	88.2493	870.0	92.9506	941.0	95.1767	1012.0	89.5398
658.0	89.3361	729.0	94.2054	800.0	88.4715	871.0	92.9682	942.0	94.9633	1013.0	89.4770
659.0	88.8260	730.0	94.1157	801.0	88.7460	872.0	92.9532	943.0	94.7343	1014.0	89.4219
660.0	88.4985	731.0	93.9673	802.0	89.0684	873.0	92.9056	944.0	94.4926	1015.0	89.3752
661.0	88.3595	732.0	93.7599	803.0	89.4333	874.0	92.8258	945.0	94.2409	1016.0	89.3372
662.0	88.4092	733.0	93.4950	804.0	89.8346	875.0	92.7148	946.0	93.9819	1017.0	89.3083
663.0	88.6423	734.0	93.1761	805.0	90.2659	876.0	92.5741	947.0	93.7183	1018.0	89.2887
664.0	89.0490	735.0	92.8084	806.0	90.7203	877.0	92.4055	948.0	93.4527	1019.0	89.2787
665.0	89.6141	736.0	92.3990	807.0	91.1903	878.0	92.2113	949.0	93.1877	1020.0	89.2782
666.0	90.3178	737.0	91.9563	808.0	91.6685	879.0	91.9943	950.0	92.9256	1021.0	89.2872
667.0	91.1355	738.0	91.4901	809.0	92.1472	880.0	91.7573	951.0	92.6689	1022.0	89.3055
668.0	92.0386	739.0	91.0109	810.0	92.6185	881.0	91.5035	952.0	92.4193	1023.0	89.3330
669.0	92.9943	740.0	90.5297	811.0	93.0748	882.0	91.2364	953.0	92.1786	1024.0	89.3692
670.0	93.9674	741.0	90.0579	812.0	93.5088	883.0	90.9594	954.0	91.9486	1025.0	89.4139
671.0	94.9205	742.0	89.6065	813.0	93.9133	884.0	90.6762	955.0	91.7307	1026.0	89.4664
672.0	95.8166	743.0	89.1865	814.0	94.2818	885.0	90.3904	956.0	91.5262	1027.0	89.5261
673.0	96.6199	744.0	88.8079	815.0	94.6086	886.0	90.1056	957.0	91.3362	1028.0	89.5924
674.0	97.2984	745.0	88.4799	816.0	94.8886	887.0	89.8253	958.0	91.1615	1029.0	89.6645
675.0	97.8257	746.0	88.2109	817.0	95.1177	888.0	89.5530	959.0	91.0029	1030.0	89.7417
676.0	98.1823	747.0	88.0080	818.0	95.2927	889.0	89.2919	960.0	90.8608	1031.0	89.8230
677.0	98.3570	748.0	87.8770	819.0	95.4116	890.0	89.0451	961.0	90.7356	1032.0	89.9075
678.0	98.3476	749.0	87.8226	820.0	95.4734	891.0	88.8157	962.0	90.6274	1033.0	89.9942
679.0	98.1602	750.0	87.8478	821.0	95.4782	892.0	88.6061	963.0	90.5360	1034.0	90.0822
680.0	97.8091	751.0	87.9481	822.0	95.4272	893.0	88.4189	964.0	90.4612	1035.0	90.1704
681.0	97.3147	752.0	88.1262	823.0	95.3226	894.0	88.2563	965.0	90.4027	1036.0	90.2578
682.0	96.7022	753.0	88.3812	824.0	95.1674	895.0	88.1201	966.0	90.3599	1037.0	90.3433
683.0	95.9997	754.0	88.7106	825.0	94.9656	896.0	88.0120	967.0	90.3321	1038.0	90.4260
684.0	95.2362	755.0	89.1104	826.0	94.7218	897.0	87.9334	968.0	90.3185	1039.0	90.5048
685.0	94.4403	756.0	89.5755	827.0	94.4412	898.0	87.8854	969.0	90.3181	1040.0	90.5786
686.0	93.6385	757.0	90.0991	828.0	94.1293	899.0	87.8688	970.0	90.3298	1041.0	90.6467
687.0	92.8548	758.0	90.6733	829.0	93.7920	900.0	87.8840	971.0	90.3526	1042.0	90.7080
688.0	92.1094	759.0	91.2886	830.0	93.4354	901.0	87.9304	972.0	90.3852	1043.0	90.7619
689.0	91.4191	760.0	91.9345	831.0	93.0655	902.0	88.0087	973.0	90.4262	1044.0	90.8074
690.0	90.7967	761.0	92.5992	832.0	92.6883	903.0	88.1186	974.0	90.4744	1045.0	90.8439
691.0	90.2514	762.0	93.2702	833.0	92.3095	904.0	88.2595	975.0	90.5284	1046.0	90.8709
692.0	89.7887	763.0	93.9340	834.0	91.9348	905.0	88.4306	976.0	90.5867	1047.0	90.8878

nm	Ave	nm	Ave	nm	Ave	nm	Ave	nm	Ave	nm	Ave
1048.0	90.8943	1119.0	94.4312	1190.0	94.8589	1261.0	87.8268	1332.0	27.5947	1403.0	6.5513
1049.0	90.8900	1120.0	94.4742	1191.0	95.3089	1262.0	88.1680	1333.0	26.6223	1404.0	6.5146
1050.0	90.8749	1121.0	94.4952	1192.0	95.7520	1263.0	88.5399	1334.0	25.6938	1405.0	6.4803
1051.0	90.8490	1122.0	94.4939	1193.0	96.1860	1264.0	88.9411	1335.0	24.8075	1406.0	6.4483
1052.0	90.8123	1123.0	94.4700	1194.0	96.6081	1265.0	89.3697	1336.0	23.9614	1407.0	6.4187
1053.0	90.7649	1124.0	94.4234	1195.0	97.0160	1266.0	89.8238	1337.0	23.1539	1408.0	6.3913
1054.0	90.7072	1125.0	94.3543	1196.0	97.4072	1267.0	90.3008	1338.0	22.3833	1409.0	6.3661
1055.0	90.6395	1126.0	94.2630	1197.0	97.7791	1268.0	90.7982	1339.0	21.6479	1410.0	6.3432
1056.0	90.5623	1127.0	94.1498	1198.0	98.1294	1269.0	91.3126	1340.0	20.9460	1411.0	6.3223
1057.0	90.4762	1128.0	94.0155	1199.0	98.4557	1270.0	91.8406	1341.0	20.2762	1412.0	6.3036
1058.0	90.3820	1129.0	93.8608	1200.0	98.7558	1271.0	92.3782	1342.0	19.6369	1413.0	6.2870
1059.0	90.2804	1130.0	93.6867	1201.0	99.0275	1272.0	92.9209	1343.0	19.0267	1414.0	6.2724
1060.0	90.1722	1131.0	93.4941	1202.0	99.2690	1273.0	93.4638	1344.0	18.4442	1415.0	6.2599
1061.0	90.0585	1132.0	93.2843	1203.0	99.4783	1274.0	94.0015	1345.0	17.8880	1416.0	6.2493
1062.0	89.9402	1133.0	93.0587	1204.0	99.6539	1275.0	94.5280	1346.0	17.3570	1417.0	6.2408
1063.0	89.8183	1134.0	92.8185	1205.0	99.7945	1276.0	95.0369	1347.0	16.8499	1418.0	6.2341
1064.0	89.6940	1135.0	92.5654	1206.0	99.8988	1277.0	95.5214	1348.0	16.3655	1419.0	6.2294
1065.0	89.5684	1136.0	92.3009	1207.0	99.9659	1278.0	95.9739	1349.0	15.9027	1420.0	6.2267
1066.0	89.4426	1137.0	92.0267	1208.0	99.9951	1279.0	96.3867	1350.0	15.4606	1421.0	6.2258
1067.0	89.3178	1138.0	91.7445	1209.0	99.9860	1280.0	96.7515	1351.0	15.0377	1422.0	6.2268
1068.0	89.1951	1139.0	91.4559	1210.0	99.9386	1281.0	97.0599	1352.0	14.6335	1423.0	6.2296
1069.0	89.0757	1140.0	91.1629	1211.0	99.8528	1282.0	97.3032	1353.0	14.2470	1424.0	6.2344
1070.0	88.9607	1141.0	90.8671	1212.0	99.7292	1283.0	97.4725	1354.0	13.8775	1425.0	6.2409
1071.0	88.8513	1142.0	90.5702	1213.0	99.5685	1284.0	97.5590	1355.0	13.5241	1426.0	6.2493
1072.0	88.7485	1143.0	90.2742	1214.0	99.3715	1285.0	97.5541	1356.0	13.1860	1427.0	6.2596
1073.0	88.6534	1144.0	89.9807	1215.0	99.1395	1286.0	97.4496	1357.0	12.8625	1428.0	6.2717
1074.0	88.5669	1145.0	89.6914	1216.0	98.8740	1287.0	97.2378	1358.0	12.5530	1429.0	6.2856
1075.0	88.4900	1146.0	89.4079	1217.0	98.5766	1288.0	96.9116	1359.0	12.2567	1430.0	6.3013
1076.0	88.4235	1147.0	89.1320	1218.0	98.2492	1289.0	96.4649	1360.0	11.9731	1431.0	6.3188
1077.0	88.3684	1148.0	88.8651	1219.0	97.8938	1290.0	95.8926	1361.0	11.7015	1432.0	6.3381
1078.0	88.3253	1149.0	88.6088	1220.0	97.5127	1291.0	95.1909	1362.0	11.4414	1433.0	6.3593
1079.0	88.2949	1150.0	88.3645	1221.0	97.1082	1292.0	94.3574	1363.0	11.1923	1434.0	6.3823
1080.0	88.2778	1151.0	88.1341	1222.0	96.6829	1293.0	93.3912	1364.0	10.9536	1435.0	6.4071
1081.0	88.2746	1152.0	87.9184	1223.0	96.2393	1294.0	92.2929	1365.0	10.7250	1436.0	6.4338
1082.0	88.2856	1153.0	87.7184	1224.0	95.7800	1295.0	91.0649	1366.0	10.5059	1437.0	6.4622
1083.0	88.3111	1154.0	87.5354	1225.0	95.3077	1296.0	89.7109	1367.0	10.2960	1438.0	6.4925
1084.0	88.3516	1155.0	87.3704	1226.0	94.8252	1297.0	88.2364	1368.0	10.0947	1439.0	6.5247
1085.0	88.4070	1156.0	87.2243	1227.0	94.3352	1298.0	86.6485	1369.0	9.9019	1440.0	6.5587
1086.0	88.4775	1157.0	87.0980	1228.0	93.8404	1299.0	84.9551	1370.0	9.7170	1441.0	6.5946
1087.0	88.5630	1158.0	86.9924	1229.0	93.3434	1300.0	83.1659	1371.0	9.5397	1442.0	6.6323
1088.0	88.6634	1159.0	86.9082	1230.0	92.8469	1301.0	81.2949	1372.0	9.3698	1443.0	6.6719
1089.0	88.7786	1160.0	86.8461	1231.0	92.3536	1302.0	79.3497	1373.0	9.2069	1444.0	6.7135
1090.0	88.9081	1161.0	86.8065	1232.0	91.8658	1303.0	77.3416	1374.0	9.0507	1445.0	6.7569
1091.0	89.0515	1162.0	86.7901	1233.0	91.3860	1304.0	75.2824	1375.0	8.9009	1446.0	6.8022
1092.0	89.2084	1163.0	86.7971	1234.0	90.9165	1305.0	73.1837	1376.0	8.7573	1447.0	6.8495
1093.0	89.3781	1164.0	86.8280	1235.0	90.4597	1306.0	71.0571	1377.0	8.6197	1448.0	6.8986
1094.0	89.5599	1165.0	86.8829	1236.0	90.0175	1307.0	68.9139	1378.0	8.4878	1449.0	6.9498
1095.0	89.7530	1166.0	86.9621	1237.0	89.5921	1308.0	66.7645	1379.0	8.3613	1450.0	7.0029
1096.0	89.9565	1167.0	87.0655	1238.0	89.1854	1309.0	64.6191	1380.0	8.2401	1451.0	7.0578
1097.0	90.1694	1168.0	87.1931	1239.0	88.7992	1310.0	62.4868	1381.0	8.1240	1452.0	7.1148
1098.0	90.3906	1169.0	87.3449	1240.0	88.4352	1311.0	60.3760	1382.0	8.0127	1453.0	7.1737
1099.0	90.6189	1170.0	87.5206	1241.0	88.0949	1312.0	58.2943	1383.0	7.9062	1454.0	7.2346
1100.0	90.8531	1171.0	87.7200	1242.0	87.7800	1313.0	56.2482	1384.0	7.8042	1455.0	7.2976
1101.0	91.0908	1172.0	87.9427	1243.0	87.4918	1314.0	54.2434	1385.0	7.7065	1456.0	7.3625
1102.0	91.3318	1173.0	88.1881	1244.0	87.2316	1315.0	52.2849	1386.0	7.6130	1457.0	7.4296
1103.0	91.5744	1174.0	88.4557	1245.0	87.0005	1316.0	50.3765	1387.0	7.5236	1458.0	7.4986
1104.0	91.8172	1175.0	88.7448	1246.0	86.7997	1317.0	48.5216	1388.0	7.4381	1459.0	7.5697
1105.0	92.0587	1176.0	89.0546	1247.0	86.6301	1318.0	46.7225	1389.0	7.3564	1460.0	7.6429
1106.0	92.2973	1177.0	89.3842	1248.0	86.4926	1319.0	44.9813	1390.0	7.2784	1461.0	7.7182
1107.0	92.5314	1178.0	89.7327	1249.0	86.3879	1320.0	43.2989	1391.0	7.2039	1462.0	7.7955
1108.0	92.7594	1179.0	90.0988	1250.0	86.3168	1321.0	41.6762	1392.0	7.1329	1463.0	7.8749
1109.0	92.9796	1180.0	90.4814	1251.0	86.2798	1322.0	40.1133	1393.0	7.0652	1464.0	7.9564
1110.0	93.1905	1181.0	90.8790	1252.0	86.2773	1323.0	38.6101	1394.0	7.0007	1465.0	8.0400
1111.0	93.3906	1182.0	91.2903	1253.0	86.3096	1324.0	37.1659	1395.0	6.9394	1466.0	8.1256
1112.0	93.5782	1183.0	91.7137	1254.0	86.3771	1325.0	35.7799	1396.0	6.8811	1467.0	8.2133
1113.0	93.7519	1184.0	92.1474	1255.0	86.4799	1326.0	34.4510	1397.0	6.8257	1468.0	8.3031
1114.0	93.9104	1185.0	92.5897	1256.0	86.6179	1327.0	33.1780	1398.0	6.7732	1469.0	8.3949
1115.0	94.0522	1186.0	93.0386	1257.0	86.7910	1328.0	31.9592	1399.0	6.7236	1470.0	8.4888
1116.0	94.1763	1187.0	93.4922	1258.0	86.9990	1329.0	30.7933	1400.0	6.6766	1471.0	8.5847
1117.0	94.2814	1188.0	93.9482	1259.0	87.2414	1330.0	29.6783	1401.0	6.6323	1472.0	8.6826
1118.0	94.3667	1189.0	94.4046	1260.0	87.5176	1331.0	28.6127	1402.0	6.5906	1473.0	8.7825

nm	Ave	nm	Ave	nm	Ave	nm	Ave	nm	Ave	nm	Ave
1474.0	8.8843	1545.0	13.8895	1616.0	10.2653	1687.0	13.1137	1758.0	15.4520	1829.0	12.1923
1475.0	8.9881	1546.0	13.8361	1617.0	10.2596	1688.0	13.1869	1759.0	15.4185	1830.0	12.1613
1476.0	9.0937	1547.0	13.7802	1618.0	10.2555	1689.0	13.2603	1760.0	15.3836	1831.0	12.1310
1477.0	9.2012	1548.0	13.7217	1619.0	10.2528	1690.0	13.3338	1761.0	15.3472	1832.0	12.1016
1478.0	9.3104	1549.0	13.6611	1620.0	10.2516	1691.0	13.4073	1762.0	15.3095	1833.0	12.0729
1479.0	9.4214	1550.0	13.5984	1621.0	10.2519	1692.0	13.4808	1763.0	15.2705	1834.0	12.0451
1480.0	9.5341	1551.0	13.5337	1622.0	10.2537	1693.0	13.5541	1764.0	15.2302	1835.0	12.0181
1481.0	9.6483	1552.0	13.4674	1623.0	10.2570	1694.0	13.6274	1765.0	15.1888	1836.0	11.9919
1482.0	9.7642	1553.0	13.3995	1624.0	10.2617	1695.0	13.7004	1766.0	15.1462	1837.0	11.9665
1483.0	9.8814	1554.0	13.3302	1625.0	10.2679	1696.0	13.7731	1767.0	15.1025	1838.0	11.9419
1484.0	10.0001	1555.0	13.2598	1626.0	10.2755	1697.0	13.8455	1768.0	15.0579	1839.0	11.9182
1485.0	10.1200	1556.0	13.1883	1627.0	10.2846	1698.0	13.9175	1769.0	15.0123	1840.0	11.8953
1486.0	10.2412	1557.0	13.1160	1628.0	10.2952	1699.0	13.9890	1770.0	14.9658	1841.0	11.8731
1487.0	10.3634	1558.0	13.0429	1629.0	10.3071	1700.0	14.0600	1771.0	14.9184	1842.0	11.8519
1488.0	10.4865	1559.0	12.9693	1630.0	10.3205	1701.0	14.1303	1772.0	14.8703	1843.0	11.8314
1489.0	10.6105	1560.0	12.8952	1631.0	10.3354	1702.0	14.1999	1773.0	14.8215	1844.0	11.8117
1490.0	10.7352	1561.0	12.8209	1632.0	10.3516	1703.0	14.2687	1774.0	14.7720	1845.0	11.7929
1491.0	10.8605	1562.0	12.7464	1633.0	10.3693	1704.0	14.3368	1775.0	14.7218	1846.0	11.7749
1492.0	10.9863	1563.0	12.6718	1634.0	10.3883	1705.0	14.4040	1776.0	14.6712	1847.0	11.7577
1493.0	11.1123	1564.0	12.5973	1635.0	10.4088	1706.0	14.4702	1777.0	14.6200	1848.0	11.7413
1494.0	11.2384	1565.0	12.5230	1636.0	10.4307	1707.0	14.5354	1778.0	14.5683	1849.0	11.7257
1495.0	11.3645	1566.0	12.4490	1637.0	10.4539	1708.0	14.5995	1779.0	14.5163	1850.0	11.7110
1496.0	11.4903	1567.0	12.3754	1638.0	10.4785	1709.0	14.6625	1780.0	14.4639	1851.0	11.6970
1497.0	11.6157	1568.0	12.3023	1639.0	10.5045	1710.0	14.7242	1781.0	14.4113	1852.0	11.6839
1498.0	11.7406	1569.0	12.2298	1640.0	10.5319	1711.0	14.7847	1782.0	14.3583	1853.0	11.6716
1499.0	11.8647	1570.0	12.1580	1641.0	10.5606	1712.0	14.8439	1783.0	14.3052	1854.0	11.6601
1500.0	11.9878	1571.0	12.0869	1642.0	10.5907	1713.0	14.9016	1784.0	14.2519	1855.0	11.6494
1501.0	12.1095	1572.0	12.0166	1643.0	10.6221	1714.0	14.9578	1785.0	14.1986	1856.0	11.6395
1502.0	12.2298	1573.0	11.9473	1644.0	10.6549	1715.0	15.0125	1786.0	14.1451	1857.0	11.6304
1503.0	12.3485	1574.0	11.8788	1645.0	10.6890	1716.0	15.0656	1787.0	14.0916	1858.0	11.6222
1504.0	12.4654	1575.0	11.8114	1646.0	10.7244	1717.0	15.1171	1788.0	14.0382	1859.0	11.6147
1505.0	12.5803	1576.0	11.7451	1647.0	10.7611	1718.0	15.1669	1789.0	13.9848	1860.0	11.6080
1506.0	12.6929	1577.0	11.6799	1648.0	10.7991	1719.0	15.2149	1790.0	13.9315	1861.0	11.6021
1507.0	12.8031	1578.0	11.6159	1649.0	10.8384	1720.0	15.2610	1791.0	13.8783	1862.0	11.5970
1508.0	12.9106	1579.0	11.5531	1650.0	10.8790	1721.0	15.3053	1792.0	13.8253	1863.0	11.5927
1509.0	13.0153	1580.0	11.4916	1651.0	10.9208	1722.0	15.3477	1793.0	13.7725	1864.0	11.5892
1510.0	13.1168	1581.0	11.4314	1652.0	10.9639	1723.0	15.3882	1794.0	13.7200	1865.0	11.5865
1511.0	13.2151	1582.0	11.3725	1653.0	11.0081	1724.0	15.4266	1795.0	13.6677	1866.0	11.5845
1512.0	13.3099	1583.0	11.3150	1654.0	11.0537	1725.0	15.4630	1796.0	13.6157	1867.0	11.5834
1513.0	13.4010	1584.0	11.2588	1655.0	11.1004	1726.0	15.4973	1797.0	13.5641	1868.0	11.5830
1514.0	13.4883	1585.0	11.2041	1656.0	11.1483	1727.0	15.5295	1798.0	13.5128	1869.0	11.5834
1515.0	13.5715	1586.0	11.1508	1657.0	11.1975	1728.0	15.5596	1799.0	13.4620	1870.0	11.5846
1516.0	13.6506	1587.0	11.0990	1658.0	11.2478	1729.0	15.5875	1800.0	13.4115	1871.0	11.5866
1517.0	13.7253	1588.0	11.0486	1659.0	11.2993	1730.0	15.6132	1801.0	13.3608	1872.0	11.5893
1518.0	13.7955	1589.0	10.9998	1660.0	11.3519	1731.0	15.6367	1802.0	13.3106	1873.0	11.5928
1519.0	13.8612	1590.0	10.9524	1661.0	11.4056	1732.0	15.6580	1803.0	13.2608	1874.0	11.5971
1520.0	13.9221	1591.0	10.9066	1662.0	11.4604	1733.0	15.6770	1804.0	13.2115	1875.0	11.6021
1521.0	13.9782	1592.0	10.8623	1663.0	11.5164	1734.0	15.6938	1805.0	13.1628	1876.0	11.6079
1522.0	14.0294	1593.0	10.8196	1664.0	11.5734	1735.0	15.7083	1806.0	13.1147	1877.0	11.6144
1523.0	14.0756	1594.0	10.7784	1665.0	11.6314	1736.0	15.7205	1807.0	13.0671	1878.0	11.6217
1524.0	14.1168	1595.0	10.7387	1666.0	11.6905	1737.0	15.7305	1808.0	13.0201	1879.0	11.6298
1525.0	14.1529	1596.0	10.7006	1667.0	11.7505	1738.0	15.7382	1809.0	12.9737	1880.0	11.6386
1526.0	14.1840	1597.0	10.6641	1668.0	11.8116	1739.0	15.7437	1810.0	12.9279	1881.0	11.6482
1527.0	14.2100	1598.0	10.6291	1669.0	11.8735	1740.0	15.7469	1811.0	12.8828	1882.0	11.6585
1528.0	14.2309	1599.0	10.5957	1670.0	11.9364	1741.0	15.7479	1812.0	12.8383	1883.0	11.6695
1529.0	14.2468	1600.0	10.5639	1671.0	12.0002	1742.0	15.7467	1813.0	12.7944	1884.0	11.6813
1530.0	14.2576	1601.0	10.5336	1672.0	12.0649	1743.0	15.7433	1814.0	12.7513	1885.0	11.6938
1531.0	14.2636	1602.0	10.5049	1673.0	12.1304	1744.0	15.7377	1815.0	12.7089	1886.0	11.7071
1532.0	14.2646	1603.0	10.4777	1674.0	12.1967	1745.0	15.7299	1816.0	12.6671	1887.0	11.7211
1533.0	14.2609	1604.0	10.4521	1675.0	12.2637	1746.0	15.7201	1817.0	12.6261	1888.0	11.7358
1534.0	14.2525	1605.0	10.4280	1676.0	12.3315	1747.0	15.7081	1818.0	12.5858	1889.0	11.7512
1535.0	14.2395	1606.0	10.4055	1677.0	12.4000	1748.0	15.6941	1819.0	12.5462	1890.0	11.7674
1536.0	14.2220	1607.0	10.3846	1678.0	12.4691	1749.0	15.6781	1820.0	12.5073	1891.0	11.7843
1537.0	14.2003	1608.0	10.3652	1679.0	12.5388	1750.0	15.6602	1821.0	12.4693	1892.0	11.8019
1538.0	14.1744	1609.0	10.3473	1680.0	12.6091	1751.0	15.6404	1822.0	12.4319	1893.0	11.8202
1539.0	14.1444	1610.0	10.3310	1681.0	12.6800	1752.0	15.6187	1823.0	12.3954	1894.0	11.8392
1540.0	14.1106	1611.0	10.3162	1682.0	12.7513	1753.0	15.5952	1824.0	12.3596	1895.0	11.8589
1541.0	14.0731	1612.0	10.3030	1683.0	12.8231	1754.0	15.5700	1825.0	12.3245	1896.0	11.8794
1542.0	14.0320	1613.0	10.2913	1684.0	12.8953	1755.0	15.5429	1826.0	12.2903	1897.0	11.9005
1543.0	13.9876	1614.0	10.2811	1685.0	12.9678	1756.0	15.5142	1827.0	12.2569	1898.0	11.9223
1544.0	13.9401	1615.0	10.2724	1686.0	13.0406	1757.0	15.4839	1828.0	12.2242	1899.0	11.9449

nm	Ave	nm	Ave	nm	Ave	nm	Ave	nm	Ave	nm	Ave
1900.0	11.9681	1971.0	15.0323	2042.0	18.1264	2113.0	18.0742	2184.0	17.3312	2255.0	17.6838
1901.0	11.9920	1972.0	15.0877	2043.0	18.1470	2114.0	18.0606	2185.0	17.3279	2256.0	17.6960
1902.0	12.0166	1973.0	15.1432	2044.0	18.1668	2115.0	18.0469	2186.0	17.3248	2257.0	17.7084
1903.0	12.0419	1974.0	15.1986	2045.0	18.1859	2116.0	18.0331	2187.0	17.3220	2258.0	17.7209
1904.0	12.0678	1975.0	15.2541	2046.0	18.2042	2117.0	18.0193	2188.0	17.3194	2259.0	17.7336
1905.0	12.0944	1976.0	15.3095	2047.0	18.2217	2118.0	18.0054	2189.0	17.3171	2260.0	17.7465
1906.0	12.1217	1977.0	15.3649	2048.0	18.2384	2119.0	17.9915	2190.0	17.3151	2261.0	17.7595
1907.0	12.1497	1978.0	15.4202	2049.0	18.2543	2120.0	17.9775	2191.0	17.3133	2262.0	17.7726
1908.0	12.1783	1979.0	15.4755	2050.0	18.2694	2121.0	17.9636	2192.0	17.3117	2263.0	17.7859
1909.0	12.2076	1980.0	15.5307	2051.0	18.2840	2122.0	17.9496	2193.0	17.3104	2264.0	17.7993
1910.0	12.2375	1981.0	15.5858	2052.0	18.2978	2123.0	17.9357	2194.0	17.3094	2265.0	17.8128
1911.0	12.2681	1982.0	15.6408	2053.0	18.3108	2124.0	17.9217	2195.0	17.3086	2266.0	17.8265
1912.0	12.2993	1983.0	15.6957	2054.0	18.3230	2125.0	17.9078	2196.0	17.3081	2267.0	17.8403
1913.0	12.3311	1984.0	15.7504	2055.0	18.3346	2126.0	17.8939	2197.0	17.3078	2268.0	17.8542
1914.0	12.3636	1985.0	15.8049	2056.0	18.3454	2127.0	17.8800	2198.0	17.3078	2269.0	17.8683
1915.0	12.3967	1986.0	15.8592	2057.0	18.3554	2128.0	17.8661	2199.0	17.3080	2270.0	17.8824
1916.0	12.4305	1987.0	15.9134	2058.0	18.3647	2129.0	17.8524	2200.0	17.3085	2271.0	17.8968
1917.0	12.4648	1988.0	15.9673	2059.0	18.3734	2130.0	17.8386	2201.0	17.3092	2272.0	17.9112
1918.0	12.4998	1989.0	16.0210	2060.0	18.3813	2131.0	17.8250	2202.0	17.3101	2273.0	17.9257
1919.0	12.5354	1990.0	16.0744	2061.0	18.3885	2132.0	17.8114	2203.0	17.3114	2274.0	17.9404
1920.0	12.5716	1991.0	16.1275	2062.0	18.3950	2133.0	17.7978	2204.0	17.3128	2275.0	17.9551
1921.0	12.6084	1992.0	16.1804	2063.0	18.4008	2134.0	17.7844	2205.0	17.3146	2276.0	17.9700
1922.0	12.6457	1993.0	16.2330	2064.0	18.4060	2135.0	17.7711	2206.0	17.3165	2277.0	17.9850
1923.0	12.6837	1994.0	16.2852	2065.0	18.4105	2136.0	17.7578	2207.0	17.3187	2278.0	18.0001
1924.0	12.7222	1995.0	16.3371	2066.0	18.4144	2137.0	17.7447	2208.0	17.3212	2279.0	18.0153
1925.0	12.7614	1996.0	16.3886	2067.0	18.4176	2138.0	17.7317	2209.0	17.3239	2280.0	18.0306
1926.0	12.8010	1997.0	16.4398	2068.0	18.4202	2139.0	17.7188	2210.0	17.3268	2281.0	18.0460
1927.0	12.8413	1998.0	16.4905	2069.0	18.4221	2140.0	17.7060	2211.0	17.3300	2282.0	18.0615
1928.0	12.8821	1999.0	16.5409	2070.0	18.4235	2141.0	17.6934	2212.0	17.3334	2283.0	18.0771
1929.0	12.9234	2000.0	16.5908	2071.0	18.4243	2142.0	17.6808	2213.0	17.3370	2284.0	18.0928
1930.0	12.9653	2001.0	16.6402	2072.0	18.4244	2143.0	17.6685	2214.0	17.3409	2285.0	18.1085
1931.0	13.0077	2002.0	16.6890	2073.0	18.4240	2144.0	17.6563	2215.0	17.3451	2286.0	18.1244
1932.0	13.0507	2003.0	16.7375	2074.0	18.4231	2145.0	17.6442	2216.0	17.3494	2287.0	18.1403
1933.0	13.0942	2004.0	16.7854	2075.0	18.4215	2146.0	17.6323	2217.0	17.3540	2288.0	18.1564
1934.0	13.1381	2005.0	16.8328	2076.0	18.4195	2147.0	17.6205	2218.0	17.3588	2289.0	18.1725
1935.0	13.1826	2006.0	16.8797	2077.0	18.4169	2148.0	17.6089	2219.0	17.3639	2290.0	18.1887
1936.0	13.2276	2007.0	16.9261	2078.0	18.4138	2149.0	17.5975	2220.0	17.3692	2291.0	18.2049
1937.0	13.2730	2008.0	16.9719	2079.0	18.4101	2150.0	17.5863	2221.0	17.3747	2292.0	18.2213
1938.0	13.3190	2009.0	17.0172	2080.0	18.4060	2151.0	17.5752	2222.0	17.3804	2293.0	18.2377
1939.0	13.3654	2010.0	17.0619	2081.0	18.4014	2152.0	17.5643	2223.0	17.3864	2294.0	18.2542
1940.0	13.4122	2011.0	17.1060	2082.0	18.3964	2153.0	17.5536	2224.0	17.3926	2295.0	18.2708
1941.0	13.4595	2012.0	17.1495	2083.0	18.3909	2154.0	17.5431	2225.0	17.3990	2296.0	18.2874
1942.0	13.5073	2013.0	17.1924	2084.0	18.3849	2155.0	17.5328	2226.0	17.4056	2297.0	18.3041
1943.0	13.5554	2014.0	17.2347	2085.0	18.3785	2156.0	17.5227	2227.0	17.4124	2298.0	18.3209
1944.0	13.6040	2015.0	17.2763	2086.0	18.3717	2157.0	17.5128	2228.0	17.4195	2299.0	18.3377
1945.0	13.6531	2016.0	17.3173	2087.0	18.3645	2158.0	17.5031	2229.0	17.4267	2300.0	18.3546
1946.0	13.7025	2017.0	17.3576	2088.0	18.3569	2159.0	17.4936	2230.0	17.4342	2301.0	18.3714
1947.0	13.7523	2018.0	17.3972	2089.0	18.3490	2160.0	17.4843	2231.0	17.4419	2302.0	18.3883
1948.0	13.8024	2019.0	17.4362	2090.0	18.3406	2161.0	17.4753	2232.0	17.4498	2303.0	18.4053
1949.0	13.8530	2020.0	17.4744	2091.0	18.3319	2162.0	17.4664	2233.0	17.4579	2304.0	18.4222
1950.0	13.9039	2021.0	17.5120	2092.0	18.3229	2163.0	17.4578	2234.0	17.4662	2305.0	18.4393
1951.0	13.9551	2022.0	17.5488	2093.0	18.3135	2164.0	17.4494	2235.0	17.4747	2306.0	18.4564
1952.0	14.0067	2023.0	17.5849	2094.0	18.3038	2165.0	17.4412	2236.0	17.4834	2307.0	18.4735
1953.0	14.0586	2024.0	17.6203	2095.0	18.2938	2166.0	17.4333	2237.0	17.4923	2308.0	18.4907
1954.0	14.1108	2025.0	17.6550	2096.0	18.2836	2167.0	17.4256	2238.0	17.5014	2309.0	18.5079
1955.0	14.1633	2026.0	17.6889	2097.0	18.2730	2168.0	17.4181	2239.0	17.5106	2310.0	18.5252
1956.0	14.2161	2027.0	17.7221	2098.0	18.2622	2169.0	17.4108	2240.0	17.5201	2311.0	18.5425
1957.0	14.2691	2028.0	17.7545	2099.0	18.2511	2170.0	17.4038	2241.0	17.5298	2312.0	18.5599
1958.0	14.3224	2029.0	17.7861	2100.0	18.2398	2171.0	17.3970	2242.0	17.5396	2313.0	18.5773
1959.0	14.3760	2030.0	17.8170	2101.0	18.2281	2172.0	17.3905	2243.0	17.5497	2314.0	18.5947
1960.0	14.4297	2031.0	17.8471	2102.0	18.2162	2173.0	17.3842	2244.0	17.5599	2315.0	18.6122
1961.0	14.4837	2032.0	17.8764	2103.0	18.2041	2174.0	17.3781	2245.0	17.5703	2316.0	18.6297
1962.0	14.5379	2033.0	17.9050	2104.0	18.1918	2175.0	17.3723	2246.0	17.5809	2317.0	18.6473
1963.0	14.5923	2034.0	17.9328	2105.0	18.1793	2176.0	17.3668	2247.0	17.5916	2318.0	18.6648
1964.0	14.6469	2035.0	17.9597	2106.0	18.1667	2177.0	17.3614	2248.0	17.6026	2319.0	18.6824
1965.0	14.7016	2036.0	17.9859	2107.0	18.1539	2178.0	17.3564	2249.0	17.6137	2320.0	18.7001
1966.0	14.7564	2037.0	18.0113	2108.0	18.1409	2179.0	17.3515	2250.0	17.6249	2321.0	18.7178
1967.0	14.8114	2038.0	18.0359	2109.0	18.1278	2180.0	17.3470	2251.0	17.6364	2322.0	18.7355
1968.0	14.8665	2039.0	18.0597	2110.0	18.1146	2181.0	17.3426	2252.0	17.6480	2323.0	18.7532
1969.0	14.9217	2040.0	18.0827	2111.0	18.1012	2182.0	17.3386	2253.0	17.6597	2324.0	18.7710
1970.0	14.9770	2041.0	18.1049	2112.0	18.0878	2183.0	17.3348	2254.0	17.6717	2325.0	18.7887

TFCalc

nm	Ave	nm	Ave	nm	Ave
2326.0	18.8065	2397.0	20.1311	2468.0	21.9027
2327.0	18.8244	2398.0	20.1512	2469.0	21.9351
2328.0	18.8422	2399.0	20.1714	2470.0	21.9678
2329.0	18.8601	2400.0	20.1917	2471.0	22.0009
2330.0	18.8780	2401.0	20.2121	2472.0	22.0342
2331.0	18.8959	2402.0	20.2326	2473.0	22.0678
2332.0	18.9139	2403.0	20.2531	2474.0	22.1018
2333.0	18.9319	2404.0	20.2738	2475.0	22.1360
2334.0	18.9498	2405.0	20.2945	2476.0	22.1705
2335.0	18.9678	2406.0	20.3153	2477.0	22.2054
2336.0	18.9859	2407.0	20.3362	2478.0	22.2406
2337.0	19.0039	2408.0	20.3572	2479.0	22.2761
2338.0	19.0220	2409.0	20.3783	2480.0	22.3119
2339.0	19.0401	2410.0	20.3996	2481.0	22.3481
2340.0	19.0581	2411.0	20.4209	2482.0	22.3845
2341.0	19.0763	2412.0	20.4423	2483.0	22.4214
2342.0	19.0944	2413.0	20.4639	2484.0	22.4585
2343.0	19.1125	2414.0	20.4855	2485.0	22.4960
2344.0	19.1307	2415.0	20.5073	2486.0	22.5339
2345.0	19.1489	2416.0	20.5292	2487.0	22.5721
2346.0	19.1671	2417.0	20.5512	2488.0	22.6107
2347.0	19.1853	2418.0	20.5733	2489.0	22.6496
2348.0	19.2035	2419.0	20.5956	2490.0	22.6889
2349.0	19.2218	2420.0	20.6180	2491.0	22.7285
2350.0	19.2400	2421.0	20.6405	2492.0	22.7685
2351.0	19.2583	2422.0	20.6631	2493.0	22.8089
2352.0	19.2766	2423.0	20.6859	2494.0	22.8497
2353.0	19.2949	2424.0	20.7088	2495.0	22.8908
2354.0	19.3133	2425.0	20.7319	2496.0	22.9324
2355.0	19.3316	2426.0	20.7551	2497.0	22.9743
2356.0	19.3500	2427.0	20.7785	2498.0	23.0166
2357.0	19.3684	2428.0	20.8020	2499.0	23.0593
2358.0	19.3868	2429.0	20.8257	2500.0	23.1025
2359.0	19.4053	2430.0	20.8495		
2360.0	19.4237	2431.0	20.8735		
2361.0	19.4422	2432.0	20.8977		
2362.0	19.4607	2433.0	20.9220		
2363.0	19.4792	2434.0	20.9465		
2364.0	19.4978	2435.0	20.9712		
2365.0	19.5163	2436.0	20.9960		
2366.0	19.5349	2437.0	21.0210		
2367.0	19.5536	2438.0	21.0462		
2368.0	19.5722	2439.0	21.0716		
2369.0	19.5909	2440.0	21.0972		
2370.0	19.6096	2441.0	21.1229		
2371.0	19.6284	2442.0	21.1489		
2372.0	19.6471	2443.0	21.1750		
2373.0	19.6659	2444.0	21.2014		
2374.0	19.6848	2445.0	21.2280		
2375.0	19.7037	2446.0	21.2547		
2376.0	19.7226	2447.0	21.2817		
2377.0	19.7415	2448.0	21.3089		
2378.0	19.7605	2449.0	21.3363		
2379.0	19.7796	2450.0	21.3639		
2380.0	19.7986	2451.0	21.3918		
2381.0	19.8178	2452.0	21.4198		
2382.0	19.8369	2453.0	21.4482		
2383.0	19.8561	2454.0	21.4767		
2384.0	19.8754	2455.0	21.5055		
2385.0	19.8947	2456.0	21.5345		
2386.0	19.9141	2457.0	21.5637		
2387.0	19.9335	2458.0	21.5933		
2388.0	19.9530	2459.0	21.6230		
2389.0	19.9725	2460.0	21.6530		
2390.0	19.9921	2461.0	21.6833		
2391.0	20.0118	2462.0	21.7138		
2392.0	20.0315	2463.0	21.7446		
2393.0	20.0513	2464.0	21.7757		
2394.0	20.0711	2465.0	21.8070		
2395.0	20.0910	2466.0	21.8386		
2396.0	20.1110	2467.0	21.8705		

Appendix D

Nomenclature and Abbreviations

λ_g	Wavelength corresponding to the bandgap energy E_g
E_g	bandgap energy
h	Planck's constant
c	the speed of light
η	conversion efficiency
P_m	generated maximum power by solar cell
P_{in}	The incident power
J_{sc}	Short circuit current
V_{oc}	Open circuit voltage
FF	Fill factor
$\phi(\lambda)$	The photon flux density
p_{abs}	The fraction of the incident power that is absorbed by a solar cell and used for energy conversion
p_{use}	The fraction of the absorbed energy that the solar can deliver as useful energy
A_{proj}	the projected area of the flat panel PV
C_g	The geometric concentration
A	The area of the input to the system and of the
A'	The area of the PV device
θ	acceptance angle
n	The index of refraction at the entrance aperture of the system and
n'	The index of the medium immediately before the PV device
R_s	series resistance
I_D	The Irradiance density
dP	The light power (energy per unit time),
$d\lambda$	unit wavelength
I	Electrical current
n_E	Number of electrons
q	The charge of the electron

EQE	External quantum efficiency
E	The energy of each photon at a wavelength λ
n_P	The number of photons per unit time.
$I_{\lambda,\lambda+\Delta\lambda}$	Photocurrent
$I_{sc,3J}$	Multi junction solar cell short current
$I_{sc,Top}$	Top sub-cell short current
$I_{sc,Middle}$	Middle sub-cell short current
$I_{sc,Bottom}$	bottom sub-cell short current
$I_{D_{AM1.5D}}(\lambda)$	is the solar irradiance density as a function of wavelength
$EQE_{TOP}(\lambda)$	The external quantum efficiency of top sub-cells
$EQE_{Middle}(\lambda)$	The external quantum efficiency of middle sub-cells
$EQE_{Bottom}(\lambda)$	The external quantum efficiency of bottom sub-cells
$T(\lambda)$	The spectral transmission of the concentrator.
HCPV	High concentrator photovoltaic
LCPV	Low concentrator photovoltaic
TIR	Total internal reflection
NIO	Non-imaging optics
δ	The thickness of the thin film layer
z	The location of the layer insertion
P	Function that identify the most appropriate position to insert new layers
T_{cell}	Solar cell temperature
T_{module}	Module temperature at back surface
$R_{th\_cell\_heatsink}$	Thermal resistance between the cell and the back chassis or heat sink core.
P_{cell}	The heat power
η_{op}	The optical efficiency
η	The electrical efficiency
PAR	Peak to average irradiance ratio
POE	Primary optical element
SOE	Secondary optical element
L	The length of the Fresnel lens
W	The width of the Fresnel lens
L_{EnS}	The width of the entry aperture of the secondary optical element

W_{EnS}	The width of the entry aperture of the secondary optical element
L_{ExS}	The width of the exit aperture of the secondary optical element
W_{ExS}	The width of the exit aperture of the secondary optical element
H_S	The height of the secondary optical element
L_{PV}	Solar cell length
W_{PV}	Solar cell Width
H	Solar cell thickness
P_{UV}	The heat power for ultraviolet spectrum
P_{IR}	The heat power for Ifrared spectrum
$S_{AM\ 1.5D}(\lambda)$	Artificial spectrum for the photocurrent when using AM 1.5D
$E_{AM\ 1.5D}(\lambda)$	The standard solar spectrum distribution AM 1.5D
E_A	The activation energy
R_{sh1}	Top sub-cell shunt resistance
R_{sh2}	Middle sub-cell shunt resistance
R_{sh3}	Bottom sub-cell shunt resistance
R_{tl1}	Tunnel junction resistance
R_{tl2}	Tunnel junction resistance
R_{el}	Circuit series resistance
$F(t)$	The unreliability as a function of time
$L(T)$	Temporal measurable characteristic of the device under the life test
C	Parameter of the Arrhenius model
A_F	The acceleration factor
$f(t)$	The Arrhenius–Weibull model for the lifetime distribution and the life stress model.
$f(t, T)$	The probability density function
$g(t)$	The average Arrhenius–Weibull model for the lifetime distribution and the life stress model.
m	is the number of calculated cell temperatures throughout one year
$G(t)$	The new unreliability function by an equation that uses the average Arrhenius–Weibull model
NEDO	New Energy and Industrial Technology Development Organization
I_{p1}	Top sub-cell photocurrent

I_{p2}	Middle sub-cell photocurrent
I_{p3}	Bottom sub-cell photocurrent
P_m	Solar cell maximum power point
FF	Solar cell Fill factor
Pt100	Precision platinum temperature sensor
$S_{RS}(\lambda)$	The artificial spectrum for the photocurrent when using real solar spectrum
$E_{RS}(\lambda)$	Real measured direct spectrum of the sun at the calculation time on February 15, 2017
(Pt100)	precision platinum temperature sensor
V_{mp}	Maximum power voltage
I_{mp}	Maximum power current
$\mathrm{CM}_{Mid}^{Top}(E_{RS})$	The current matching ratio for the multijunction solar cell without concentration
$I_{\mathrm{p,top}}(E_{RS})$	The top sub-cell photocurrent calculated for the real spectrum
$I_{\mathrm{p,mid}}(E_{RS})$	The middle sub-cell photocurrent calculated for the real spectrum
$\mathrm{CM}_{Mid}^{Top}(E_{RS}.Con)$	The current matching ratio for the multijunction solar cell with concentration
$I_{\mathrm{p,top}}(E_{RS}.Con)$	The top sub-cell photocurrent calculated for the real spectrum after concentration
$I_{\mathrm{p,mid}}(E_{RS}.Con)$	The middle sub-cell photocurrent calculated for the real spectrum after concentration
OM_{Mid}^{Top}	The optical matching ratio
e	Sensitivity analysis elasticity

List of publications

I. Academic journals

1. A 3.2% output increase in an existing photovoltaic system using an antireflection and anti-soiling silica-based coat.
   Yasuyuki Ota, Nawwar Ahmad, Kensuke Nishioka
   Solar Energy, Vol. 136, pp. 547-552 (2016).
2. Temperature reduction of solar cells in a concentrator photovoltaic system using a long wavelength cut filter
   Nawwar Ahmad, Yasuyuki Ota, Kensuke Nishioka
   Japanese Journal of Applied Physics, Vol. 56, 032301-1 - 032301-8 (2017).
3. 111 suns concentrator photovoltaic module with wide acceptance angle that can efficiently operate using 30-minute intermittent tracking system.
   Nawwar Ahmad, Yasuyuki Ota, Kenji Araki, Kan-Hua Lee, Masafumi Yamaguchi, Kensuke Nishioka
   Japanese Journal of Applied Physics, Vol. 56, 092301-1 - 092301-8 (2017).

II. International conference proceedings

1. Designing of long wavelength cut thin film filter for temperature reduction of concentrator photovoltaic
   Nawwar Ahmad, Keisuke Hatakeyama, Yasuyuki Ota, Kensuke Nishioka
   MATEC Web of Conferences, Vol. 65, 04002 (2016).
2. Optical and Thermal Simulation for Wide Acceptance Angle CPV Module
   Nawwar Ahmad, Yasuyuki Ota, Kenji Araki, Kan-Hua Lee, Masafumi Yamaguchi, Kensuke Nishioka

AIP Conference Proceedings, Accepted (2017).
3. Repair of damaged lens surface of CPV using silica based coating
Shota Kurogi, Takuya Hirohata, Ahmad Nawwar, Yasuyuki Ota, Kensuke Nishioka
Photovoltaic Specialist Conference (PVSC), 2015 IEEE 42nd, DOI: 10.1109/PVSC.2015.7355762